

# Laboratory of Computational Physics

BY LUCA CASSIA

Dipartimento di Fisica, Università di Milano-Bicocca  
I-20126 Milano, Italy

Email: [1.cassia@campus.unimib.it](mailto:1.cassia@campus.unimib.it)

## Table of contents

<b>1 Hard-Core Molecular Dynamics in 2d</b>	1
1.1 Thermalization	1
1.2 Momentum Distribution	4
1.3 Phase Transition	6
1.4 Collision Times	8
1.5 Mean Squared Displacement	9

## 1 Hard-Core Molecular Dynamics in 2d

In this section we simulate the dynamics of a system of  $N$  identical spherical particles in two dimensions, subject to the hard-core central potential:

$$V(r) = \begin{cases} 0 & r > R \\ \infty & r \leq R \end{cases} \quad (1)$$

with  $\sigma = 2R$  being the diameter of the particles. For convenience we decide to work with adimensional quantities and rescale all lengths by the size  $L$  of the box. In these units the volume of the box itself is rescaled to 1. For the same reason we take the mass of the particles to be the reference unit of mass. Periodic boundary conditions in both directions are implemented in order to reduce boundary effects due to the finite size of the system. This turns our box in a toroidal surface.

### 1.1 Thermalization

First we initialize the system positioning the particles (disks) on the sites of a regular square lattice as in (Fig.1). This type of circle packing has a *packing density*  $\eta$  (i.e., the proportion of the surface covered by the circles) of:

$$\eta = \frac{N\pi\sigma^2}{4L^2} \quad (2)$$

which takes its maximum value for  $\sigma = L/\sqrt{N}$ :

$$\eta_{\max} = \frac{\pi}{4} \approx 0.78539816339... \quad (3)$$

The highest-density lattice arrangement of circles in the plane is actually the hexagonal packing

arrangement, with a maximal packing density of  $\eta_h = \frac{\pi}{2\sqrt{3}} \approx 0.9069$ . In fact we see that, a system with large  $\eta$ , spontaneously tends to arrange itself in such a way (Fig.1).

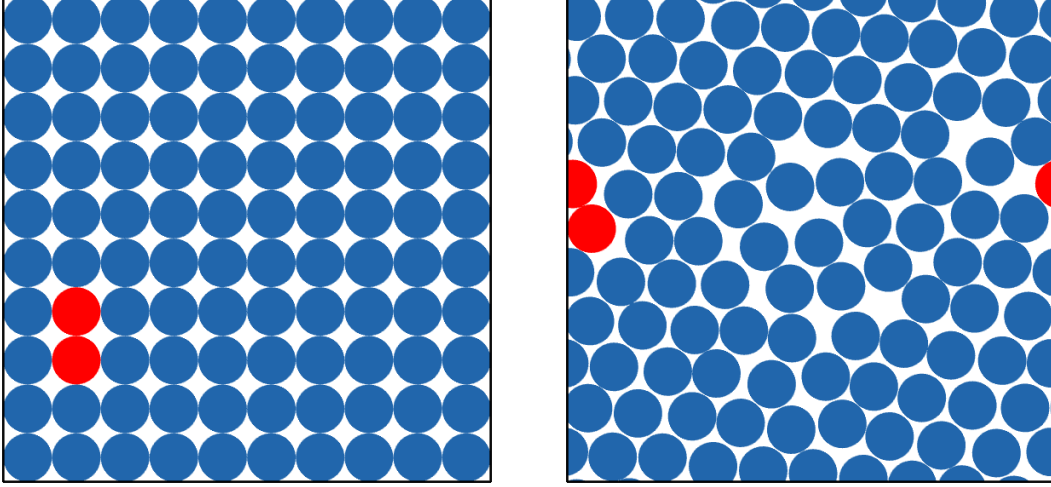


**Figure 1.** On the left we illustrate the initial spatial configuration of a system of 100 particles at temperature  $k_b T = 1$  and  $\eta = 0.78$ . On the right we show the same system after  $10^5$  collisions. The red disks indicate two particles colliding.

The momenta of the particles are initialized with uniform distribution inside the range  $[-1, 1]$  with total momentum equal to zero (center of mass reference frame). After the initialization the momenta are rescaled in order to obtain the desired temperature. Kinetic energy and temperature are related by:

$$K = \frac{d}{2} N k_b T, \quad K = \frac{1}{2} m \sum_{i=1}^N |\vec{v}_i|^2 \quad (4)$$

$$\Rightarrow \quad k_b T = \frac{m}{d N} \sum_{i=1}^N |\vec{v}_i|^2 \quad (5)$$

We now study the mixing properties of this type of system. We evolve a system of  $N = 100$  particles from its initial configuration, for  $10^4$  collisions and measure the pressure (Fig.2) and the mean free path (Fig.3) every 10 collisions. This procedure is also repeated for  $N = 400$ .

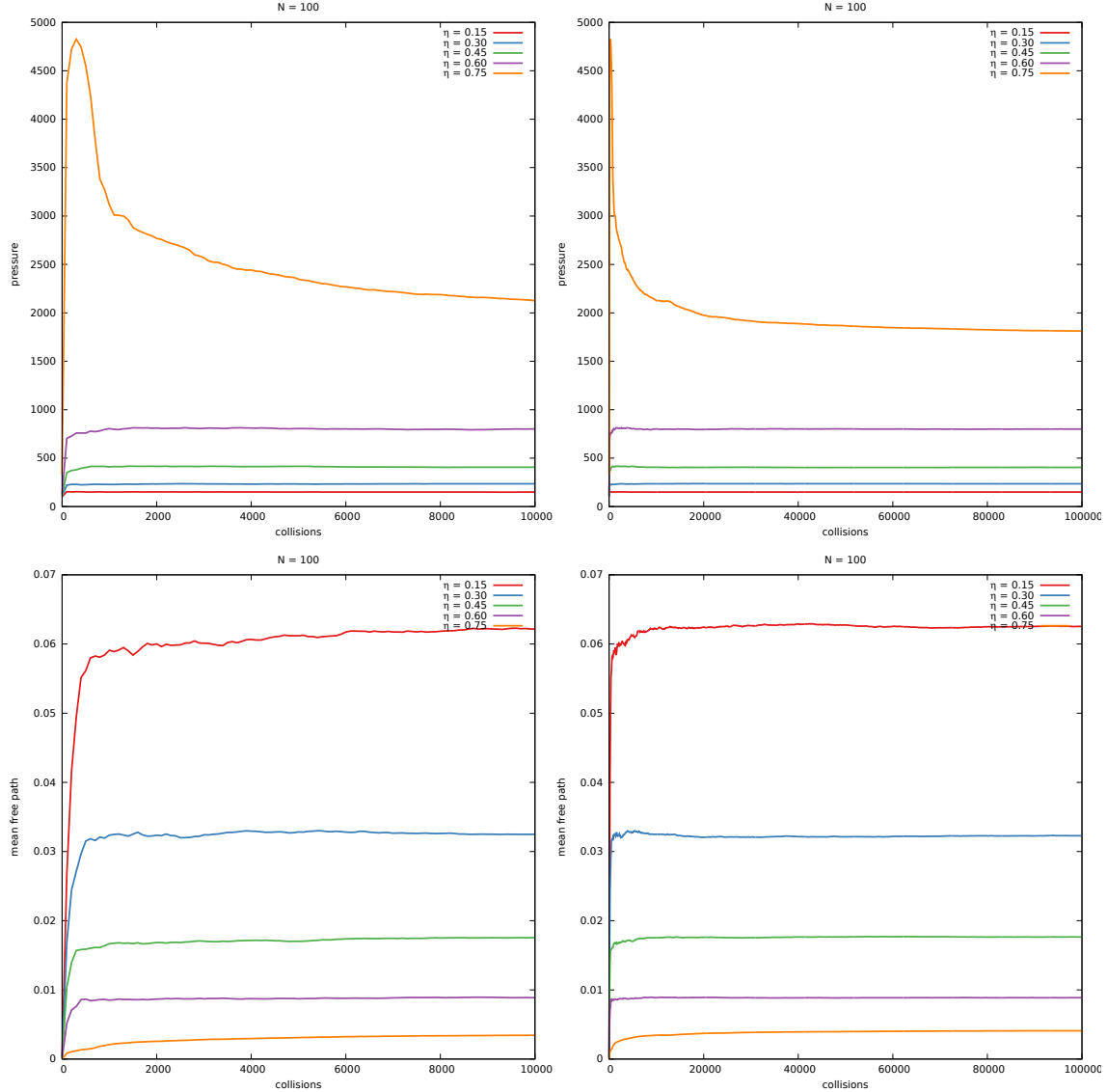


**Figure 2.** Plot of the thermalization process of an hard-core interacting gas of  $N = 100$  particles. The top two figures illustrate the pressure as a function of the number of collisions, while the bottom two show the mean free path of the particles. Different colors represent the different values of  $\eta = 0.15, 0.30, 0.45, 0.60, 0.75$  used for the simulations. On the right is the same process, after a larger number of collisions. The mixing rate of the system (as a function of the number of collisions) grows with  $\eta$  and the number of particles.

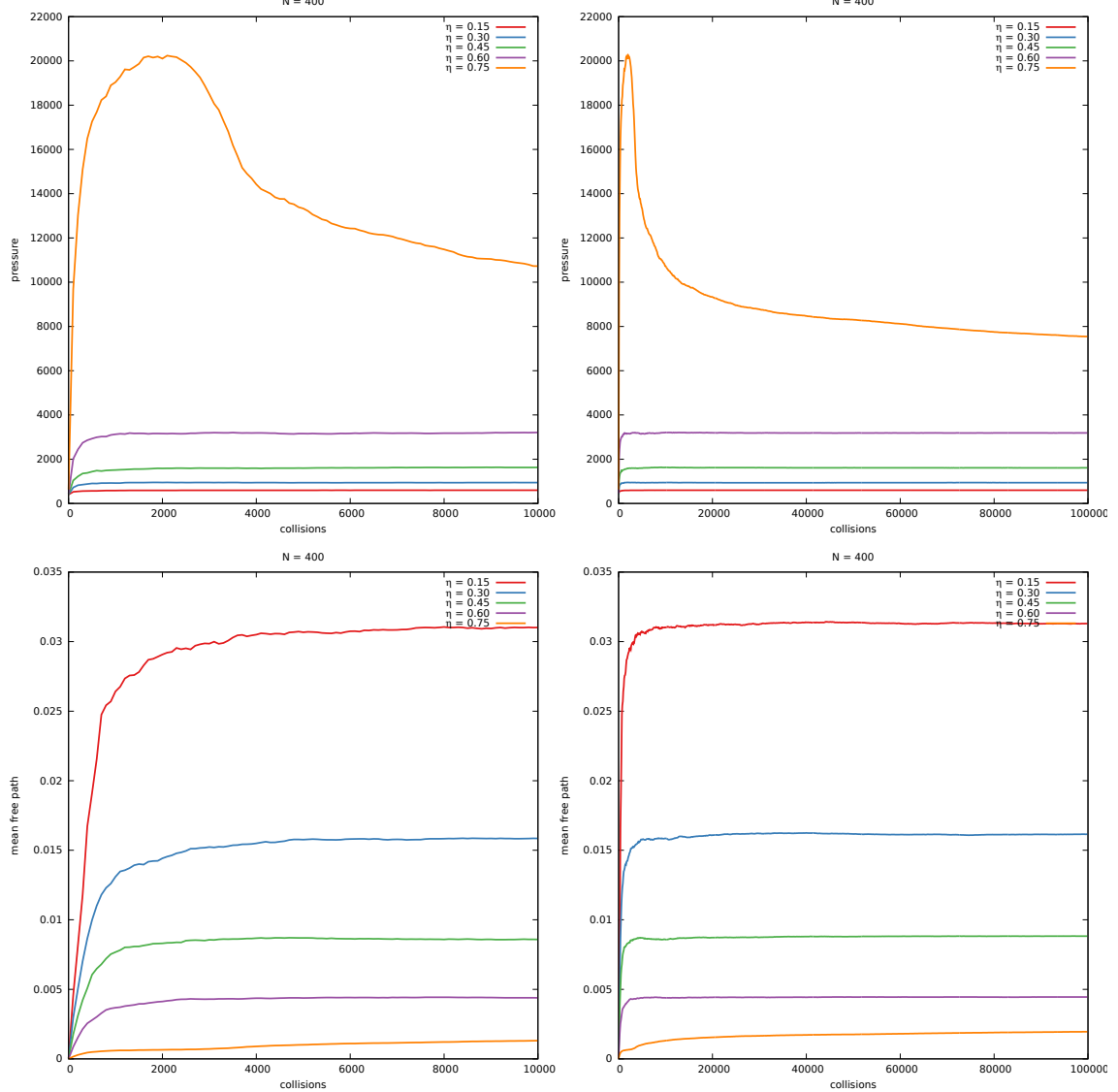


**Figure 3.** Plot of the thermalization process of an hard-core interacting gas of  $N = 400$  particles. The mixing of this larger system is much slower.

A many-body system reaches thermalization only when every particle has interacted with every other particle at least once. Since hard-core particles interact only when they collide with each other, the mixing of this type of systems depends only on the number of collisions and not directly on the elapsed time.

We see that larger systems (system with a large number of particles) need more collisions to mix completely, especially at high densities  $\eta$ , while smaller systems mix faster. At high densities we also note a peak in the pressure curve near the start of the simulation. This is due to the fact that we used an initial arrangement not ideal for the close packing of particles. The particles are initially very close to each other and interact frequently, but after a few collisions they rearrange in such a way as to maximize the distance between them, therefore reducing the pressure (Fig.1).

If we work with  $N = 100$  particles, we can consider the system thermalized after  $5 \cdot 10^5$  collisions.

## 1.2 Momentum Distribution

After thermalization is reached, the system acquires time translation invariance and the distribu-

tion of the momenta of the particles converge to the Maxwell-Boltzmann distribution:

$$f(v) = \sqrt{\left(\frac{m}{2\pi k_b T}\right)^3} 4\pi v^2 \exp\left[-\frac{mv^2}{2k_b T}\right] \quad (6)$$

and for the single components:

$$f(v_i) = \sqrt{\frac{m}{2\pi k_b T}} \exp\left[-\frac{mv_i^2}{2k_b T}\right] \quad (7)$$

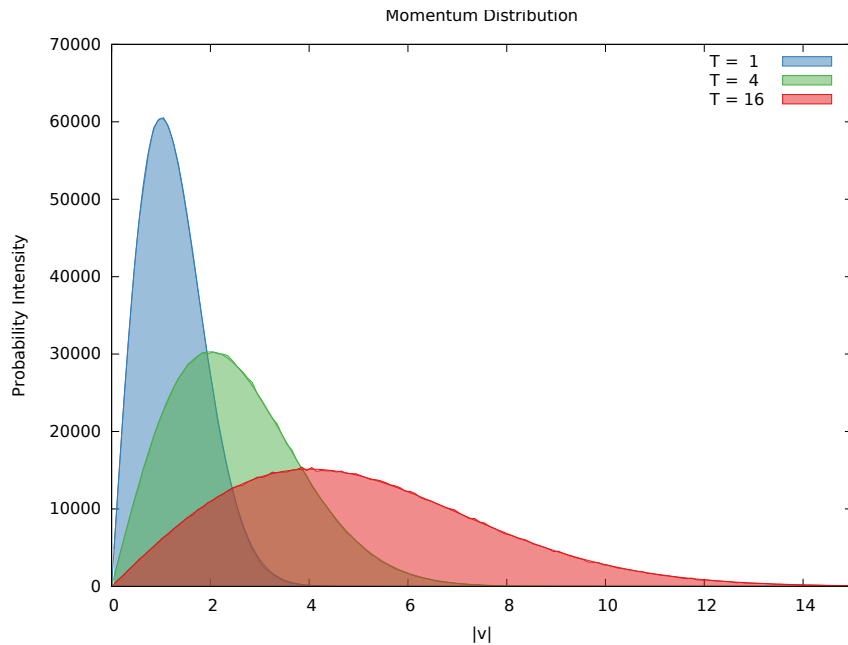


**Figure 4.** Histogram of the modulus of the momenta for  $N = 100$  particles at  $\eta = 0.5$ . The measurements are taken after  $5 \cdot 10^4$  collisions from the start of the simulation, and after that every 500 collisions for a total of  $10^4$  datasets each containing the momenta of  $N$  particles. The system is initialized at temperatures  $T = 1, 4, 16$ .

We repeat the simulation for three different values of the temperature ( $T = 1, 4, 16$ ) which we set by hand at the beginning. The temperature can then be read from a fit of the histograms of (Fig.4) and compared with the one obtained from (5):

$T$	$T_{\text{fit}}$
1	$1.011343 \pm 0.005696$
4	$4.028977 \pm 0.007747$
16	$16.134445 \pm 0.023048$

We also plot the distribution for the single components  $v_x$  and  $v_y$ :

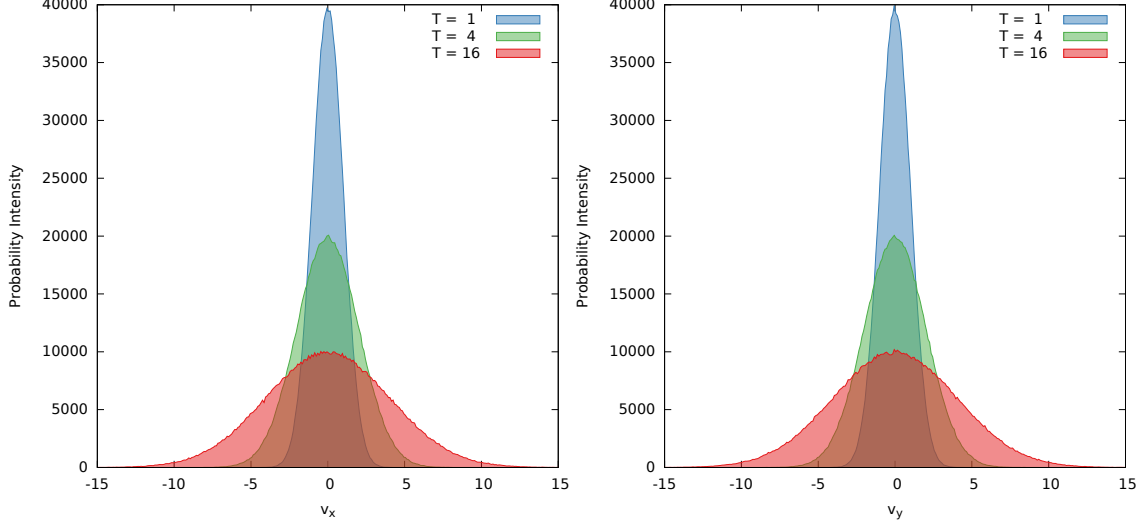


**Figure 5.** Histograms of the  $x$  (left) and  $y$  (right) components of the momenta for  $N = 100$  particles.

*Remark:* in this section we decide not to use adimensional units for time  $t$  and temperature  $k_bT$  otherwise we would end up with only one distribution with  $k_bT = 1$ . What we do is to set only  $k_b = 1$ , this way we still have the freedom to set the temperature  $T$  by rescaling all the momenta (and hence rescale time  $t$  of the right amount in order to balance the change in  $T$ ). For all the following sections we use the rescaling  $L = 1, m = 1$  and  $k_bT = 1$  such that:

$$K = \frac{d}{2} N \quad (8)$$

### 1.3 Phase Transition

In this section we study the  $\eta$  dependence of some interesting quantities describing the system. First we look at the pressure  $P$  as the packing density is increased. For a system such as those in consideration, we define the pressure  $P$  using the formula:

$$\frac{PV}{Nk_bT} = 1 + \frac{1}{2Kt} \sum_{c=1}^{N_c} m \sigma |\Delta \vec{v}_{ij}(t_c)| \quad (9)$$

with  $m\Delta \vec{v}_{ij}(t_c)$  being the exchanged momentum in the collision taking place at time  $t_c$ ,  $N_c$  the total number of collisions and  $t$  the runtime of the simulation.

*Remark:* as a measure against autocorrelation effects we decide to sample data each from an independent run and then take the average over all runs (at the same  $\eta$ ).

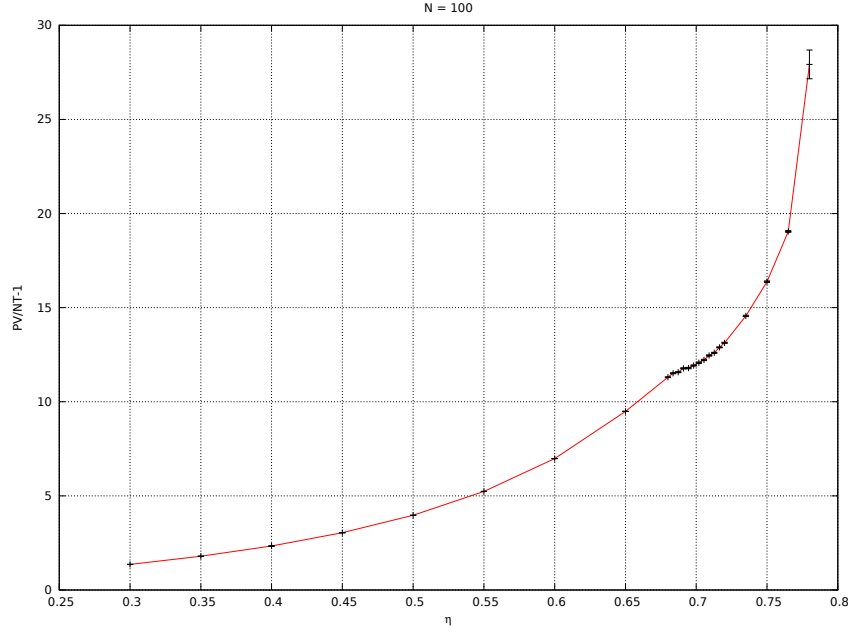


**Figure 6.** Plot of  $\frac{PV}{N k_b T} - 1$  as a function of  $\eta$  for a system of 100 particles. Every measurement is taken from the average of 50 independent runs each collected after an initial thermalization time of  $5 \cdot 10^4$  collisions. The errorbars represent the standard errors of the averages. At large values of  $\eta$  ( $\sim 0.75$ ) the system takes more time to reach thermal equilibrium and this means that measurements are collected when the system is not yet completely mixed. For this reason larger fluctuations are introduced between different simulation runs and the errors are greater.

Near  $\eta = 0.7$  we observe a first order phase transition characterized by a discontinuity in the pressure with respect to the thermodynamic variable  $\eta$ . The system is found in a liquid phase for values of the density  $\eta < 0.7$  and in a solid phase for  $\eta > 0.7$ . This kind of phase transition displays a plateau region where the transition takes place. In fact there is no well defined critical point since multiple phases can coexist near the transition.

We also note that, since the hard-core potential has no attractive effect on the particles, there cannot be a phase transition with respect to the temperature. The order-disorder transition we observe is purely of geometrical nature.

Another thermodynamic quantity that shows discontinuity at the phase transition is the mean free path, i.e., the average distance traveled by a particle between successive impacts:

$$l_c = \sum_{c=1}^{N_c^i} \frac{|\Delta \vec{r}_i(t_c, t_{c-1})|}{N_c^i} \quad (10)$$

To compute  $l_c$ , we save the total distance travelled by every particle  $\sum |\Delta \vec{r}_i| \sim \int |d \vec{r}_i|$  and the total number  $N_c^i$  of collisions it had during its path.

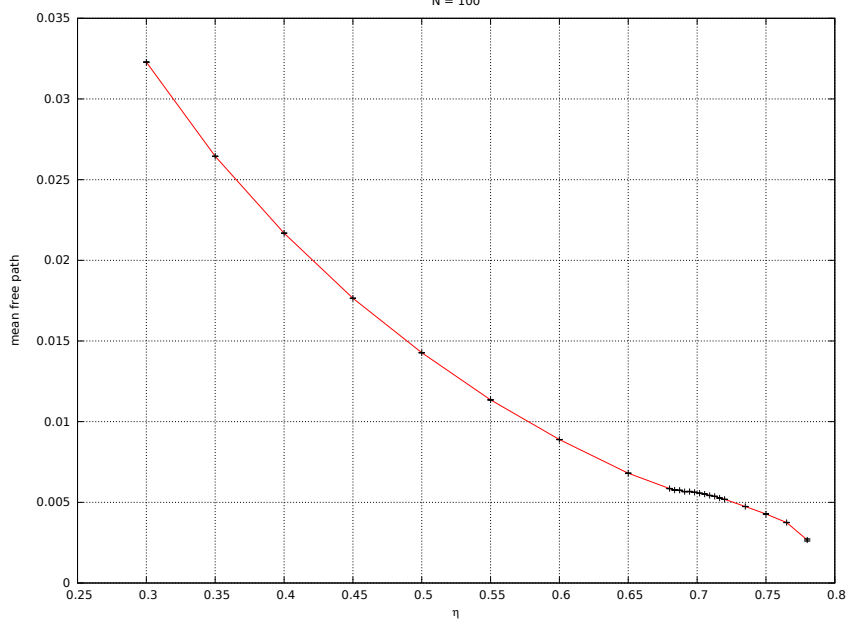


**Figure 7.** Plot of the mean free path against  $\eta$  for  $N = 100$ .

We also plot the distribution of the mean free path:

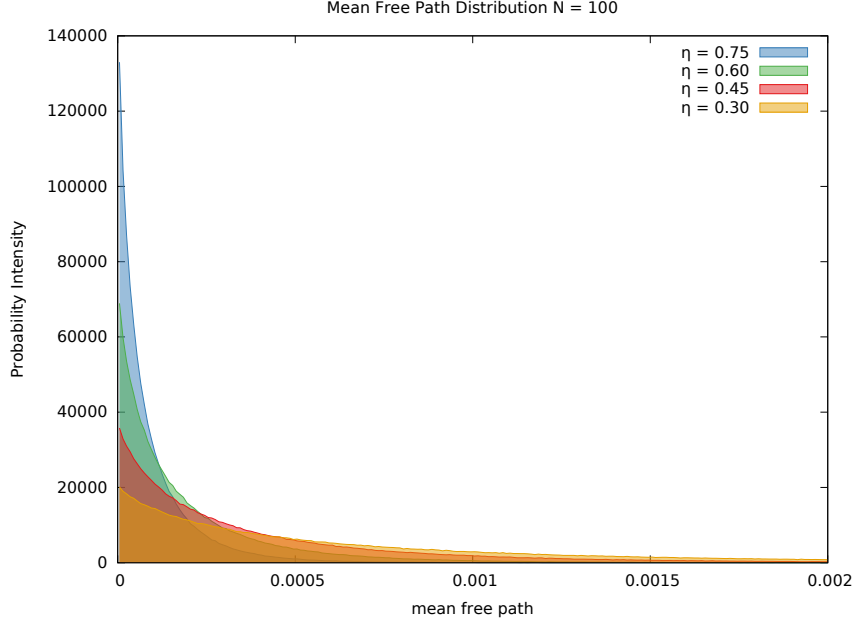


**Figure 8.** Distribution of the mean free path  $l_c$  for  $N = 100$  and  $\eta = 0.30, 0.45, 0.60, 0.75$ . The histograms are obtained from a sample of  $10^6$  measurements and after a thermalization time of  $5 \cdot 10^4$  collisions.

## 1.4 Collision Times

Yet another interesting quantity to look at is the collision time  $t_c$ , i.e., the time between two consecutive collisions. In (Fig.9) we present the distribution of  $t_c$  for increasing values of  $\eta$ :

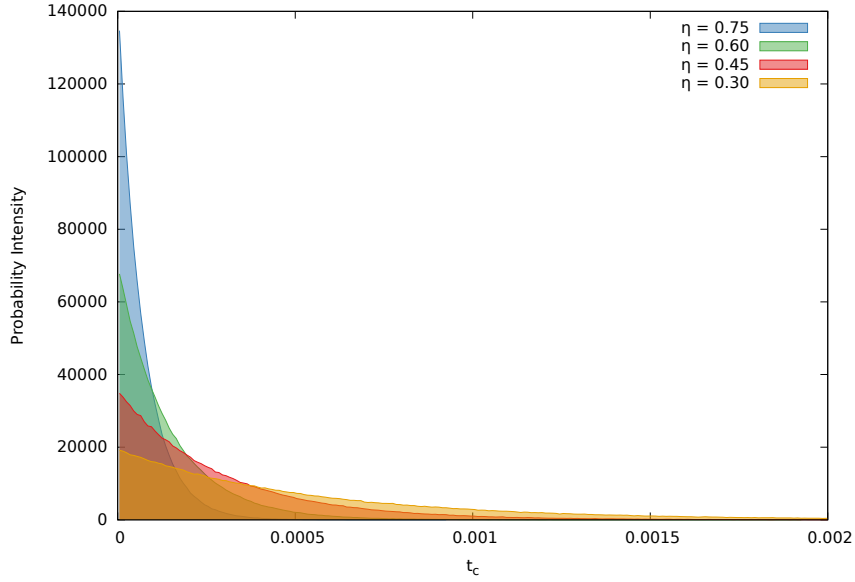


**Figure 9.** Distribution of the collision time  $t_c$  for  $N = 100$  and  $\eta = 0.30, 0.45, 0.60, 0.75$ . The histograms are obtained from a sample of  $10^6$  measurements and after a thermalization time of  $5 \cdot 10^4$  collisions.

As the density of particles increases, the collisions become more frequent because of the decrease in free space available for the particles to freely travel. This implies that the distribution of the collision times must become narrower for larger values of  $\eta$  (Fig.9).

Similarly to the case of the pressure and the mean free path,  $t_c$  also has a discontinuity at the phase transition, as we can see from (Fig.10):

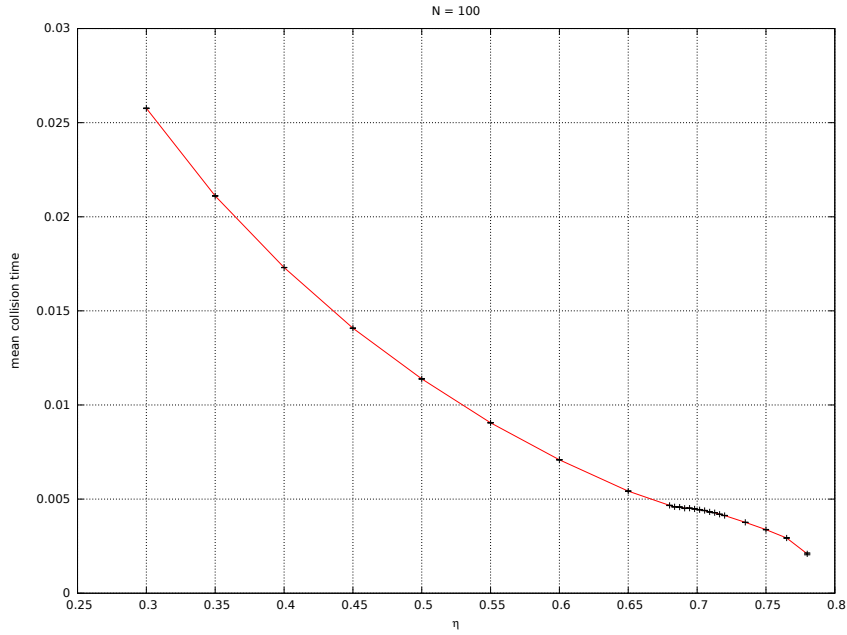


**Figure 10.** Plot of the mean collision time  $\langle t_c \rangle$  against  $\eta$  for  $N = 100$ .

## 1.5 Mean Squared Displacement

The mean squared displacement (MSD), defined as:

$$\text{MSD} = \langle (\vec{r}_i(t) - \vec{r}_i(t_0))^2 \rangle = \langle \Delta \vec{r}(t, t_0)^2 \rangle \quad (11)$$

is a very common measure of the amount of the system “explored” by a particle as the time passes. For diffusion processes (random walks), the MSD grows linearly with time:

$$\text{MSD} \simeq 2 d D \Delta t \quad \text{Einstein's relation} \quad (12)$$

where  $d$  is the dimension of the space and  $D$  is the self-diffusion constant. Usually one would plot the MSD as a function of time and, in the limit of large times, a linear fit of the curve would yield the diffusion coefficient of the process. However, we will see that the use of periodic boundary conditions will affect the linearity of (12). In fact, when a particle travels around a closed loop of non trivial homology, the total displacement computed by (11) is approximately zero, while actually the particle has travelled a distance of the order of the size  $L$  of the system. This phenomenon will effectively confine the particle to a finite volume, and as a consequence, the MSD will reach a plateau value. It is this plateau value that provides the definition of  $D$  for a finite system.

For large  $\Delta t$  this value can be computed exactly: let  $f_i(\vec{r}_0, \vec{r}, t_0, t)$  be the probability of a particle to go from  $\vec{r}_0$  to  $\vec{r}$  after a time  $\Delta t = t - t_0$ , then:

$$\langle (\vec{r}_i(t) - \vec{r}_i(t_0))^2 \rangle = \int_V d\vec{r} \int_V d\vec{r}_0 (\vec{r} - \vec{r}_0)^2 f_i(\vec{r}_0, \vec{r}, t_0, t) \quad (13)$$

$$f(\vec{r}, t) = \int_V f_i(\vec{r}_0, \vec{r}, t_0, t) d\vec{r}_0, \quad f(\vec{r}, t) = \int_V f_i(\vec{r}_0, \vec{r}, t_0, t) d\vec{r}_0, \quad f(\vec{r}_0, t_0) = f(\vec{r}, t) = \frac{1}{V} \quad (14)$$

where the first two equalities are just the definitions of the marginal probability distributions and the last is a consequence of spatial and temporal homogeneity at thermal equilibrium.

After a long time has passed, the particle loses every information about its past, and the joint probability distribution factorizes:

$$f_i(\vec{r}_0, \vec{r}, t_0, t) \xrightarrow{\Delta t \rightarrow \infty} f_i(\vec{r}_0, t_0) f_i(\vec{r}, t) \quad (15)$$

The MSD can then be computed for large time separations as:

$$\begin{aligned} \langle \Delta \vec{r}(t, t_0)^2 \rangle &= \int_V d\vec{r} \int_V d\vec{r}_0 (\vec{r} - \vec{r}_0)^2 f_i(\vec{r}_0, t_0) f_i(\vec{r}, t) \\ &= \int_V d\vec{r} \int_V d\vec{r}_0 (|\vec{r}|^2 - 2\vec{r} \cdot \vec{r}_0 + |\vec{r}_0|^2) f_i(\vec{r}_0, t_0) f_i(\vec{r}, t) \\ &= \frac{1}{V} \int_V d\vec{r} |\vec{r}|^2 - 2 \langle \vec{r}(t) \rangle \cdot \langle \vec{r}_0(t_0) \rangle + \frac{1}{V} \int_V d\vec{r}_0 |\vec{r}_0|^2 \\ &= \frac{2}{V} \int_V d\vec{r} |\vec{r}|^2 \end{aligned} \quad (16)$$

Where the factor 2 in the last step, counts both the displacement of  $\vec{r}$  and  $\vec{r}_0$ , since they are independent. We can fix the initial position of the particle to be 0 for convenience and then look only at the displacement with respect to that position. This is equivalent to considering only the final position contribution, which is half the MSD of (16).

Finally, for a volume  $V = L^d$ , we obtain:

$$\begin{aligned} \langle \Delta \vec{r}(t, t_0)^2 \rangle &= \frac{1}{V} \int_V d\vec{r} |\vec{r}|^2 \\ &= \frac{1}{L^d} \int_{-L/2}^{L/2} dx_d \dots \int_{-L/2}^{L/2} dx_2 \int_{-L/2}^{L/2} dx_1 (x_1^2 + x_2^2 + \dots + x_d^2) \\ &= \frac{1}{L^d} L^{d-1} \frac{2d}{3} \left( \frac{L}{2} \right)^3 = \frac{d}{12} L^2 \xrightarrow{L=1} \begin{cases} 1/6, & d=2 \\ 1/4, & d=3 \end{cases} \end{aligned} \quad (17)$$

By using the time translation invariance of the system (at thermalization) and the fact that all the particles are identical, we can compute an estimate of the MSD by averaging over every time interval  $[t, t + \Delta t]$  and every particle  $i$ :

$$\text{MSD}(\Delta t) = \frac{1}{N} \sum_{i=1}^N \frac{1}{(t_S - \Delta t - t_0 + 1)} \sum_{t=t_0}^{t_S - \Delta t} [\vec{r}_i(t + \Delta t) - \vec{r}_i(t)]^2 \quad (18)$$

with  $t_S$  being the time of the simulation.

We see from (Fig.11) that initially the curves grow linearly with the time separation as one would expect for a diffusive process. For larger separations, though, the MSD reaches the plateau of (17) and fluctuate around it. The measurement taken at very large displacements ( $\Delta t \approx t_S$ ) are of little significance because of the reduced amount of statistics we can collect:

$$N_{\text{samples}}(\Delta t) = (t_S - \Delta t - t_0 + 1) \xrightarrow[t \sim t_S]{} 1$$

We can also see the phase transition of the system in the abrupt drop in the self-diffusion coefficient of the initial diffusive parts of the curves<sup>1</sup>.

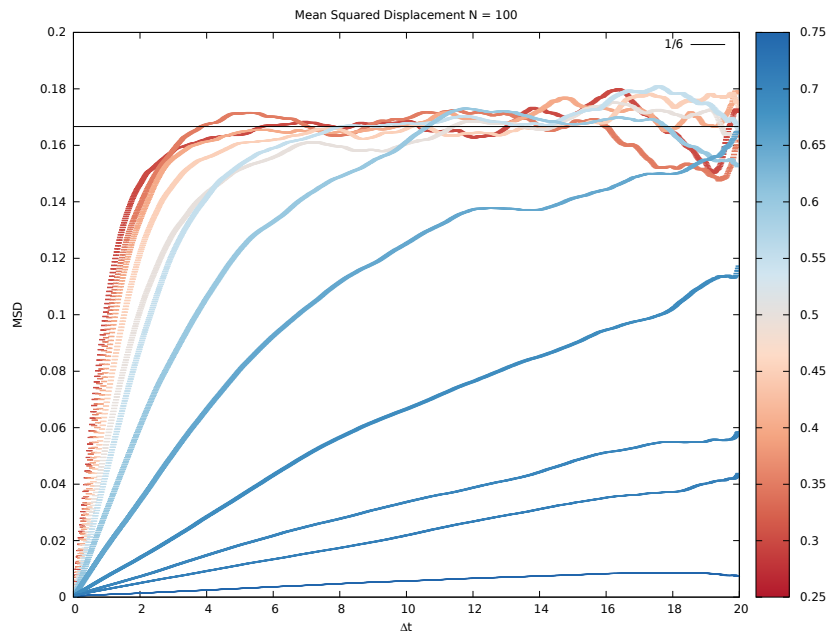


**Figure 11.** Mean squared displacement from a simulation of  $N = 100$  particles. The measurements are taken for a simulation time  $t_S = 20$  with a time step of 0.003 after a thermalization of  $5 \cdot 10^4$  collisions. The color palette represents different values of  $\eta$ . The solid line in black is the exact result for  $\Delta t \rightarrow \infty$ .

As  $\eta$  approaches large values, the particles are more and more constrained by the increase in occupied volume and are less free to travel around (Fig.13). As a consequence they resent much later of the finite size effect of the system, and continue to diffuse linearly with time for much longer (Fig.12):

<sup>1</sup> As already mentioned in (12), the first derivative of the MSD with respect to time is proportional to the self-diffusion coefficient  $D$ .

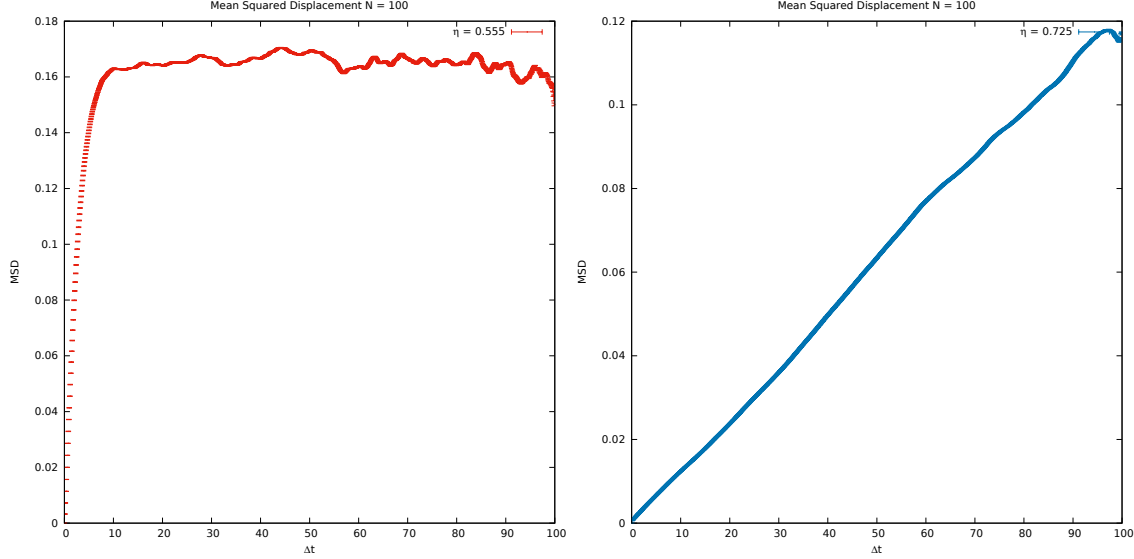


**Figure 12.** Mean squared displacement from a simulation of  $N = 100$  particles at  $\eta = 0.555$  and  $\eta = 0.725$ . The measurements are taken for a simulation time  $t_S = 100$  with a time step of 0.01 after a thermalization of  $5 \cdot 10^4$  collisions.

This is intuitively understood by looking at the trajectory on the right of (Fig.13) and realizing that the particle lives mostly in the bulk of the box and that it almost never travels around a loop of non trivial homology.

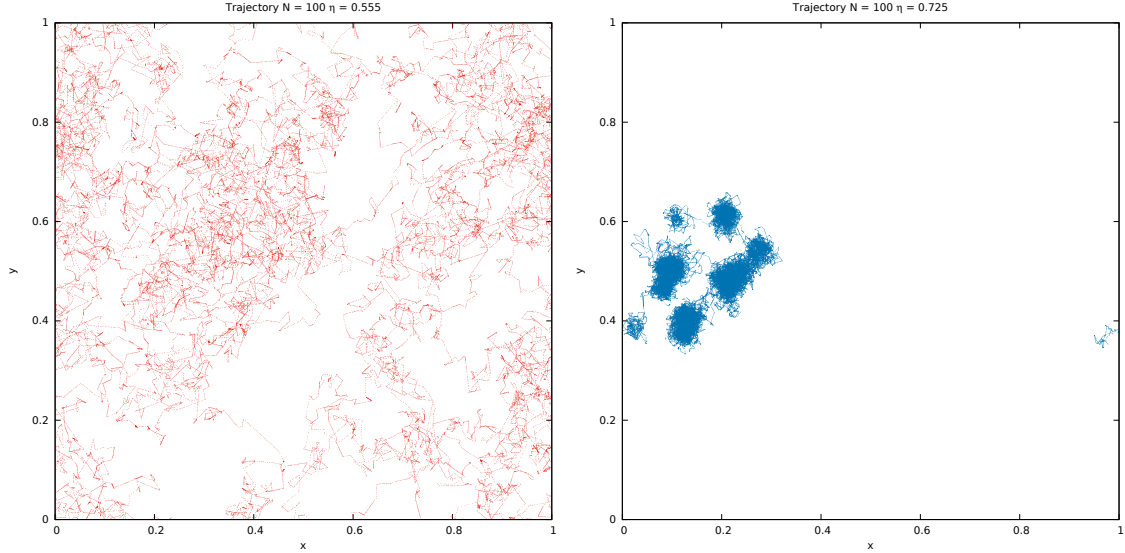


**Figure 13.** Trajectory of a single particle at  $\eta = 0.555$  (left) and  $\eta = 0.725$  (right) in a system with  $N = 100$ . Both simulations had a runtime of  $t_S = 100$  after a thermalization time corresponding to  $5 \cdot 10^4$  collisions.

Another approach is to consider the “unfolded” history (or unfolded coordinates) of the particles, i.e., the trajectories that the particles would have followed if there were no periodic boundary conditions but with the same collisions happening in the “folded” history<sup>2</sup>. The effect of using unfolded coordinates is immediately visible from the plot of the MSD (Fig.15). Having removed the effect of the boudary conditions, the diffusive nature of the process is preserved even at large time intervals, especially for  $\eta \ll 1$  where the confinement of the plateau  $1/6$  was most evident.

<sup>2</sup>. The term “folding” refers to the procedure of obtaining a torus from a quotient of the two-plane, usually the complex plane  $\mathbb{C}$ . Conversely, the unfolding corresponds to the inverse procedure of obtaining a plane from copies of a torus.

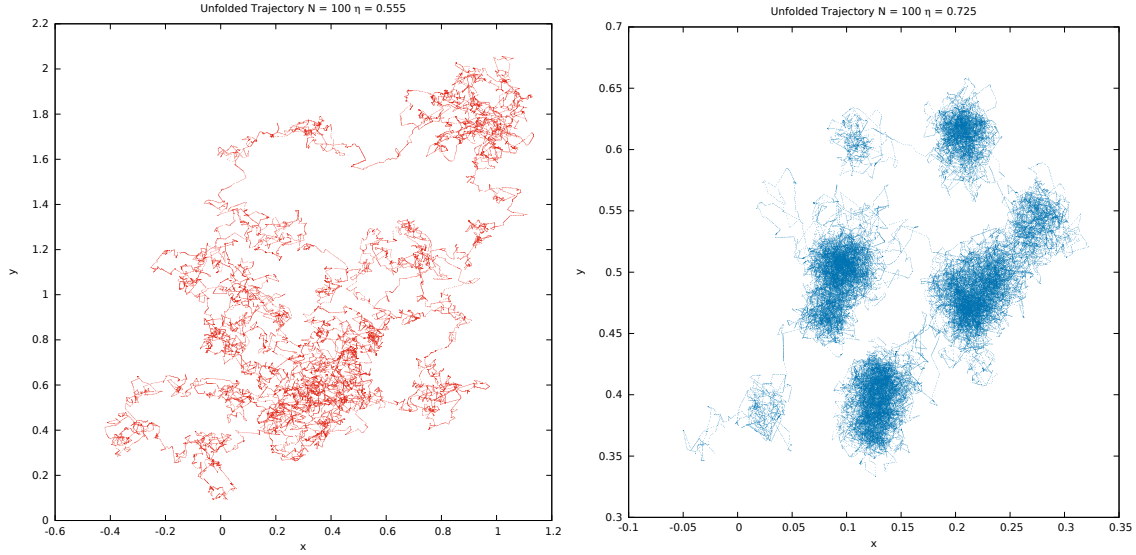


**Figure 14.** Trajectories of the same particles of (Fig.13) but in unfolded coordinates.

As we can see, the unfolding procedure is most effective for lower values of the density, when the particles have more freedom of movement and can cross many times the boundaries from many directions.

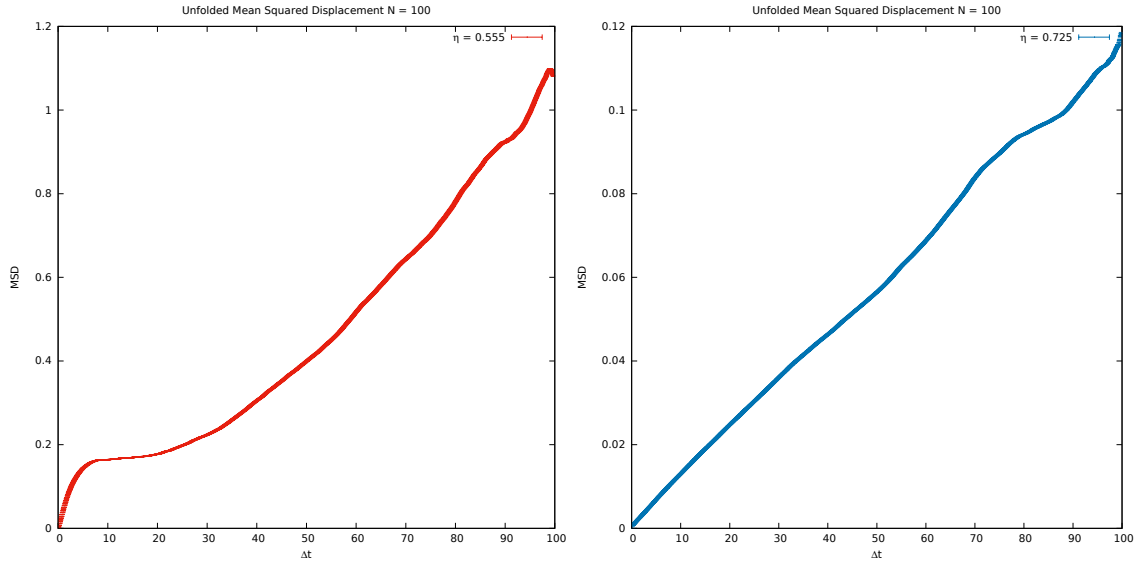


**Figure 15.** Mean squared displacement from an unfolded simulation of  $N = 100$  particles at  $\eta = 0.555$  and  $\eta = 0.725$ . The measurements are taken for a simulation time  $t_S = 100$  with a time step of 0.01 after a thermalization of  $5 \cdot 10^4$  collisions.

# Laboratory of Computational Physics

BY LUCA CASSIA

Dipartimento di Fisica, Università di Milano-Bicocca  
I-20126 Milano, Italy

Email: [l.cassia@campus.unimib.it](mailto:l.cassia@campus.unimib.it)

## Table of contents

<b>1 Hard-Core Molecular Dynamics in 3d</b>	1
1.1 Thermalization	1
1.2 Phase Transition	3
1.3 Mean Squared Displacement	4
1.4 Thermodynamic Limit	5

## 1 Hard-Core Molecular Dynamics in 3d

In this section we repeat the study of molecular dynamics with hard-core central potential for 3d systems. As for the 2-dimensional case, we work with identical particles enclosed in a box with PBCs and use adimensional units of length, time and mass:

$$L = 1, \quad m = 1, \quad k_b T = 1 \quad (1)$$

### 1.1 Thermalization

The system is initialized in a BCC lattice (Fig.1). This type of sphere packing has a packing density:

$$\eta = \frac{N\pi\sigma^3}{6L^3}, \quad \sigma = \sqrt[3]{\frac{6\eta}{\pi N}} L \quad (2)$$

which takes its maximum value for  $\sigma^3 = (3\sqrt{3}L^3)/4N$ :

$$\eta_{\max} = \frac{\pi\sqrt{3}}{8} \approx 0.68017476158... \quad (3)$$

The momenta of the particles are initialized with uniform distribution inside the range  $[-1, 1]$  with total momentum equal to zero (center of mass reference frame). After the initialization the momenta are rescaled in order to obtain the desired temperature. As before, we have the relation between kinetic energy and temperature:

$$K = \frac{d}{2} N k_b T, \quad T = \frac{2}{d N k_b} K \quad (4)$$

We now study the mixing properties of this type of system. We evolve a system of  $N = 100$  particles from its initial configuration, for  $10^4$  collisions and measure the pressure (Fig.1) and the mean free path (Fig.2) every 10 collisions. This procedure is also repeated for  $N = 400$ .

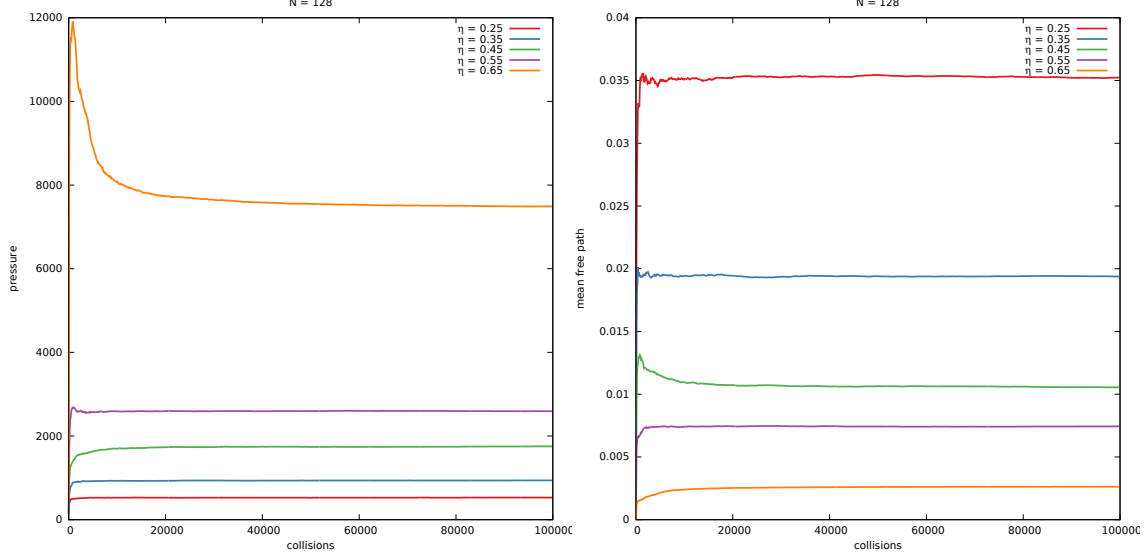


**Figure 1.** Plot of the thermalization process of an hard-core interacting gas of  $N = 128$  particles. On the left is the pressure as a function of the number of collisions, while on the right is the mean free path of the particles. Different colors represent the different values of  $\eta = 0.25, 0.35, 0.45, 0.55, 0.65$  used for the simulations.

We consider the system thermalized after  $5 \cdot 10^4$  collisions where we expect a momentum distribution of the Maxwell-Boltzmann type. The distribution obtained from the simulation confirms our choice of thermalization time:

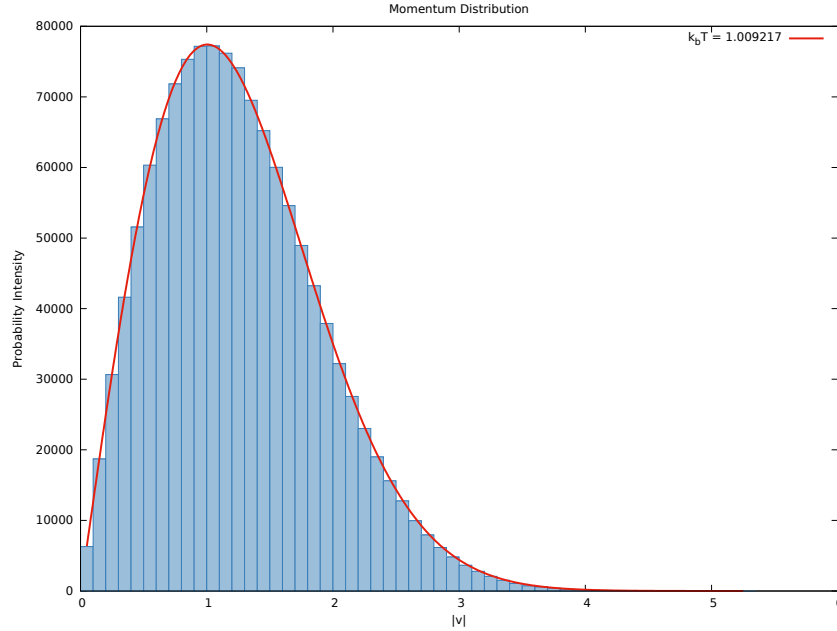


**Figure 2.** Histogram of the modulus of the momenta for  $N = 128$  particles at  $\eta = 0.5$ . The measurements are taken after  $5 \cdot 10^4$  collisions from the start of the simulation, and after that every 500 collisions for a total of  $10^4$  datasets each containing the momenta of  $N$  particles.

By fitting the histogram we obtain the result:

$$k_b T = 1.00922 \pm 0.00559 \quad (5)$$

which is remarkably close to the numerical value  $k_b T = 1$  that was set at the beginning of the simulation.

## 1.2 Phase Transition

In this section we study the  $\eta$  dependence of the pressure  $P$  for a system of  $N = 250$  particles. As for the 2-dimensional case we use the formula:

$$\frac{PV}{Nk_b T} = 1 + \frac{1}{2Kt} \sum_{c=1}^{N_c} m \sigma |\Delta \vec{v}_{ij}(t_c)| \quad (6)$$

Again the measurements are taken by averaging over independent simulation runs in order to reduce autocorrelation effects. Every point of in (Fig.3) is the mean value of 10 independent simulation thermalized for a time corresponding to  $5 \cdot 10^4$  collisions.

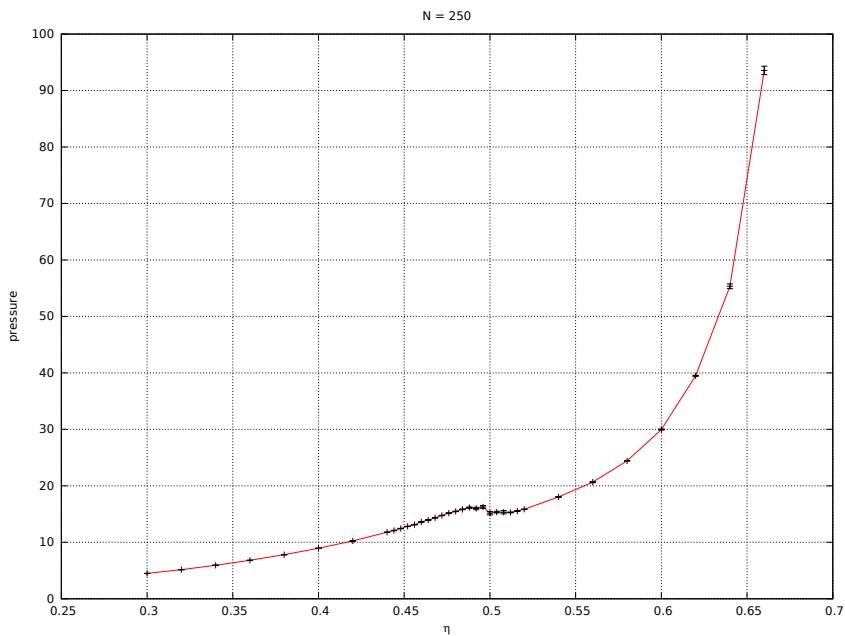


**Figure 3.** Plot of  $\frac{PV}{Nk_b T} - 1$  as a function of  $\eta$  for a system of 250 particles. Every measurement is taken from the average of 10 independent runs each collected after an initial thermalization time of  $5 \cdot 10^4$  collisions. The errorbars represent the standard errors of the averages.

For the 3 dimensional case at study, we notice a discontinuity of the pressure around the value  $\eta \sim 0.5$ . Near the transition point the measurements are averaged over the two metastable branches of the curve, thus forming almost a plateau, which is a typical property of first order phase transitions.

### 1.3 Mean Squared Displacement

Informations about the phase of the system and about its diffusive/confined properties are also found by looking at the mean squared displacement:

$$\text{MSD} = \langle (\vec{r}_i(t) - \vec{r}_i(t_0))^2 \rangle = \langle \Delta \vec{r}(t, t_0)^2 \rangle \quad (7)$$

which, for a 3 dimensional system enclosed in a box with edge  $L=1$ , has a plateau at:

$$\lim_{\Delta t \rightarrow \infty} \text{MSD}_{3d} = \frac{L^2}{4} = 0.25 \quad (8)$$

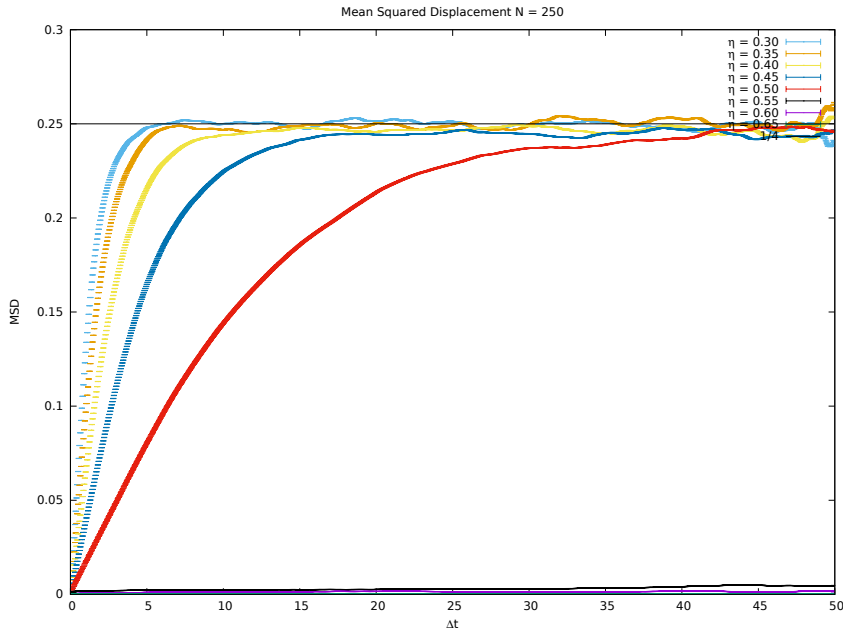


**Figure 4.** Mean squared displacement from a simulation of  $N = 250$  particles. The measurements are taken for a simulation time  $t_S = 50$  with a time step of 0.005 after a thermalization of  $5 \cdot 10^4$  collisions. The color palette represents different values of  $\eta$ . The solid line in black is the exact result for  $\Delta t \rightarrow \infty$ .

From the growth of the MSD with time, we note a similar behavior to that of the 2 dimensional case. This time, though, the discontinuity in the rate of change of the coefficient  $D$  with respect to  $\eta$  is even more drastic. For  $\eta < 0.5$  the particles have an initial diffusive dynamics that becomes

confined when the plateau value 0.25 is reached. Immediately after  $\eta \sim 0.5$  the diffusion coefficient drops almost to zero and we witness a transition to a solid phase of the system where the particles are strongly confined by the small space available.

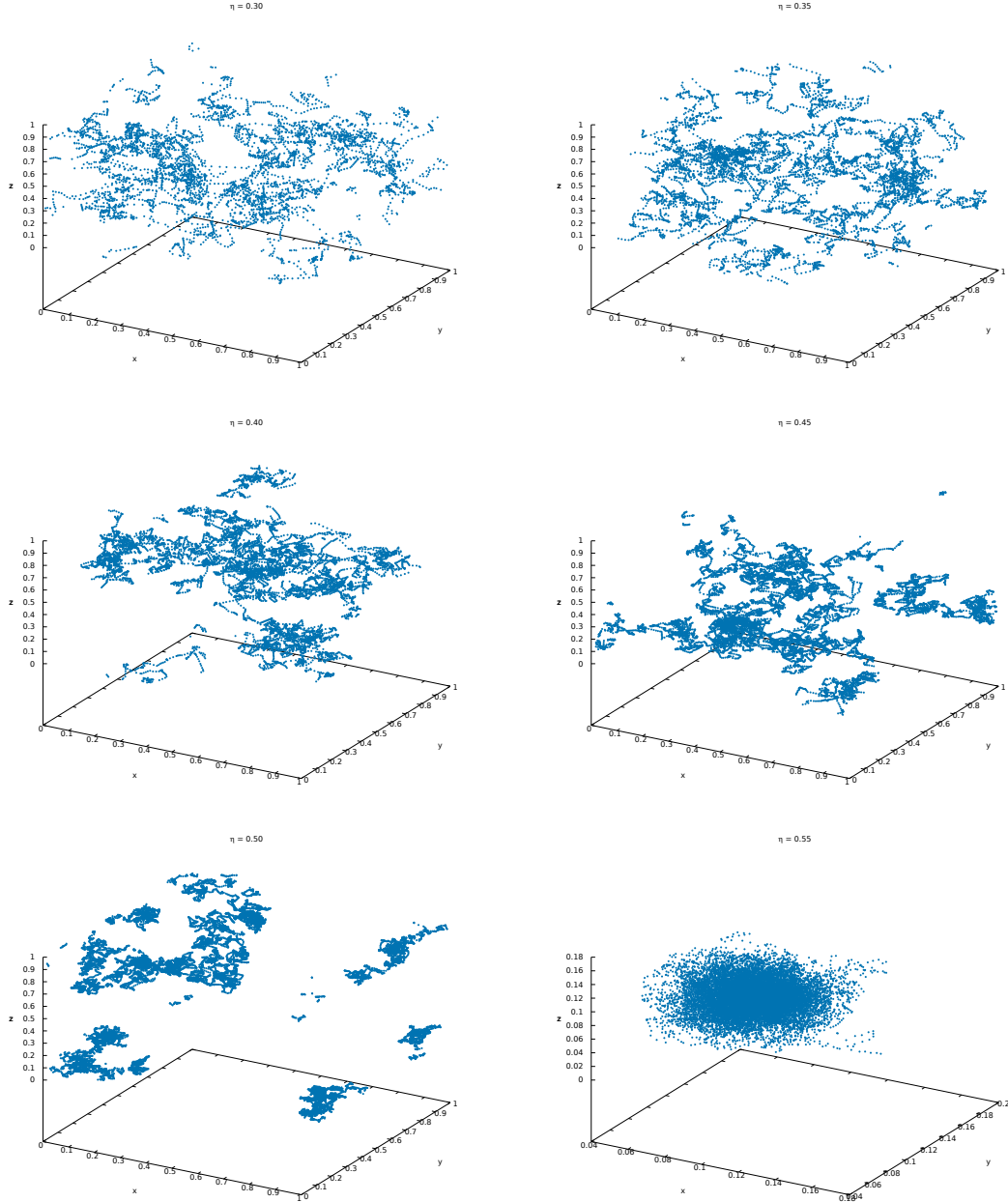


**Figure 5.** Points visited by individual particles in a system of  $N = 250$  total particles, at different values of the packing density  $\eta$ . The first five picture represent the typical trajectories of diffusion processes such as random walks (liquid phase). In the last picture is evident the confining property of the solid phase of the system.

## 1.4 Thermodynamic Limit

Finally we study the thermodynamic limit of the pressure by taking several measurements at

growing values of  $V$  and  $N$  keeping the density  $\eta$  fixed (instead of actually scaling the volume  $V$  we increase the number of particles and reduce their diameter so that  $\eta = \text{const}$ ).

We consider systems with  $N = 32, 64, 128, 256, 512$  and measure the quantity:

$$\frac{PV}{Nk_bT} - 1 = \frac{m\sigma}{2Kt} \sum |\Delta \vec{v}_{ij}| \quad (9)$$

at the fixed value  $\eta = 0.3$ . We then plot the results against  $1/L$  and perform a linear fit of the form:

$$y = p_0 + p_1 x \quad (10)$$

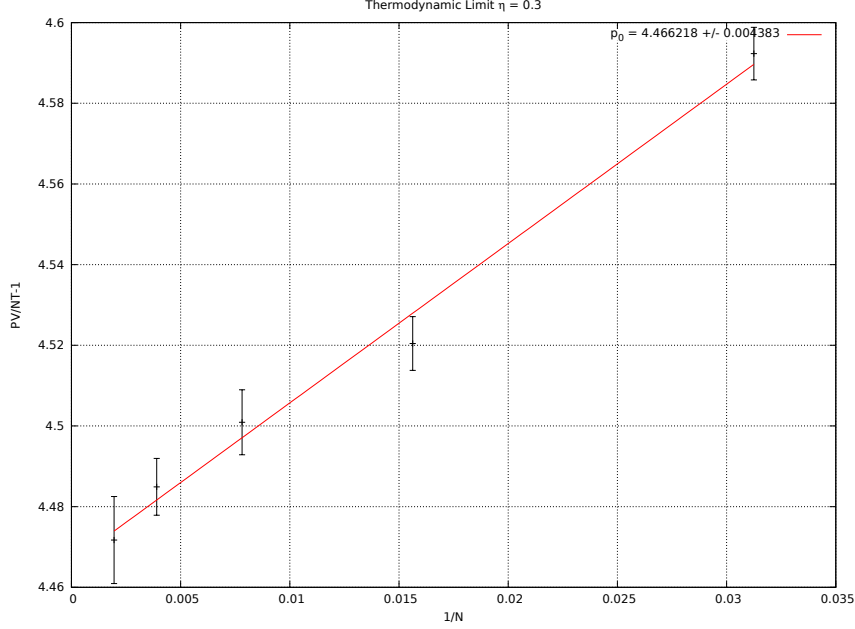


**Figure 6.** Plot of  $\frac{PV}{Nk_bT} - 1$  as a function of  $1/L$ . Each point is taken after thermalization and averaged over 10 independent simulation runs. The errors are computed as the standard error on the mean values.

The result of the fit indicates that:

$$\lim_{N \rightarrow \infty} \frac{PV}{Nk_bT} - 1 = 4.4662 \pm 0.0044 \quad (11)$$

# Laboratory of Computational Physics

BY LUCA CASSIA

Dipartimento di Fisica, Università di Milano-Bicocca  
I-20126 Milano, Italy

Email: [l.cassia@campus.unimib.it](mailto:l.cassia@campus.unimib.it)

## Table of contents

1 Soft-Core Molecular Dynamics in 3d . . . . .	1
1.1 Thermalization . . . . .	3
1.2 Momentum Distribution . . . . .	4
1.3 Potential Energy and Fluctuations . . . . .	4
1.4 Energy, Temperature and Pressure . . . . .	6
1.5 Mean Squared Displacement . . . . .	6
1.6 Thermodynamic Limit . . . . .	7

## 1 Soft-Core Molecular Dynamics in 3d

We now consider a system of  $N$  particles enclosed in a box with PBC and interacting through a smooth central potential which is repulsive at short range and attractive at large distances. The most common form of this kind of potential is the **Lennard-Jones** (L-J) potential:

$$U(r) = 4 \varepsilon \left[ \left( \frac{\sigma}{r} \right)^{12} - \left( \frac{\sigma}{r} \right)^6 \right], \quad r = |\vec{x}| \quad (1)$$

where  $\varepsilon$  is the depth of the potential well,  $\sigma$  is the finite distance at which the inter-particle potential is zero and  $r$  is the distance between the particles. Upon differentiation we obtain the force acting between pair of particles:

$$F(r) = -\frac{\partial}{\partial r} U(r) = 24 \frac{\varepsilon}{\sigma} \left[ 2 \left( \frac{\sigma}{r} \right)^{13} - \left( \frac{\sigma}{r} \right)^7 \right] \quad (2)$$

To save computational time and satisfy the minimum image convention, the Lennard-Jones potential is often truncated at a cut-off distance of  $r_c = 2.5 \sigma$ , where:

$$U(r_c) = 4 \varepsilon \left[ \left( \frac{1}{2.5} \right)^{12} - \left( \frac{1}{2.5} \right)^6 \right] \approx -0.0163 \varepsilon \quad (3)$$

At distances larger than  $r_c$  the potential is less than  $\frac{1}{60}$  the minimum value  $\varepsilon$ , therefore the truncation gives us a good approximation of the full potential. As a consistency measure, we assume  $r_c < L$ , with  $L$  being the size of the box ( $L^d = V$ ).

Since the truncation introduces a jump discontinuity at the cut-off distance, we need to shift the potential upward so that  $U(r_c) = 0$  and also impose that the first derivative is continuous in

the interval  $(0, \infty)$ . The truncated and shifted potential is defined as follows:

$$U_{\text{trunc}}(r) = \begin{cases} U(r) - U(r_c) + (r - r_c) F(r_c) & \text{for } r \leq r_c \\ 0 & \text{for } r > r_c \end{cases} \quad (4)$$

where  $F(r_c)$  is the value of the force at the cut-off:

$$F(r_c) = 24 \frac{\varepsilon}{\sigma} \left[ \left( \frac{1}{2.5} \right)^{13} - \left( \frac{1}{2.5} \right)^7 \right] \approx -0.039 \frac{\varepsilon}{\sigma} \quad (5)$$

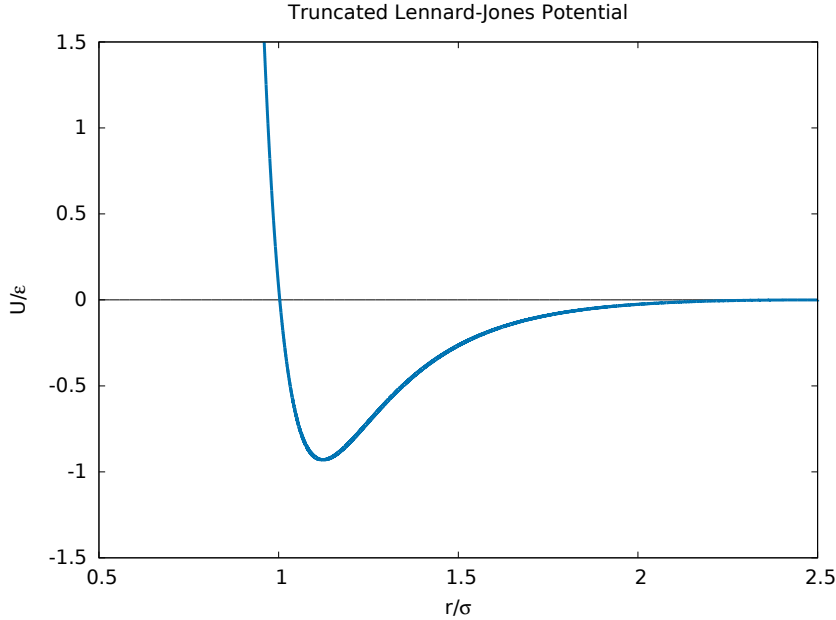


**Figure 1.** Plot of the truncated L-J potential.

Since the L-J potential depends only upon the two parameters  $\sigma$  and  $\varepsilon$ , which determine the length and energy scales of the system, we can choose to work in adimensional units where:

$$m = 1, \quad \sigma = 1, \quad \varepsilon = 1, \quad L \neq 1 \quad (6)$$

The time evolution of the system is obtained by numerical integration of the equations of motion. The method employed is the **Velocity Verlet** algorithm, which consists of the four steps:

1. half step velocity update:  $\vec{v}(t + \frac{1}{2}\Delta t) = \vec{v}(t) + \frac{1}{2}\vec{a}(t)\Delta t$
2. full step position update:  $\vec{x}(t + \Delta t) = \vec{x}(t) + \vec{v}(t + \frac{1}{2}\Delta t)\Delta t$
3. recompute accelerations:  $\vec{a}(t + \Delta t) = \frac{1}{m}\vec{F}(t + \Delta t)$
4. half step velocity update:  $\vec{v}(t + \Delta t) = \vec{v}(t + \frac{1}{2}\Delta t) + \frac{1}{2}\vec{a}(t + \Delta t)$

where in step (2) we must apply periodic boundary conditions in each of the  $d$  directions. The unit time interval is chosen to be  $\Delta t = 0.001$ .

For conservative systems, it can be shown that the energy of the Verlet approximation essentially oscillates around the constant energy of the exactly solved system, with a global error bound of order  $\mathcal{O}(\Delta t^2)$ .

*Technical Note:* in order to further reduce the computational cost of the algorithm, we construct a table  $T_{ij}$  in which we save, for each particle  $i$ , the list of neighbouring particles  $j$  at distances  $r_{ij} < 2.8 \sigma = r_m$ . Only the particles inside the neighbour list are taken into account in the calculations of the accelerations. The list itself is then updated once every 10 evolution steps to keep up with the movement of the particles.

## 1.1 Thermalization

Particles are initialized in a regular BCC lattice structure with momenta randomly assigned in the multi interval  $[-1, 1]^d$ . The instantaneous temperature  $kT = \frac{2}{d}K$  can then be set to a desired value  $kT'$  by rescaling the momenta as:

$$p_i \rightarrow p'_i = p_i \sqrt{\frac{kT'}{kT}} \quad (7)$$

While the mechanical energy  $H = K + U$  is conserved in time, the kinetic energy  $K$  and the temperature  $kT$  are not, hence the rescaling of (7) must be repeated at regular intervals until thermalization is reached.

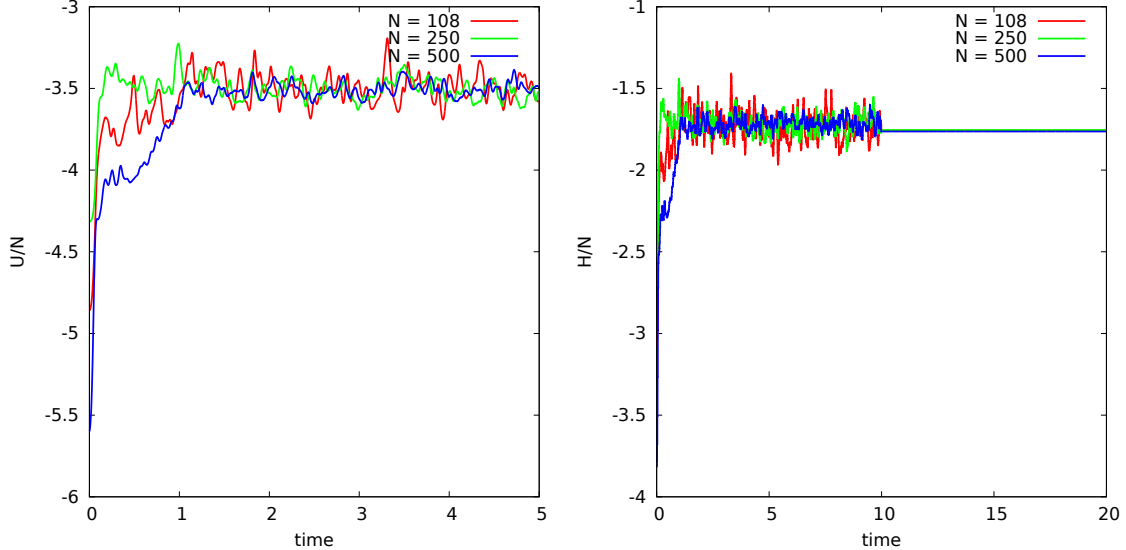


**Figure 2.** Thermalization of a system of softcore particles at density  $\rho = 0.7$ ,  $kT = 1.19$  for  $N = 108, 250, 500$ . On the left we show the evolution of the density of potential energy  $U/N$  in the first 5000 integration steps. On the right is the total energy density  $H/N$ , first during the thermalization phase ( $0 < t < 10$ ), in which the temperature is kept constant, and then in the measurement phase ( $t > 10$ ) when the energy  $H$  is constant.

We define the *density* of the system as:

$$\rho = \frac{N\sigma^d}{L^d} \implies L = \sigma \left( \frac{N}{\rho} \right)^{\frac{1}{d}} \quad (8)$$

and, since  $\sigma = 1$ , we can choose to define the properties of the system by setting some values for  $N$  and  $\rho$ , thus automatically fixing the value of  $L$ .

## 1.2 Momentum Distribution

Because the system in exam is not an ideal gas, the probability distribution of the momenta could in principle be quite different from the Maxwell-Boltzmann distribution. However, the L-J potential is still a good approximation of that of an ideal gas especially at low densities where the gas is very rarefied.

In (Fig.3) we show that a gas of  $N = 250$  particles at  $\rho = 0.5$  and  $k T = 1$ , reaches thermal equilibrium with a Maxwell Boltzmann distribution:

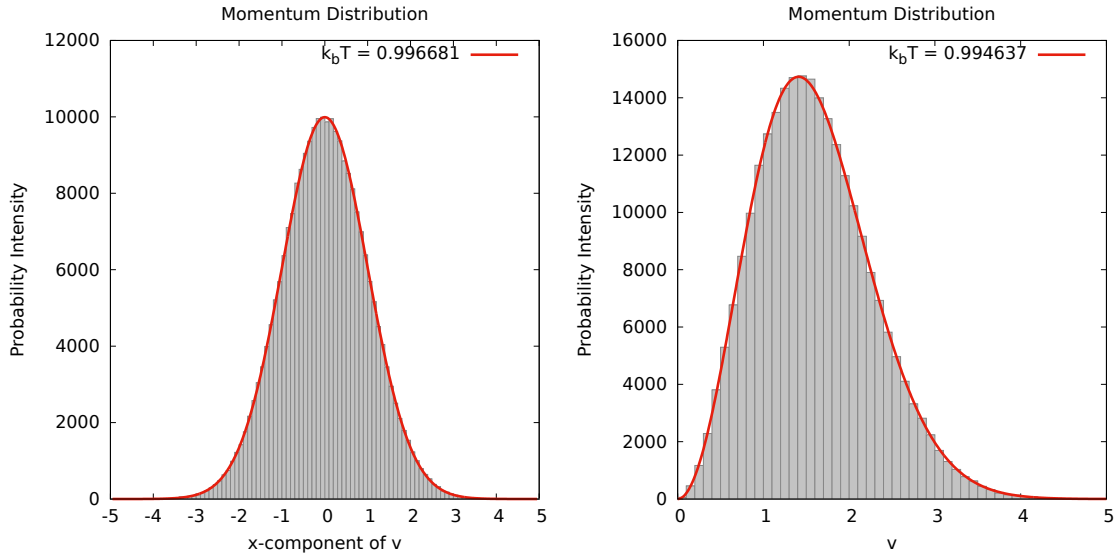


**Figure 3.** Momentum distributions for a system of  $N = 250$  particles at  $\rho = 0.5$  and  $k_b T = 1.0$ . On the left is the  $v_x$  distribution and on the right is the distribution of the modulus of the momentum. The measurements were taken every 100 evolution steps for  $10^5$  steps, each time collecting the momenta of every particle thus giving a total of 250000 samples. The simulation was preceded by a thermalization phase of  $t_{\text{therm}} = 5000 \Delta t = 5$ . The red lines represent fits with Maxwell-Boltzmann distributions.

We can compare the initial temperature of the simulation with the widths of the distributions to establish if the system has reached equilibrium at the right temperature. The results of the fit are in fact in good accordance with the chosen value  $k T = 1.0$  :

$$\begin{aligned} k T &= 0.997 \pm 0.003 \quad (v_x \text{ fit}) \\ k T &= 0.995 \pm 0.002 \quad (|\vec{v}| \text{ fit}) \end{aligned}$$

## 1.3 Potential Energy and Fluctuations

We define the density of potential (internal) energy:

$$u = \frac{U}{N} \tag{9}$$

as the average potential energy associated to each particle, and study its fluctuations around the mean value  $\langle u \rangle$ , since, as pointed out before, the quantities  $K$  and  $U$  are not conserved individually but only as the sum  $H = K + U$ .

We compute the time evolution of the observable  $u$  for systems of  $N = 108, 250, 500$  particles at density  $\rho = 0.7$  and initial temperature  $kT = 1.19$ .

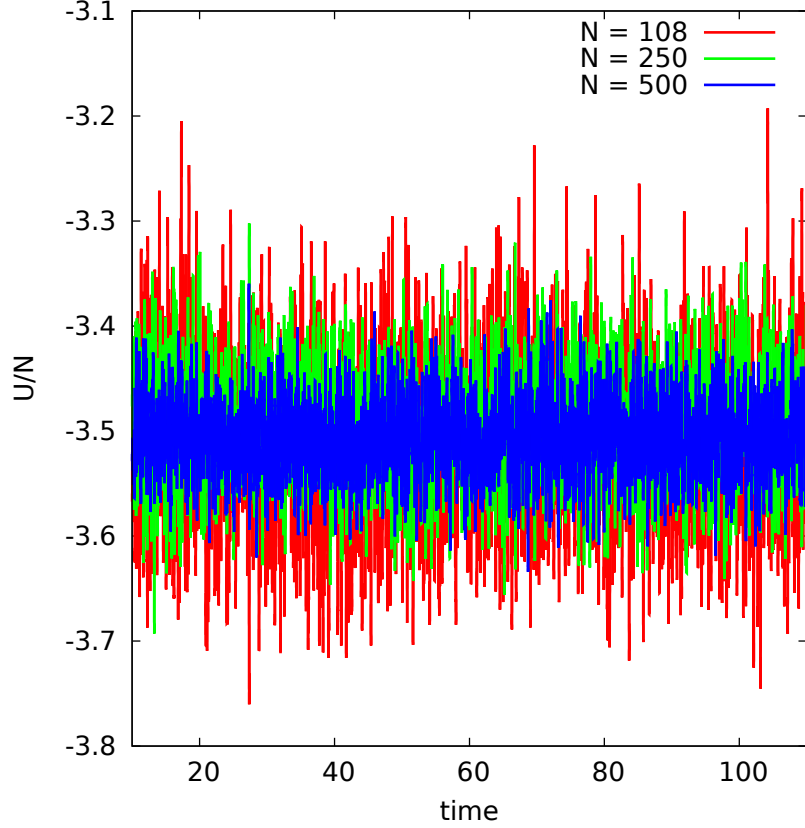


**Figure 4.** Internal energy density  $u$  for  $N = 108, 250, 500$  at  $\rho = 0.7$  and  $kT = 1.19$ . Thermalization time  $t_{\text{term}} = 10$  and total time of the simulation  $t = 100$  ( $\Delta t = 0.001$ ). During the thermalization phase the momenta were rescaled every 10 steps in order to fix the temperature to the desired value.

$N$	$\langle u \rangle$	$\Delta u$
108	-3.5141	0.0760
250	-3.4948	0.0501
500	-3.5066	0.0358

These results were obtained by averaging over a set of  $10^3$  measurements taken once every 100 evolution steps in order to reduce autocorrelation effects. The measurement phase was also preceded by a thermalization time  $t_{\text{therm}} = 10$ .

We immediately notice that the amplitude of the fluctuations decreases as the number of particle  $N$  gets larger. In fact, for a macroscopic system, we expect both the variance and the mean of the energy to scale as  $N$ , hence:

$$\frac{\Delta U^2}{\langle U \rangle^2} = \frac{\langle U^2 \rangle - \langle U \rangle^2}{\langle U \rangle^2} \sim \frac{1}{N} \xrightarrow{N \rightarrow \infty} 0 \quad (10)$$

As a consequence, if we consider the density  $u$ , we have:

$$u = \frac{U}{N} \sim \frac{N}{N} = 1, \quad \Delta u = \sqrt{\langle (u - \langle u \rangle)^2 \rangle} = \frac{\Delta U}{N} \sim \frac{\sqrt{N}}{N} = \frac{1}{\sqrt{N}} \xrightarrow[N \rightarrow \infty]{} 0 \quad (11)$$

which implies:

$$\Delta u \cdot \sqrt{N} \sim \text{const.} \quad \begin{cases} 0.0760 \cdot \sqrt{108} \approx 0.789815... \\ 0.0501 \cdot \sqrt{250} \approx 0.792151... \\ 0.0358 \cdot \sqrt{500} \approx 0.800512... \end{cases}$$

This is actually the well known result that, in the thermodynamic limit, the energy of a grand-canonical ensemble converges to its expectation value, thus giving a physically equivalent description to that of a micro-canonical ensemble.

## 1.4 Energy, Temperature and Pressure

Another quantity of interest for a soft-core interacting gas is the pressure, defined using the **virial theorem**:

$$\frac{PV}{NkT} = \frac{P\sigma^3}{\rho kT} = 1 + \frac{1}{dNkT} \sum_{i < j} \langle \vec{r}_{ij} \cdot \vec{F}_{ii} \rangle \quad (12)$$

where the sum ranges over all the pairs of particles and  $\langle \rangle$  represents the time average. If the system had the properties of an ideal gas, then the previous formula would yield zero because there would not be any interaction between particles. In the case of a L-J potential we can use the measurement of the pressure as an indicator of the deviation from the ideal gas behavior.

In this section we consider a system of  $N=108$  particles at  $\rho=0.6$  and temperature  $kT=1.22$ . We simulate for a total time  $t=110$  with  $\Delta t=0.001$  and with the first  $10^4$  timesteps ( $t=10$ ) dedicated to the thermalization of the system during which the temperature is reset every 10 steps.

The averages and standard deviations on the observables are computed with data collected every 100 steps, in order to reduce autocorrelation effects.

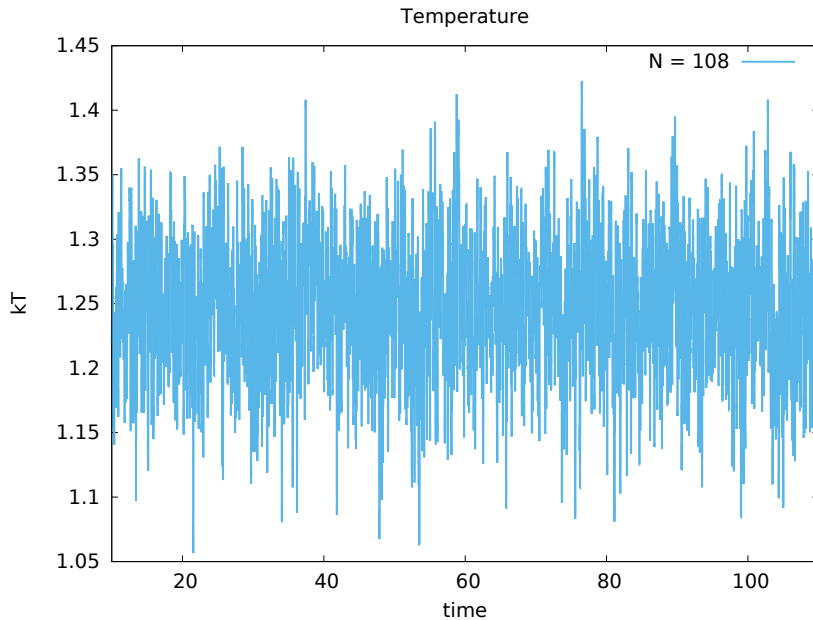


**Figure 5.** Temperature as a function of time for  $N=108$ ,  $\rho=0.6$  and initial temperature  $kT=1.22$ .

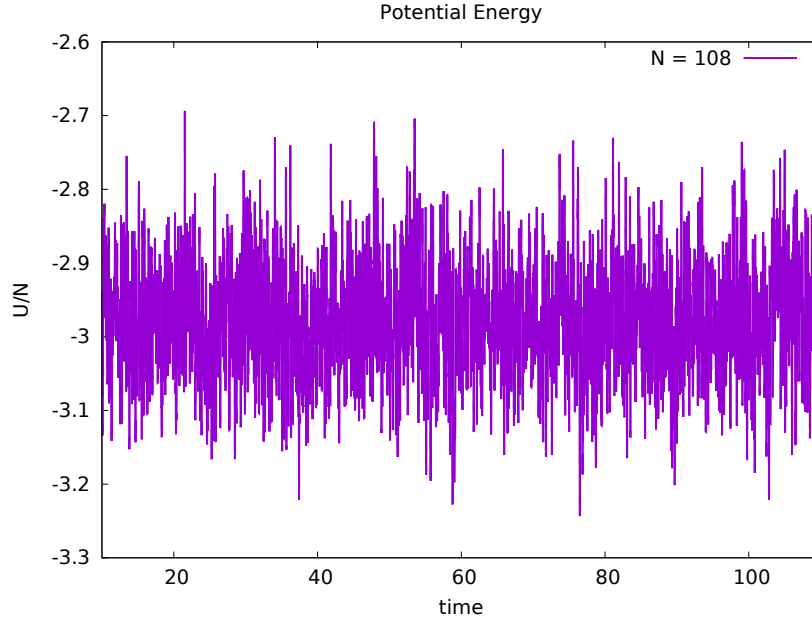


**Figure 6.** Potential energy as a function of time for  $N = 108$ ,  $\rho = 0.6$  and initial temperature  $kT = 1.22$ .

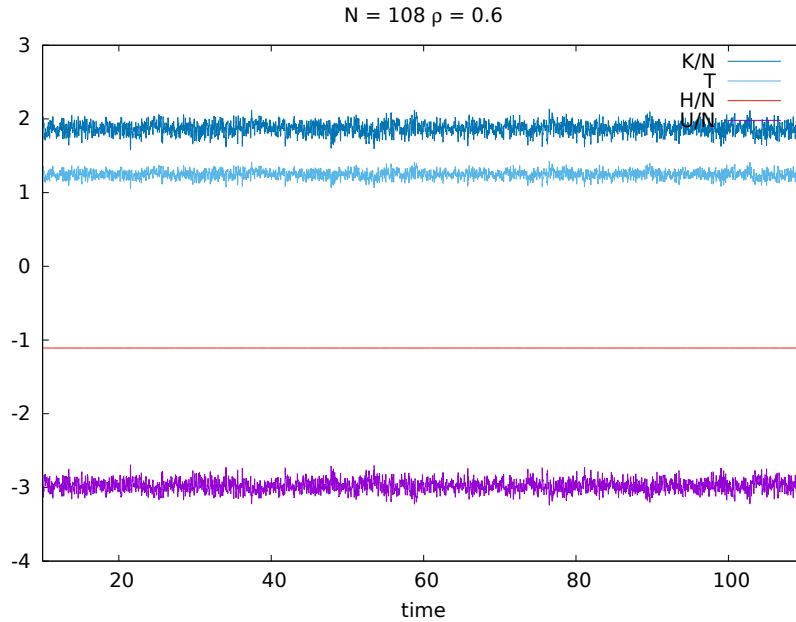


**Figure 7.** We plot, from the top, the kinetic energy  $\frac{K}{N}$ , the instantaneous temperature  $kT$ , the mechanical energy  $\frac{H}{N}$  and the potential energy  $\frac{U}{N}$  for  $N = 108$ ,  $\rho = 0.6$  and initial temperature 1.22.

We note that, because of the approximate conservation of the mechanical energy, the potential energy  $U$  and the kinetic energy  $K$  have opposite fluctuations around their respective expectation values. On the other hand the temperature  $T$  is simply proportional to  $K$  and therefore its fluctuations are proportional to those of the kinetic energy.

$$\langle u \rangle = -2.979756, \quad \sigma_{\text{std}}(u) = 0.075043 \quad (13)$$

$$\langle kT \rangle = 1.247323 \quad \sigma_{\text{std}}(kT) = 0.050026 \quad (14)$$

Finally we measure the pressure:

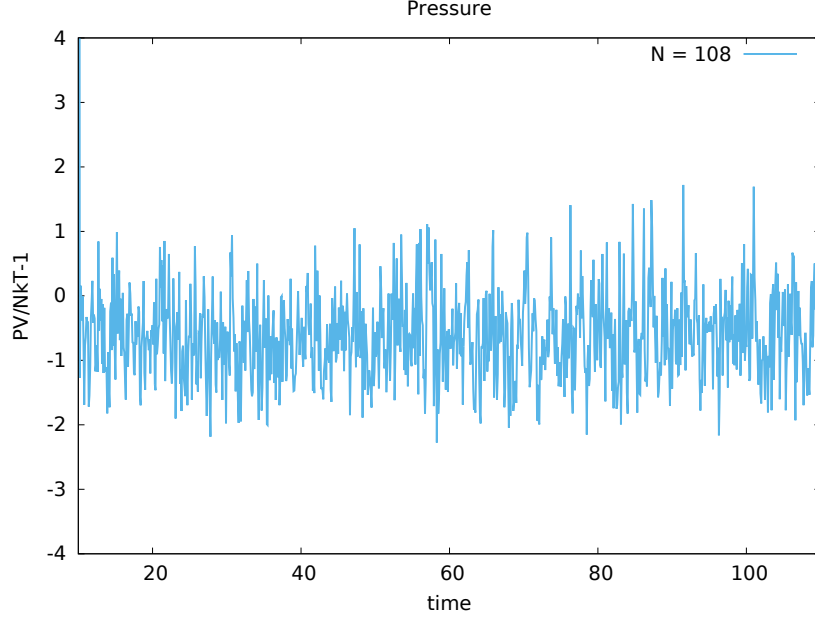


**Figure 8.** Pressure as a function of time for  $N = 108$ ,  $\rho = 0.6$  and initial temperature  $kT = 1.22$ .

$$\frac{PV}{NkT} - 1 = -0.609228 \pm 0.029351 \quad (15)$$

As we can see from (Fig.8), the average pressure value is very close to zero, which is what we expect being the L-J gas a good approximation of an ideal gas.

### 1.5 Mean Squared Displacement

The computation of the MSD is done in the same way as for the case of the hard-core gas in  $3d$ . The system taken in consideration is a L-J gas of  $N = 250$  particles at  $\rho = 0.9$  first at initial temperature  $kT = 0.8$  and then at  $kT = 1.087$ :

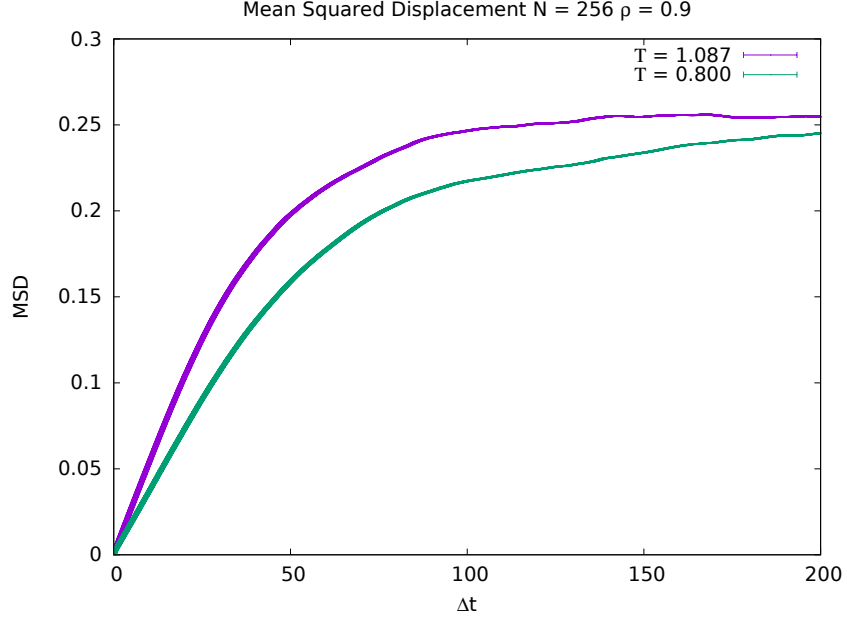


**Figure 9.** MSD for a system with  $N = 250$ ,  $\rho = 0.9$  at temperatures  $kT = 0.8, 1.087$ . The measurements were taken every 100 evolution steps for a total time of  $t = 300$  after a thermalization phase of  $t_{\text{them}} = 10$ . The points with  $\Delta t > 200$  are discarded because of the lower statistics.

Both systems display an initial diffusive behavior given by the typical linear form of the MSD of diffusive processes, but for higher time intervals they converge to the constant value  $1/4$  because of the finite size of the system and of the PBC. The rate of diffusion decreases as the temperature is lowered until the system undergoes a liquid-solid phase transition.

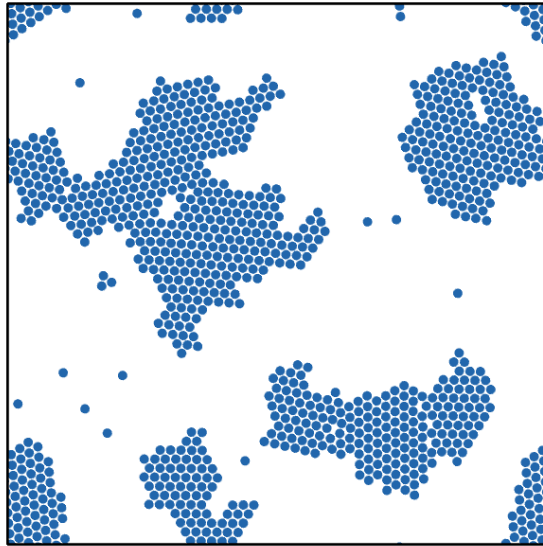


**Figure 10.** Example of solidification of a 2d L-J system of 1000 particles at  $\rho = 0.3$  at  $kT = 0.1$ . Because of the cut-off in the potential, the solid regions do not interact with each other. Each of those regions act as an isolated system.

## 1.6 Thermodynamic Limit

Finally we study the thermodynamic limit extrapolation of the temperature and of the potential energy for systems at fixed density  $\rho = 0.7$  and varying number of particles  $N^1$ . We also fix the mechanical energy to the value  $H/N = -2.98$  and express every quantity in terms of the parameter  $1/N$ .

We assume that for large  $N$ , both the temperature and the potential energy have a linear functional form in the variable  $1/N$ :

$$u = u_\infty + m \cdot \frac{1}{N} \quad (16)$$

$$T = T_\infty + m \cdot \frac{1}{N} \quad (17)$$

so that by fitting the data obtained at different  $N$  we can extrapolate the thermodynamic limit of those observables.

---

<sup>1</sup>. The thermodynamic limit consists, in fact, in sending  $N$  and  $V = L^d$  to infinity while keeping the ratio  $N/V$  constant.

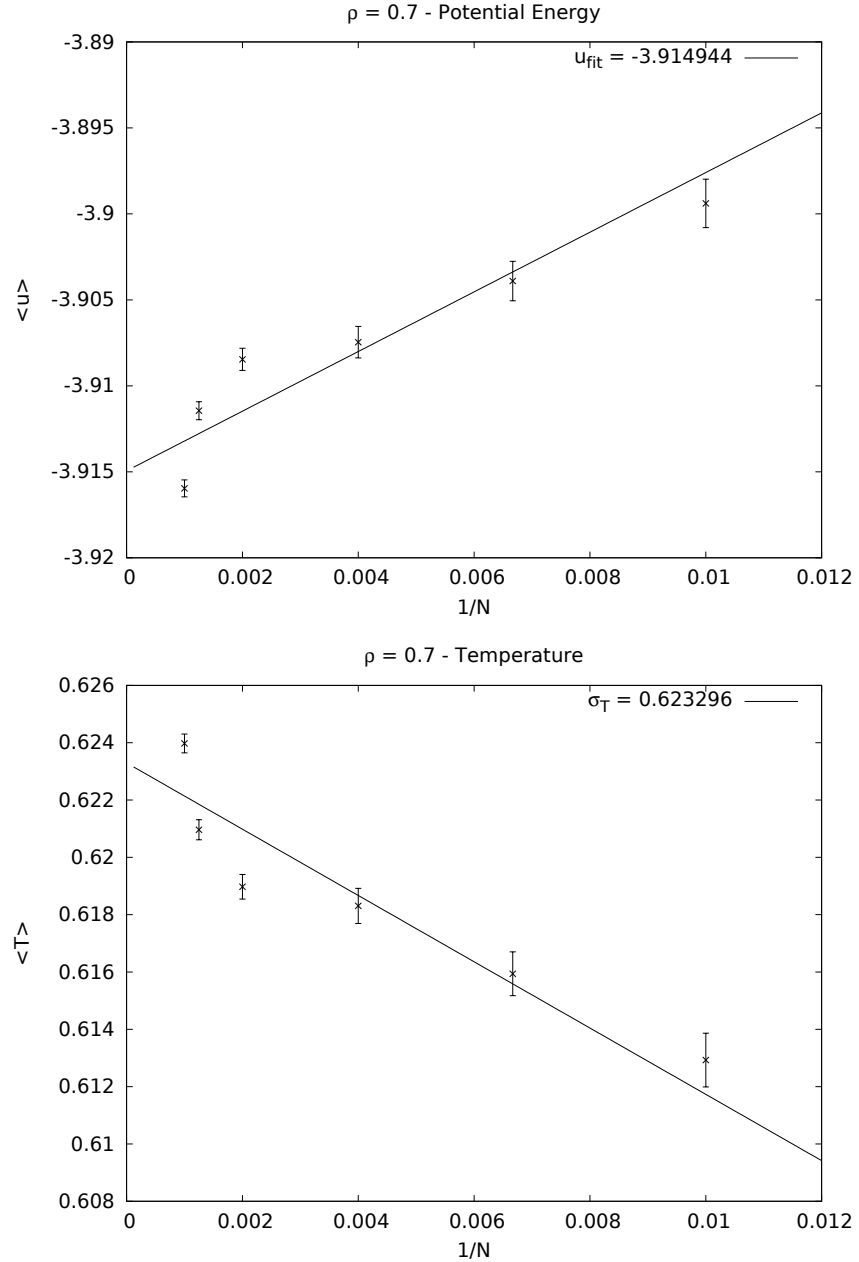


**Figure 11.** Plot of the potential energy (top) and of the temperature (bottom) as functions of the parameter  $1/N$  with  $N = 100, 150, 250, 500, 800, 1000$ . Each point is obtained as the average over a simulation run of time  $t=100$  with samples taken once every 100 steps  $\Delta t=0.001$ . The errorbars are computed as the standard errors on the mean values. The thermalization time is  $t_{\text{therm}}=10$ .

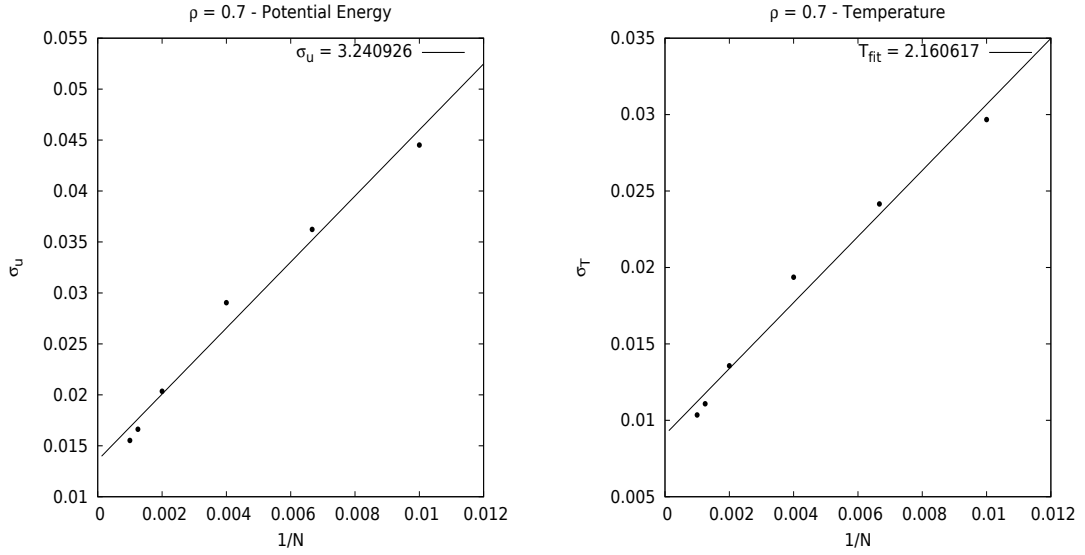


**Figure 12.** Plot of the standard deviation of the potential energy (left) and of the temperature (right) as functions of the parameter  $1/N$  for  $N = 100, 150, 250, 500, 800, 1000$ .

The results are:

$$u_{\text{fit}} = -3.9149 \pm 0.0016 \quad (18)$$

$$T_{\text{fit}} = 0.6233 \pm 0.0011 \quad (19)$$

*Remark:* since the mechanical energy is constant,  $T$  and  $U$  are related by:

$$\frac{H}{N} = \frac{d}{2} T + u = -2.98 \quad (20)$$

and follows that the fluctuations of the two quantities must cancel out:

$$\Rightarrow \frac{3}{2} \sigma_T = \sigma_u \quad (21)$$

$\sigma_u$	3.240926
$\sigma_T$	2.160617

$$\longrightarrow \quad \frac{\sigma_u}{\sigma_T} = 1.5$$

# Laboratory of Computational Physics

BY LUCA CASSIA

Dipartimento di Fisica, Università di Milano-Bicocca  
I-20126 Milano, Italy

Email: [l.cassia@campus.unimib.it](mailto:l.cassia@campus.unimib.it)

## Table of contents

<b>1 Ising Model 2d</b>	1
1.1 Thermalization	1
1.2 Autocorrelation Times	4
1.3 Binning Analysis	6
1.4 Observables	9
1.5 $\beta$ Critical	11
1.6 Probability Distribution Functions	16
1.7 Spatial Correlations	19
1.8 Finite Size Scaling	22

## 1 Ising Model 2d

In this section we study the statistical properties of a 2d Ising Model. We consider a system of  $L \times L$  spins situated on the points of a regular square lattice with periodic boundary conditions (PBC) in both directions. Each spin interacts with its nearest neighbours inside the lattice, with an Hamiltonian:

$$H = - \sum_{\langle i,j \rangle} \sigma_i \sigma_j \quad (1)$$

where the sum is taken only over the set of unordered pairs  $\langle i, j \rangle$  such that  $\sigma_i$  and  $\sigma_j$  are nearest neighbours.

In order to obtain expectation values for physical quantities of the system we should be able to sum over the space of all the spin configurations, or at least to sample configurations from this space with probability:

$$P(\{\sigma\}) \sim e^{-\beta H(\{\sigma\})} \quad (2)$$

which reproduces the integration measure of the functional integral. The obvious choice for numerical simulations is the second one, which we implement through Monte Carlo (MC) algorithms. In particular we focus on the Metropolis-Hastings (MH) and the Swendsen-Wang (SW) algorithms.

### 1.1 Thermalization

Since we do not know where to start in our Markov process, we first initialize the system in a disordered configuration (hot start) and then evolve for a certain Markov time until the system reaches equilibrium. This process is usually called *thermalization*.

After a few run we decided to opt for a cold start approach (i.e., all the spins are initially aligned). The reason for this choice is that, when using MH in 2-dimensional finite-size systems with periodic boundary conditions, the non trivial topology of the lattice allows the existence of stable configurations of the type depicted in (Fig.1), that often arise when the system is rapidly cooled from a disordered configuration. Those configurations would invalidate the mixing process and the sampling of relevant configurations at low temperatures. Therefore, by using a cold start, we exclude this possibility.

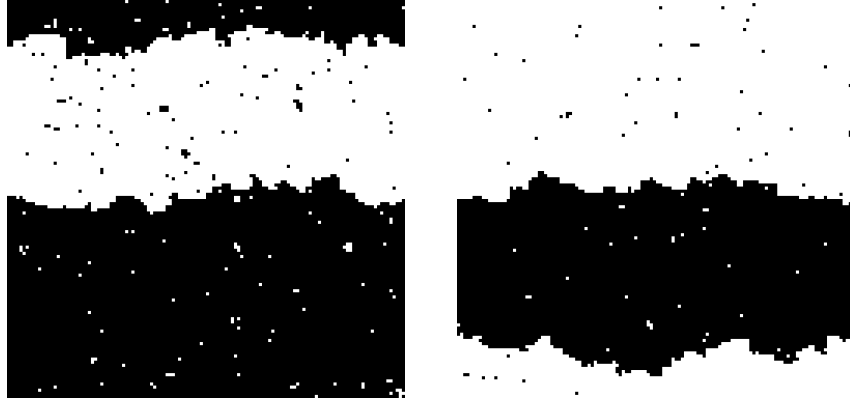


**Figure 1.** Illustration of two topologically non-trivial configurations obtained with the MH algorithm on a lattice  $128 \times 128$ .

We expect the MH algorithm to be slower to thermalize because of the local update it employs as opposed to the cluster update of the SW algorithm.

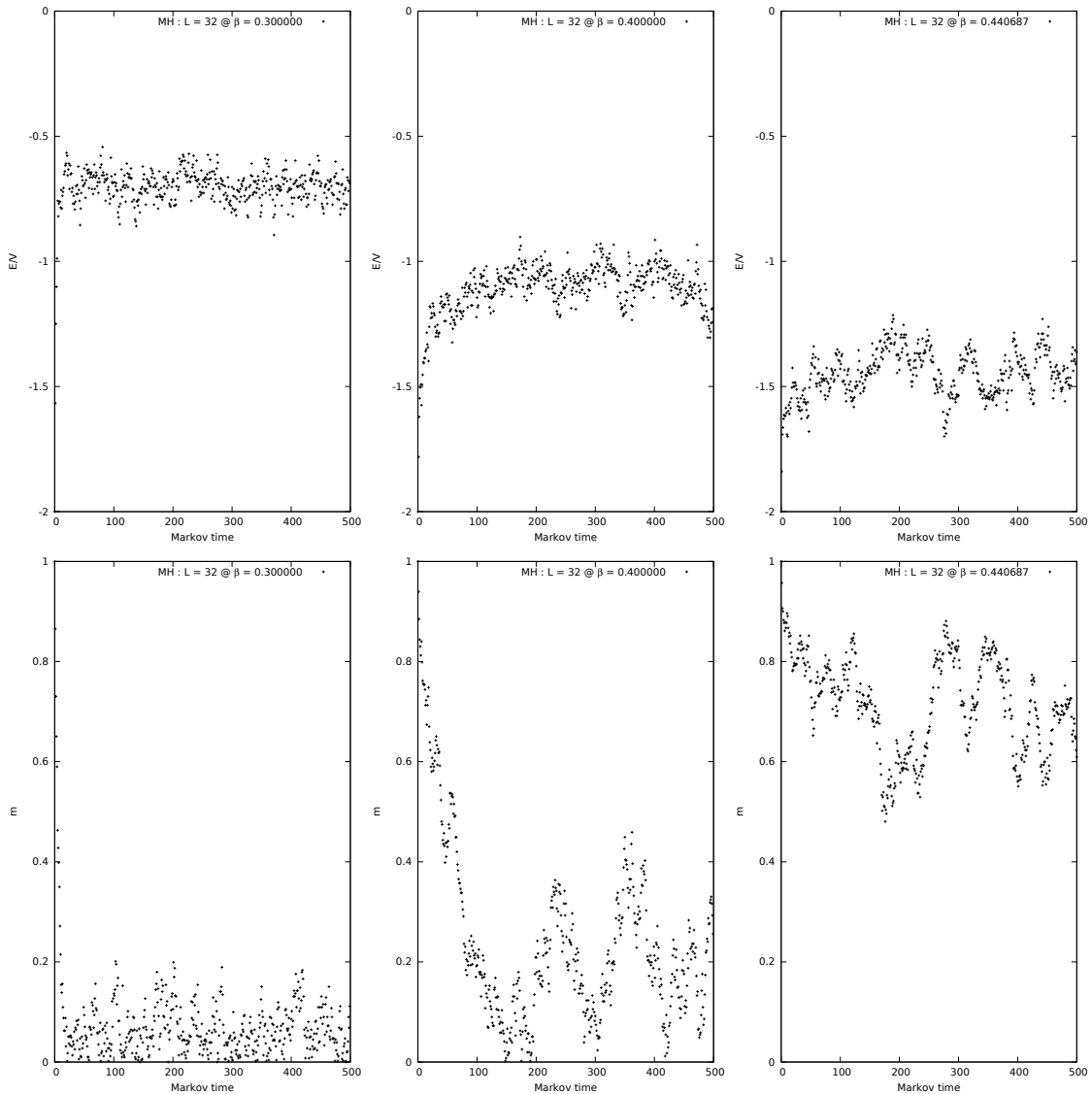


**Figure 2.** Plot of the energy density and magnetization for the MH markov process at different values of  $\beta$ .

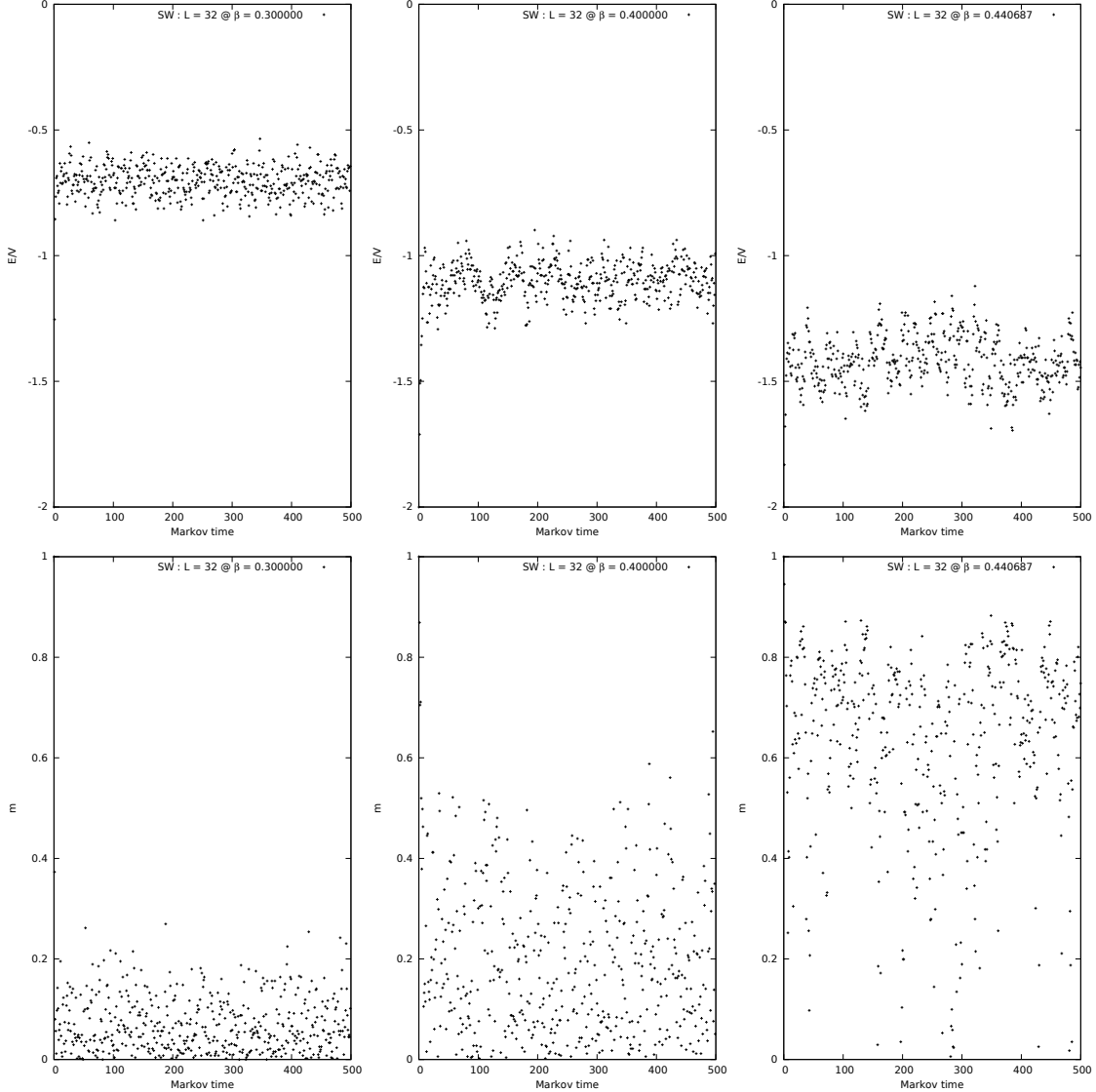


**Figure 3.** Plot of the energy density and magnetization for the SW markov process at different values of  $\beta$ .

The MH algorithm reaches thermalization very rapidly for inverse temperatures  $\beta$  far from the critical value  $\beta_c$ , while for values of  $\beta$  near the phase transition it becomes much slower (Fig.2).

This effect is called *critical slowing down* and it tells us that, when using local update algorithms, successive steps in the Markov chain are strongly correlated and therefore only approximately every  $L^2$  sweeps through the lattice, a statistically independent measurement can be taken. Close to a critical point, in fact, the autocorrelation time (in the infinite-volume limit) typically scales as:

$$\tau_{\mathcal{O}, \text{exp}} \propto \xi^z \quad (3)$$

where  $z \geq 0$  is the so-called dynamical critical exponent. The spatial correlation length  $\xi$  would diverge at the critical point, but in a finite system it is limited by the size  $L$  of the system and the scaling law (3) becomes:

$$\tau_{\mathcal{O}, \text{exp}} \propto L^z \quad (4)$$

where  $z \approx 2$  for local dynamics (MH) and  $z \approx 0$  for SW.

We also remark that for smaller values of  $\beta$ , the energy of the system can have larger fluctuations around its average and therefore thermal equilibrium is reached faster.

On the other hand the SW algorithm mixes very fast even at the phase transition (Fig.3) being a multicluster update algorithm (Fig.3).

For the rest of the simulations we considered the system to be at equilibrium after a thermalization time  $t \approx 1000$  both for MH and for SW.

## 1.2 Autocorrelation Times

We now study the correlations present between consecutive configurations sampled by the two algorithms in order to obtain the characteristic time after which we can consider two configurations to be statistically independent. This is called *integrated autocorrelation time* and is computed in the following way:

$$\tau_{\mathcal{O},\text{int}} = \frac{1}{2} + \sum_{k=1}^{k_{\max}} R(k) \quad (5)$$

where  $\mathcal{O}$  is the physical observable for which we compute autocorrelation and  $R(k)$  is defined as:

$$R(k) = \frac{1}{(n-k)\sigma^2} \sum_{t=1}^{n-k} (\mathcal{O}_t - \mu)(\mathcal{O}_{t+k} - \mu) \quad (6)$$

here  $n$  is the total number of samples of  $\mathcal{O}$  and  $\mu, \sigma^2$  are the mean and variance of the process. For large time separations  $k$ ,  $R(k)$  decays exponentially:

$$R(k) \xrightarrow{k \rightarrow \infty} r e^{-k/\tau_{\mathcal{O},\text{exp}}} \quad (7)$$

which defines the exponential autocorrelation time  $\tau_{\mathcal{O},\text{exp}}$ .

We immediately see from (Fig.4) that the MC process is strongly correlated in time particularly near the phase transition:

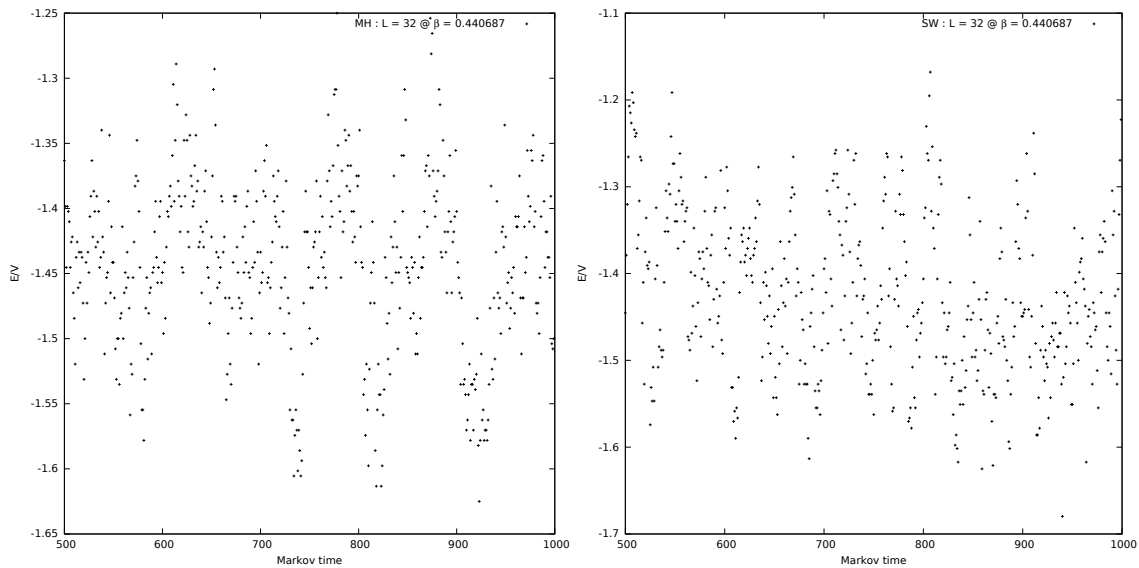


**Figure 4.** Comparison of the energy for the two algorithms at  $\beta = \beta_c$  and  $L = 32$ . (Left) MH (Right) SW.

We now compute the autocorrelation time  $\tau_{\text{int}}$  for the observable  $e = E / V$  using formula (5):

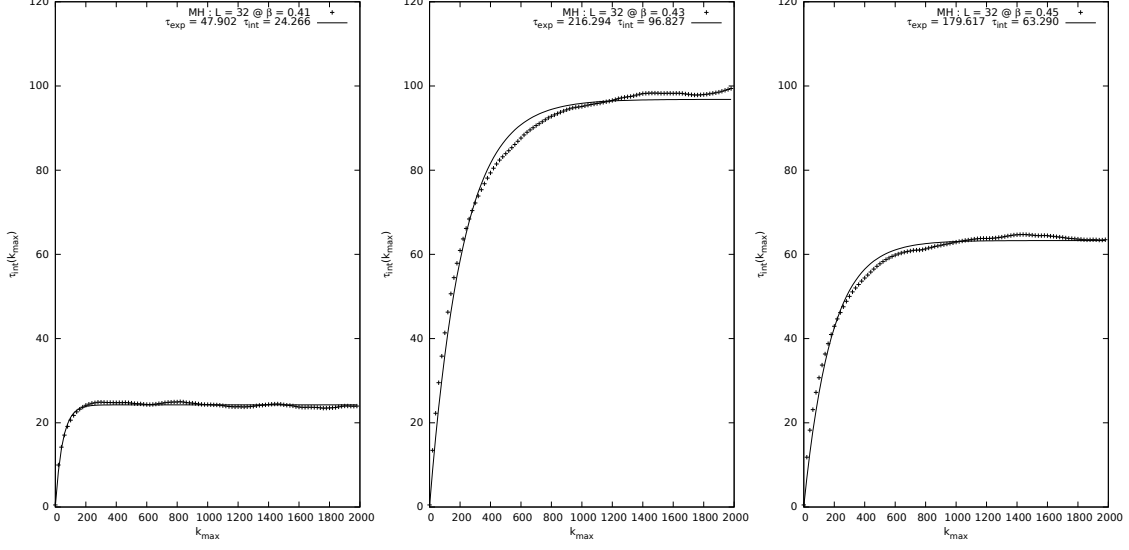


**Figure 5.** Plot of the integrated autocorrelation time near the phase transition for the MH algorithm. The raw data was obtained from a simulation of  $10^6$  measurements on a lattice  $32 \times 32$ . The fit in the center is not very accurate because near  $\beta_c$  the autocorrelation time becomes very large and the interval  $[0, 2000]$  becomes too small for a reliable estimate of  $\tau_{\text{int}}$ .

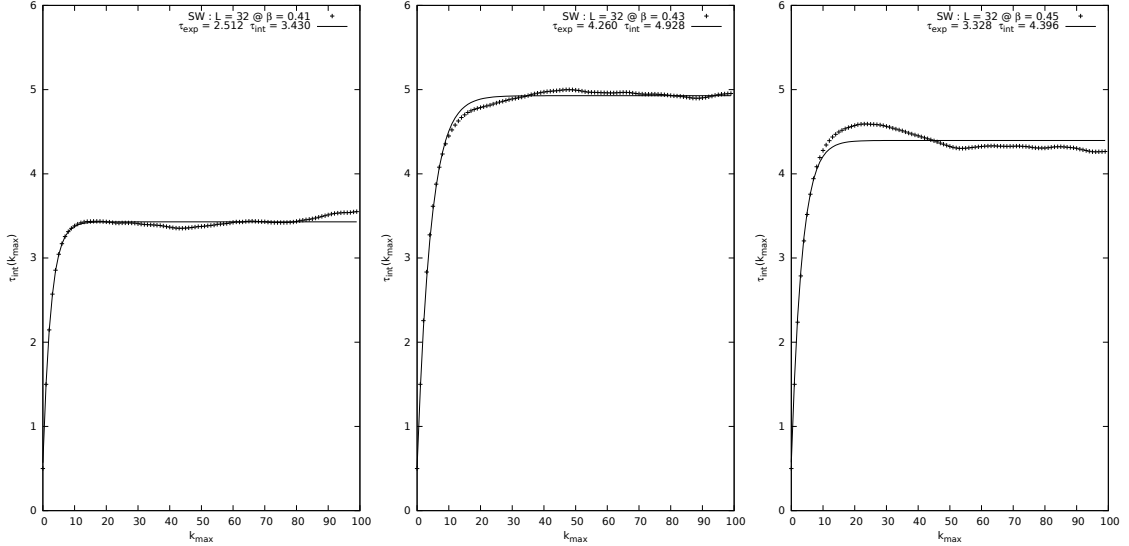


**Figure 6.** Plot of the integrated autocorrelation time near the phase transition for the SW algorithm. The raw data was obtained from a simulation of  $10^5$  measurements on a lattice  $32 \times 32$ .

The data is fitted using the function:

$$\tau_{\text{int}}(k_{\max}) = \tau_{\text{int}} \left[ 1 - \frac{2 \tau_{\text{exp}}}{2 \tau_{\text{exp}} + 1} e^{-k_{\max}/\tau_{\text{exp}}} \right] \quad (8)$$

which is the exact solution for a bivariate gaussian process.

As we can see, near the phase transition the autocorrelation time for the MH process becomes very large compared to the autocorrelation time of the SW process (Fig.7). In fact due to the

critical slowing down of the MH algorithm, we have  $\tau_{\text{int}}^{\text{MH}} \sim 100$  compared to an autocorrelation time  $\tau_{\text{int}}^{\text{SW}} \sim 5$  for SW.

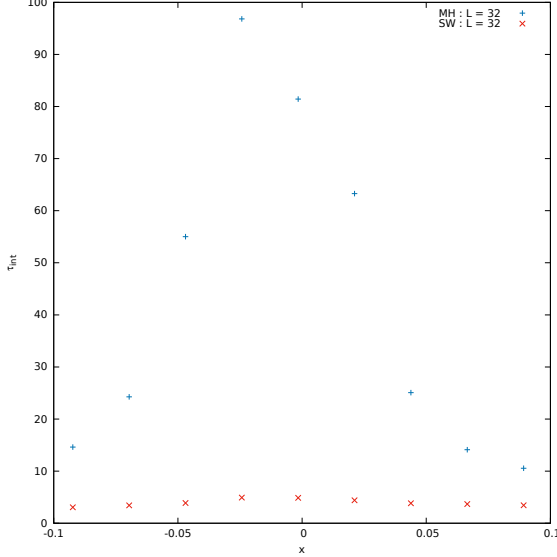


**Figure 7.** Plot of the integrated autocorrelation time as a function of  $x = \frac{\beta - \beta_c}{\beta_c}$  for  $L = 32$ .

We remark that the peak is slightly off centered because of the finite size of the lattice (pseudocritical point  $\beta_c(V) < \beta_c(\infty)$ ).

### 1.3 Binning Analysis

In order to have a statistical ensemble of uncorrelated data we need to address the issue of autocorrelation in the Markov process. An easy and efficient way to do so is to split the data in non-overlapping blocks of the same size and then average over each block to obtain (almost)uncorrelated data for the observable  $\mathcal{O}$  of interest. The blocks are also called *bins* and this method is called binning.

Consider an ensemble of  $N = N_B \cdot k$  samples divided in  $N_B$  blocks of size  $k$ . For each block  $n$  we take the average of the observables  $\mathcal{O}_i$  it contains and then obtain a block-observable  $\mathcal{O}_{B,n}$ :

$$\mathcal{O}_{B,n} = \frac{1}{k} \sum_{i=0}^{k-1} \mathcal{O}_{nk+i} \quad n = 0, \dots, N_B - 1 \quad (9)$$

From a simple calculation we obtain that the error estimate on the mean value is:

$$\epsilon_{\mathcal{O}}^2 \equiv \sigma_{\mathcal{O}}^2 = \frac{\sigma_B^2}{N_B} = 2 \tau_{\mathcal{O},\text{int}} \frac{\sigma_{\mathcal{O}_i}^2}{N} \quad (10)$$

hence:

$$2 \tau_{\mathcal{O},\text{int}} = k \sigma_B^2 / \sigma_{\mathcal{O}_i}^2 \quad (11)$$

We study the dependence of the variance  $\sigma_B^2$  on the block size  $k$ . The observable we consider is the energy density  $e$ .

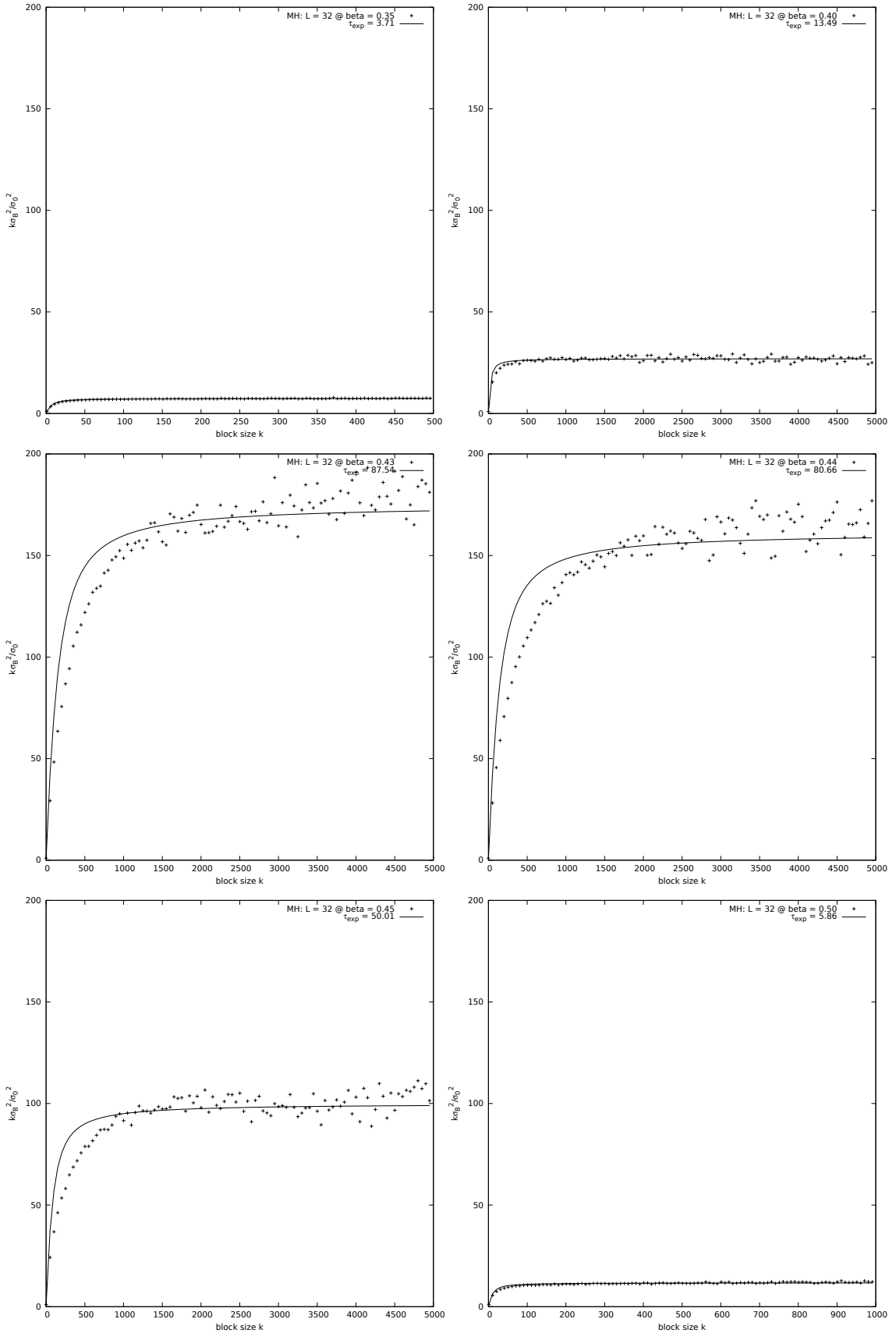


**Figure 8.** Binning analysis for the MH algorithm at various values of  $\beta$  ( $L = 32$ ).

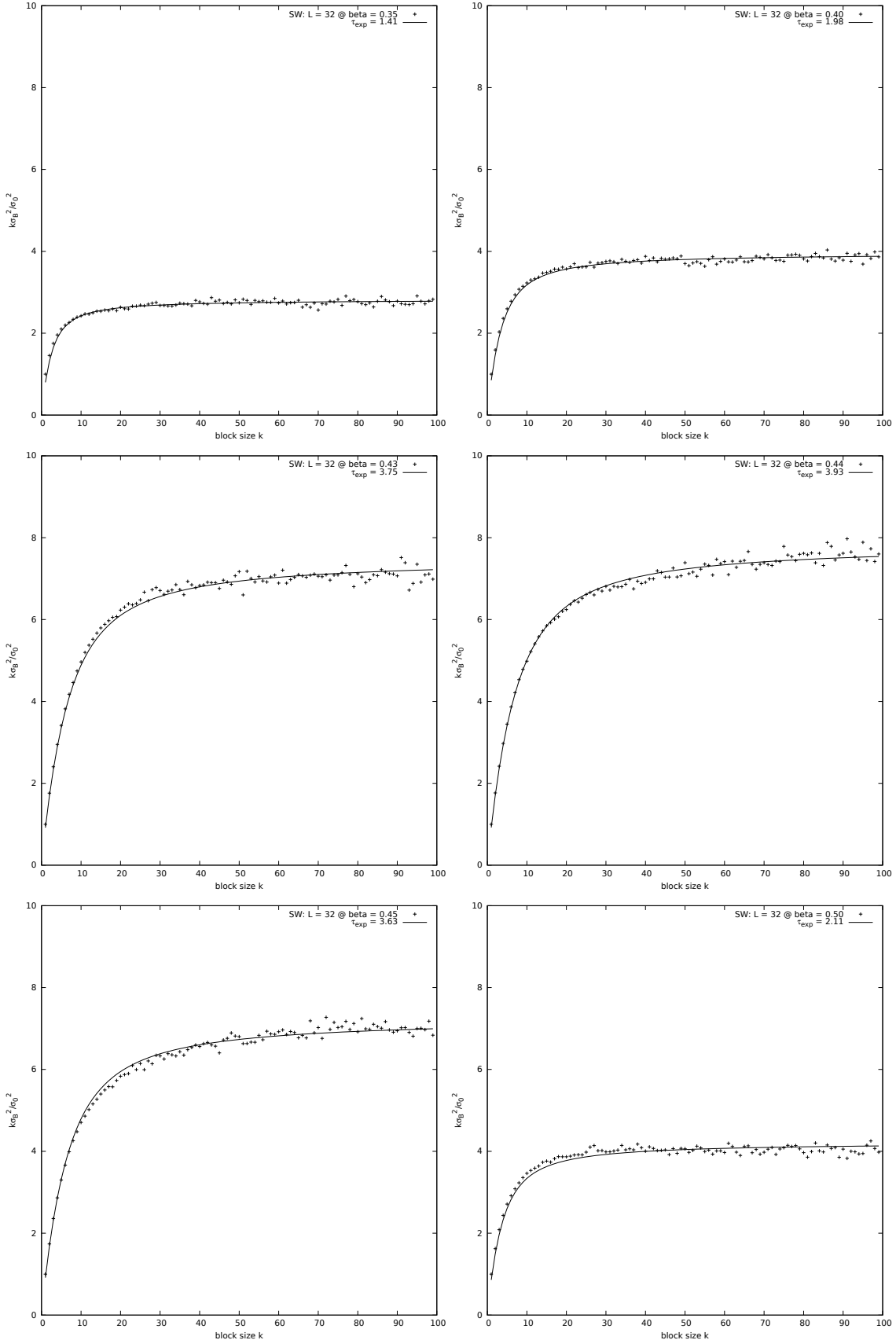


**Figure 9.** Binning analysis for the SW algorithm at various values of  $\beta$  ( $L = 32$ ).

Where we fitted the data using the formula:

$$k \sigma_B^2 \approx 2 \tau_{\text{exp}} \left( 1 - \frac{\tau_{\text{exp}}}{k} (1 - e^{-k/\tau_{\text{exp}}}) \right) \quad (12)$$

The lowest value of  $k$  for which we can consider the binned data to be uncorrelated is obtained by looking at the point for which the signal for  $k \sigma_B^2 / \sigma_{\mathcal{O}_i}^2$  stabilizes and its first derivative tends to zero. We call this point  $k^*(\beta)$ . Since  $\tau_{\text{exp}}$  has a local maximum at the critical point, we take  $k^*(\beta_c)$  as the block size for the following simulations.

With the block sizes set to:

$$\begin{aligned} k_{\text{MH}}^* &= 1000 \\ k_{\text{SW}}^* &= 50 \end{aligned}$$

we should now able to sample data without having to worry about autocorrelation in the signal.

## 1.4 Observables

The main observables of interest for this system are the energy density  $e$  and the magnetization  $m$ :

$$e = E/V, \quad E = \langle \mathcal{H} \rangle, \quad V = L^d \quad (13)$$

$$m = M/V, \quad M = \langle \mathcal{M} \rangle, \quad \mathcal{M} = \left| \sum_i \sigma_i \right| \quad (14)$$

Thanks to the analytical solution of the 2d Ising model, first obtained by Onsager, we are able to compare the estimators computed by numerical simulations with their exact values obtained analytically.

The samples and the errors are collected employing the binning procedure of the previous section. For each inverse temperature we compute the estimate of the generic observable  $\mathcal{O}$  from

$10^5$  measurements for MH and  $10^4$  for SW.

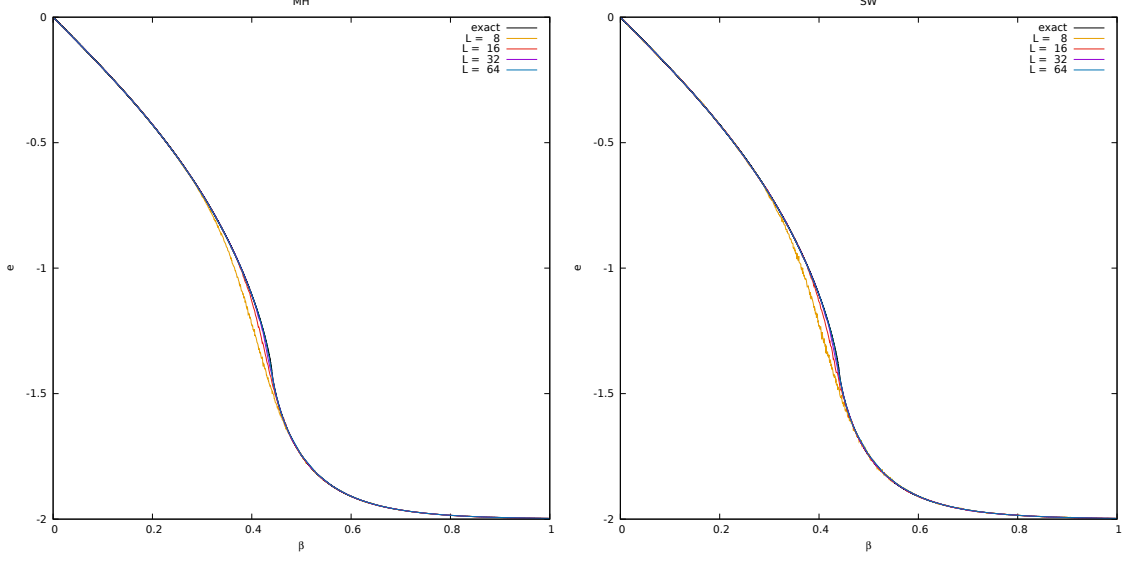


**Figure 10.** Energy density as a function of  $\beta$ . MH on the left and SW on the right.

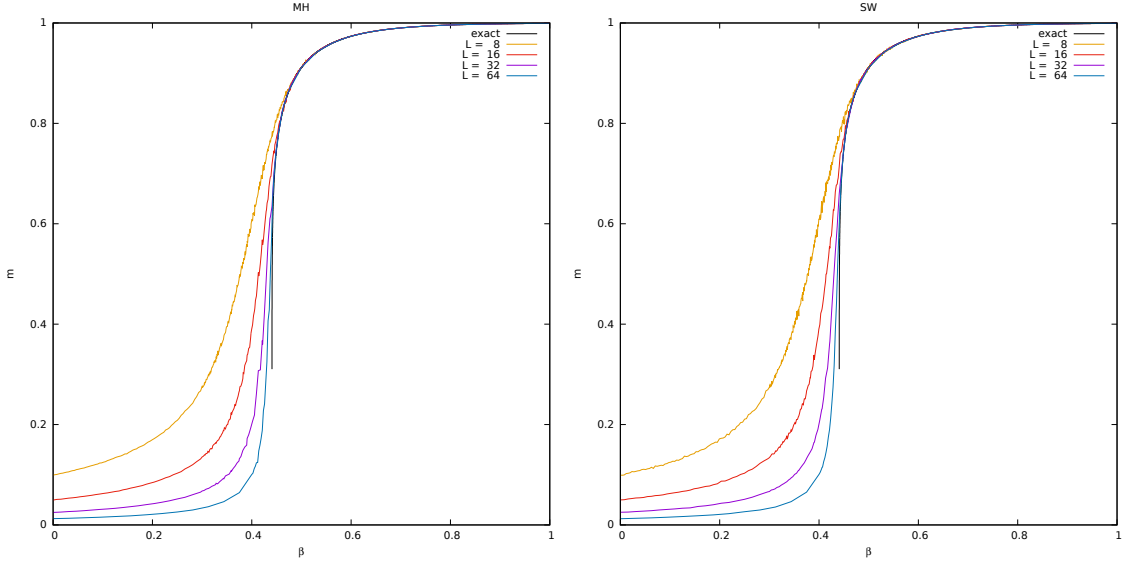


**Figure 11.** Magnetization as a function of  $\beta$ . MH on the left and SW on the right.

We find that the simulation data are remarkably close to the exact solution both for the energy density and for the magnetization especially for large sizes of the lattice. The only departure from Onsager's solution is in the paramagnetic phase of the magnetization plot: there we observe that the exact solution goes abruptly to zero before the critical point, while the numerical data seems to interpolate a smooth function. This is imputable to the finite size of the lattice used for the simulation. It is indeed a well known fact that discontinuities and divergences only appear in the thermodynamic limit of infinite size, which is precisely the premise of Onsager's solution. In fact, the numerical solution approaches more and more the exact one as the size of the lattice increases.

We also plot the heat capacity:

$$C = \frac{\beta^2}{V} \langle (\mathcal{H} - \langle \mathcal{H} \rangle)^2 \rangle \quad (15)$$

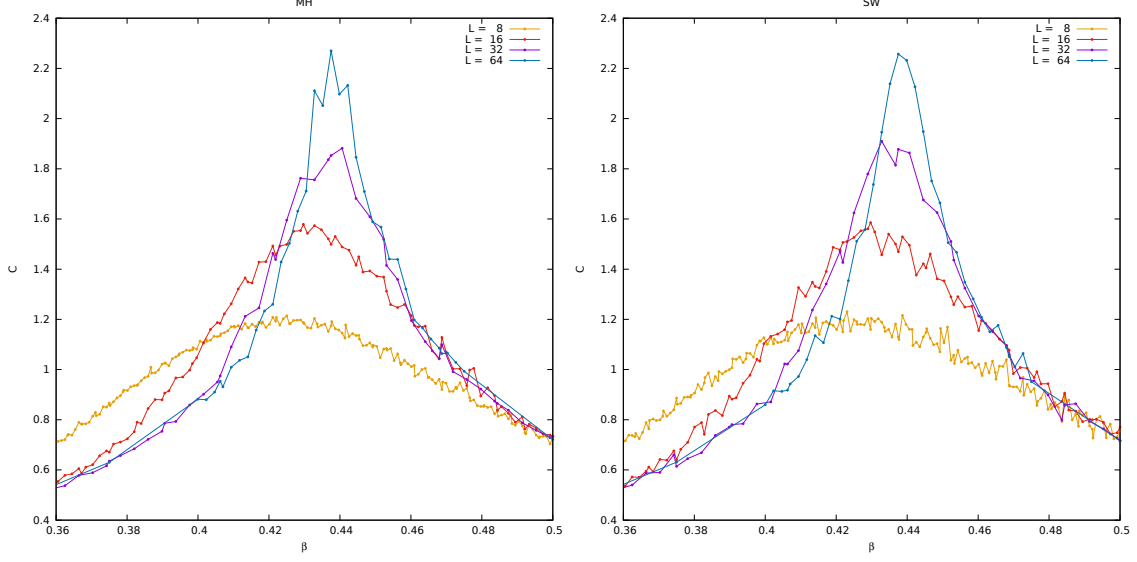


**Figure 12.** Heat capacity as a function of  $\beta$ . MH on the left and SW on the right.

and the magnetic susceptibility:

$$\chi = \frac{\beta}{V} \langle (\mathcal{M} - \langle \mathcal{M} \rangle)^2 \rangle \quad (16)$$

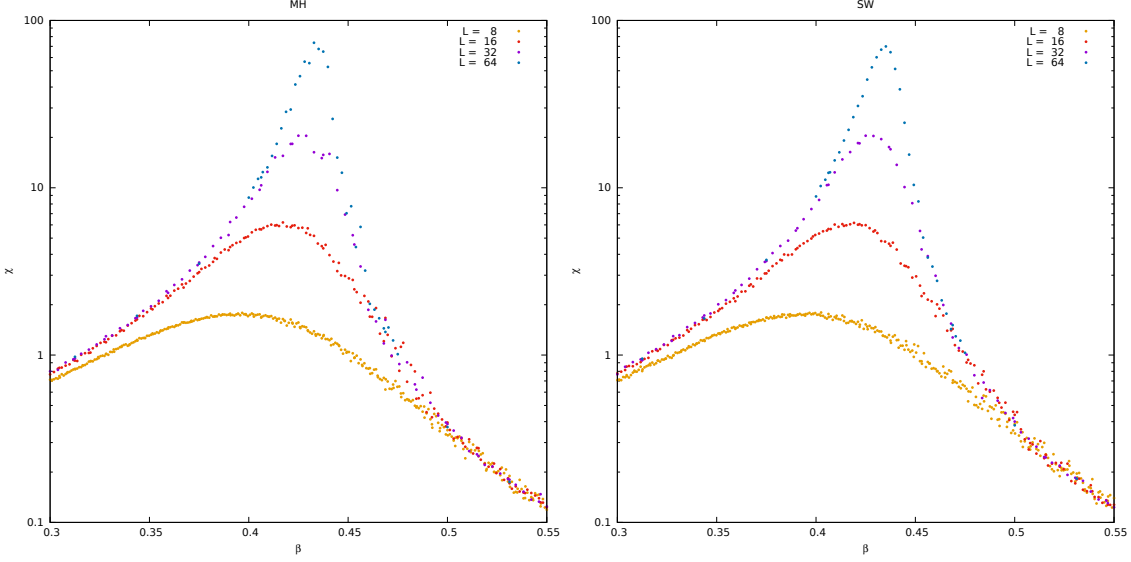


**Figure 13.** Magnetic susceptibility as a function of  $\beta$ . MH on the left and SW on the right.

As we immediately see from (Fig.12) and (Fig.13) the peak of the curve is progressively shifted to the infinite-size limit value  $\beta_c$  as we approach larger and larger sizes of the lattice:

$$\lim_{L \rightarrow \infty} \beta_{\max}(L) = \beta_c = \ln(1 + \sqrt{2})/2 \quad (17)$$

### 1.5 $\beta$ Critical

From a power law fit of the points near the peak of each dataset we obtain estimates for the pseudocritical  $\beta$ -values at finite sizes  $L = 8, 16, 32, 64$ .

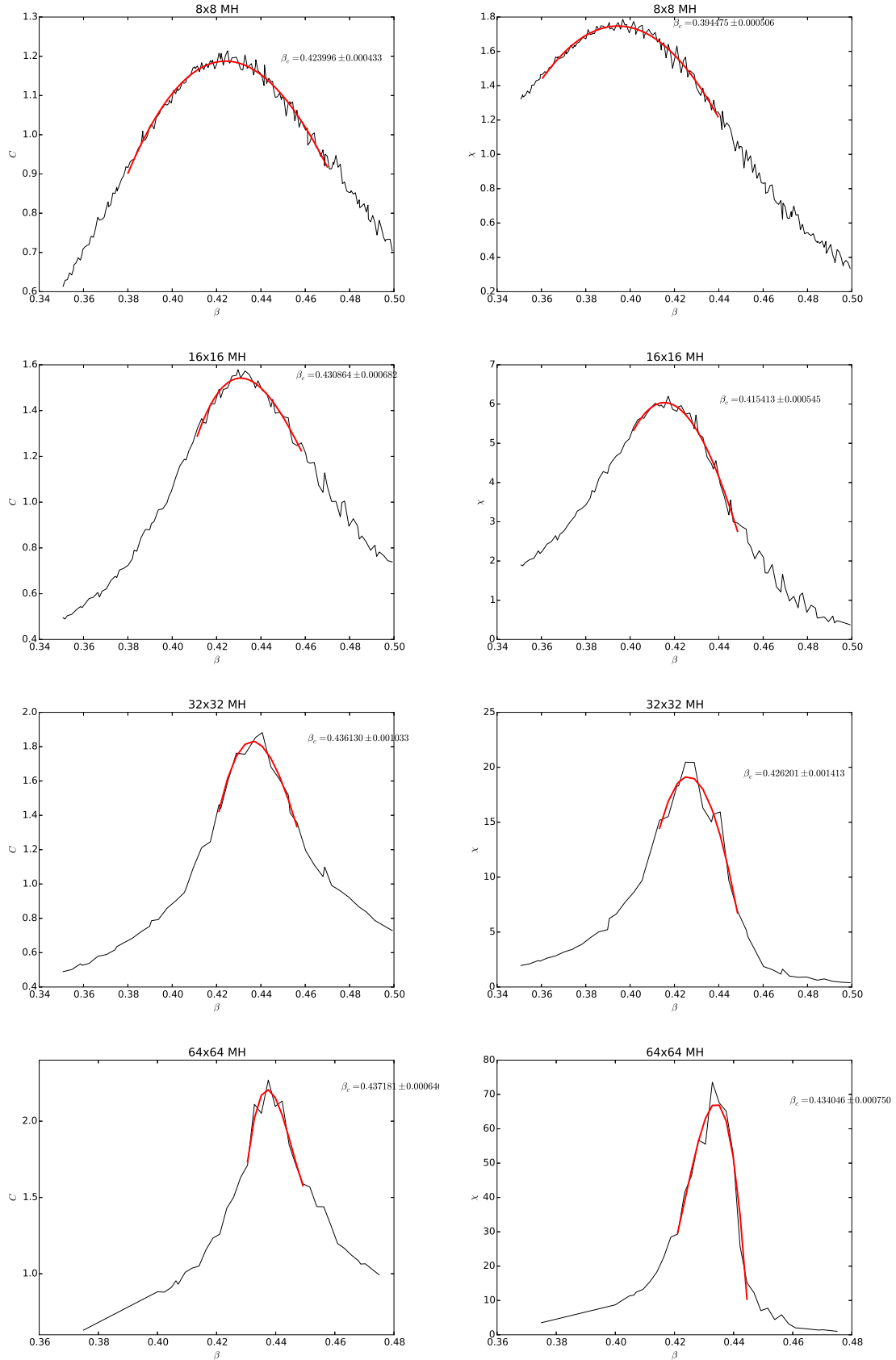


**Figure 14.** Fit of the heat capacity and susceptibility peaks (MH).

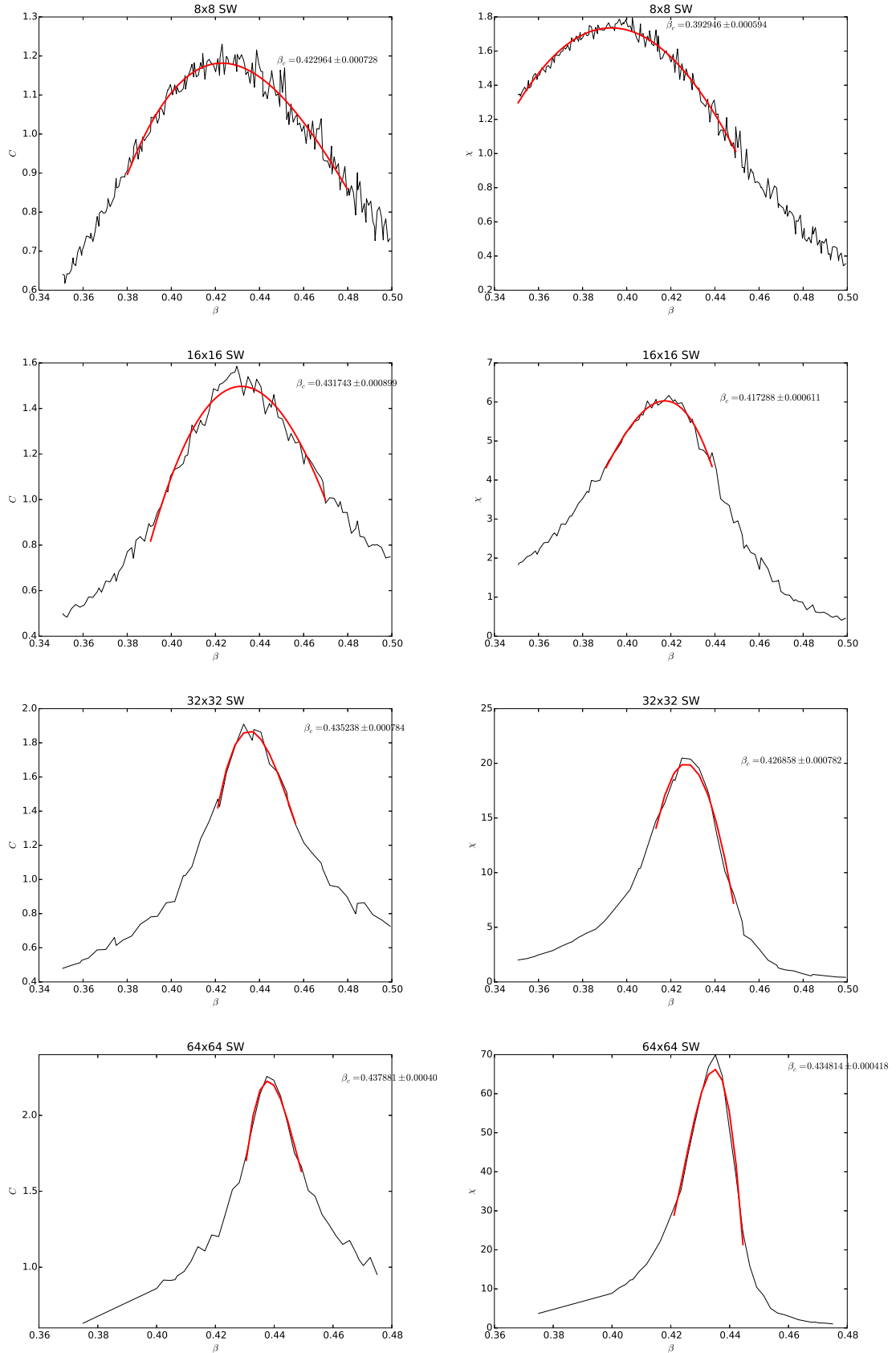


**Figure 15.** Fit of the heat capacity and susceptibility peaks (SW).

$L$	$\beta_{\max}(C)$	$\beta_{\max}(\chi)$
8	$0.42400 \pm 0.00043$	$0.39448 \pm 0.00051$
16	$0.43086 \pm 0.00086$	$0.41541 \pm 0.00055$
32	$0.43613 \pm 0.00103$	$0.42620 \pm 0.00141$
64	$0.43718 \pm 0.00065$	$0.43405 \pm 0.00075$

**Table 1.** Pseudocritical  $\beta$ -values obtained by polynomial fit of the peaks of  $C$  and  $\chi$  (MH).

The polynomial function we used for the fit is:

$$f(\beta) = A + B(\beta - \beta_{\max})^2 + C(\beta - \beta_{\max})^3 \quad (18)$$

where we omitted the term of order one since it should be zero near the maximum of the function.

$L$	$\beta_{\max}(C)$	$\beta_{\max}(\chi)$
8	$0.42296 \pm 0.00073$	$0.39295 \pm 0.00059$
16	$0.43174 \pm 0.00090$	$0.41729 \pm 0.00061$
32	$0.43524 \pm 0.00078$	$0.42686 \pm 0.00078$
64	$0.43788 \pm 0.00040$	$0.43481 \pm 0.00042$

**Table 2.** Pseudocritical  $\beta$ -values obtained by polynomial fit of the peaks of  $C$  and  $\chi$  (SW).

*Remark:* the estimates of the heat capacity and magnetic susceptibility of the MH algorithm are very accurate for small values of  $L$  where we employed a large dataset of  $10^5$  measurements and the autocorrelation time is relatively small. For large values of  $L$  the autocorrelation time grows very large compared to the size of the dataset and the estimates become less accurate.

The situation for the SW algorithm is different since the autocorrelation time in this case is always under control. However the smaller size of the dataset results in less accurate estimates especially at small lattice sizes where the MH algorithm is most efficient.

We can now obtain an estimate of  $\beta_c$  from a power law fit to the location of the maxima  $\beta_{\max}$ :

$$\beta_{\max} = \beta_c - c L^{-\nu} \quad (19)$$

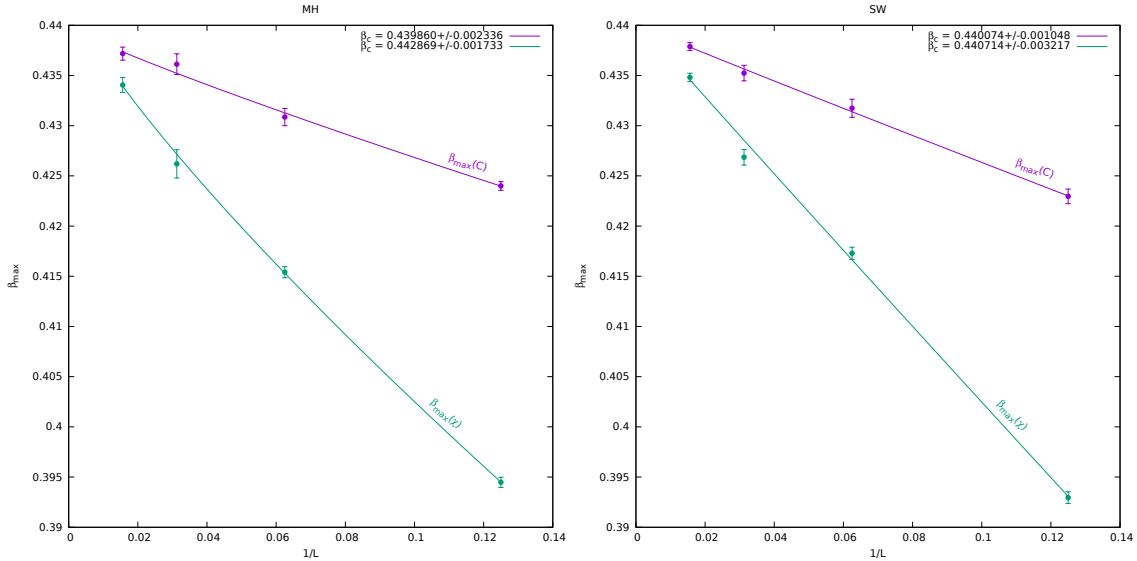


**Figure 16.** Pseudocritical inverse temperature fit. MH on the left, SW on the right. The purple lines are relative to the heat capacity  $C$  while the green ones to the magnetic susceptibility  $\chi$ .

The result of the fit are:

	$\beta_c(C)$	$\beta_c(\chi)$
MH	$0.43986 \pm 0.000234$	$0.44287 \pm 0.000173$
SW	$0.44007 \pm 0.000105$	$0.44071 \pm 0.000322$

These results are very close to the exact solution but still they could be greatly improved by taking more points especially at larger values of  $L$  for which  $C$  and  $\chi$  are more peaked.

## 1.6 Probability Distribution Functions

We study the probability distribution of the magnetization for a lattice of size  $L = 8$ . The energy and magnetization levels of a discrete system are quantized. In particular, for an Ising model on a square lattice of size  $L^2$  with PBC, there are exactly  $L^2 + 1$  magnetization levels equidistributed in the interval  $[-1, +1]$ .

With this consideration one can construct the probability distribution function of the magnetization just by counting the number of samples in each level (for  $L$  not too large). In (Fig.17) and (Fig.18) we show the PDFs of  $m$  for both of the algorithms and for various values of  $\beta$ :

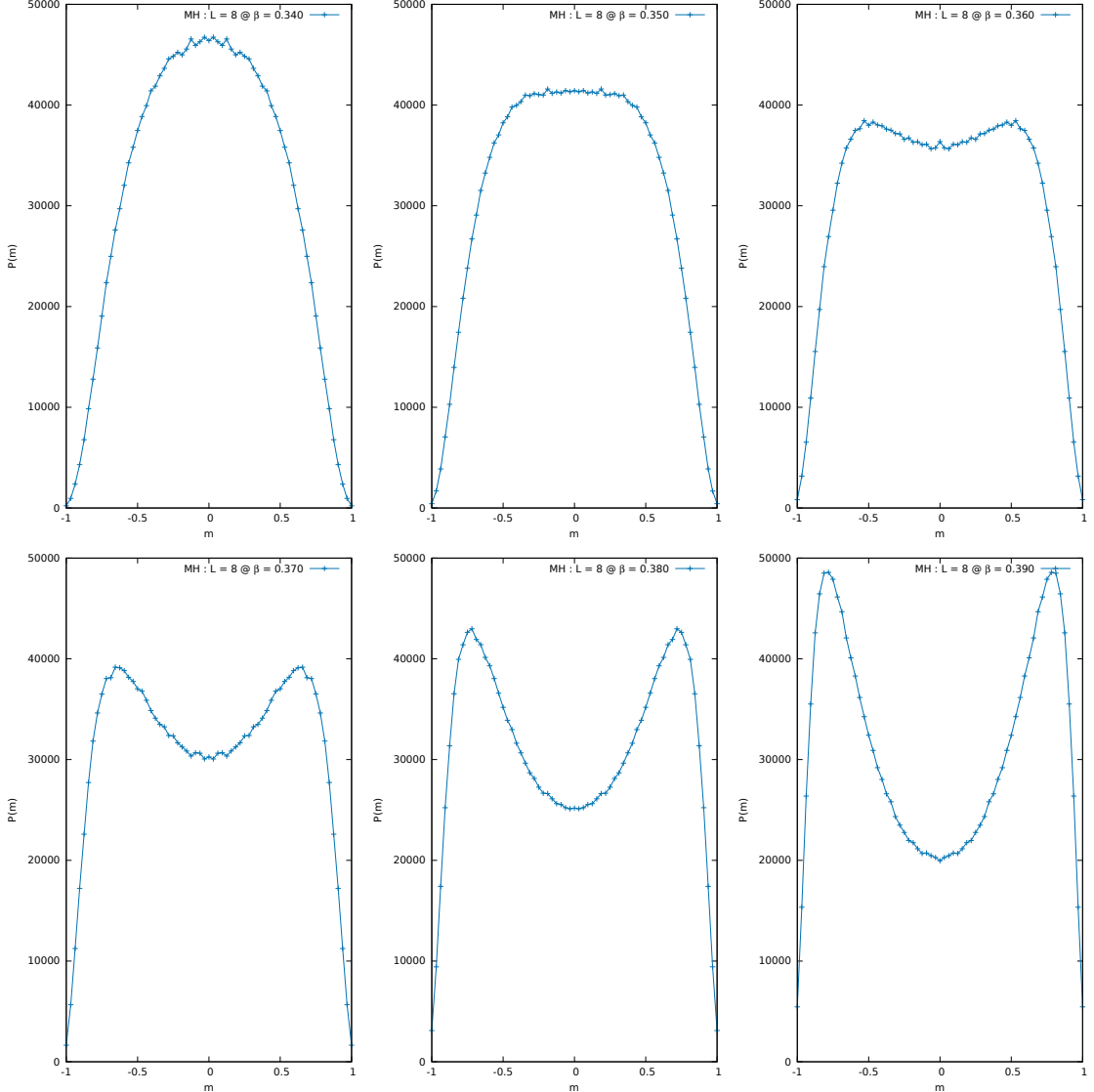


**Figure 17.** Probability distribution functions of  $m$  obtained from  $10^6$  sweeps of MH on a lattice  $8 \times 8$ .

By looking at the PDFs of  $m$  we can witness the formation of a 2-fold degeneracy of the ground state of the system for  $\beta > \beta_c$ . Moreover, if we get close to the phase transition, we see that the distribution  $P(m, \beta)$  becomes almost flat at  $m=0$  before “splitting” into the sum of two PDFs for the two degenerate vacua. This implies that near  $\beta_c$  the distribution does not have a well defined second cumulant, which is precisely the magnetic susceptibility.

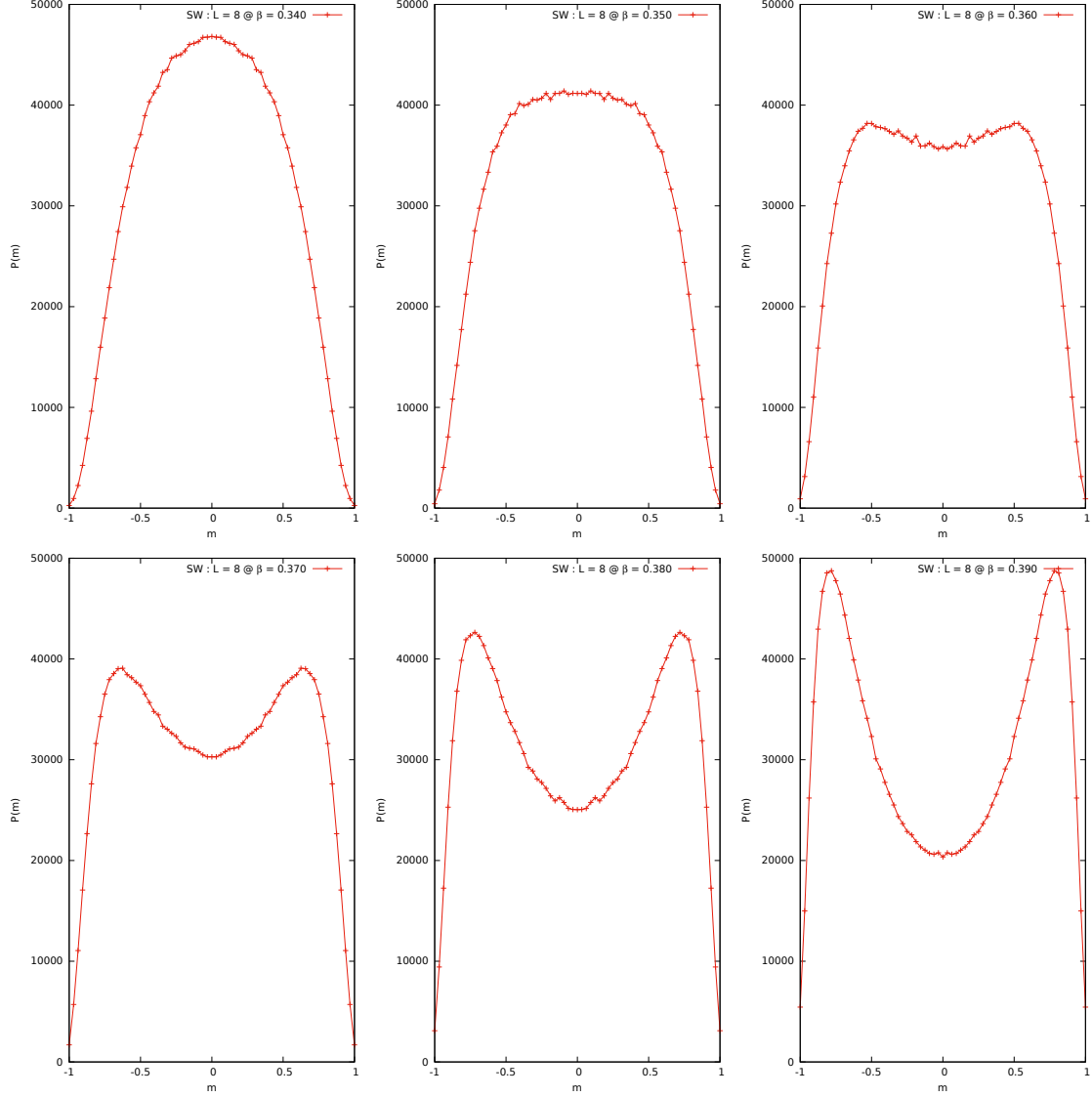


**Figure 18.** Probability distribution functions of  $m$  obtained from  $10^6$  sweeps of SW on a lattice  $8 \times 8$ .

Since we used a cold start initialization, all our simulations of MH at temperatures lower than  $T_c$  spontaneously broke the  $\mathbb{Z}_2$  symmetry of the ground state to some value  $m_0 > 0$ . Having used a hot start initialization instead, we would have ended up with  $m_0 = \pm|m_0|$  with probability  $\frac{1}{2}$  each. For the SW algorithm this is not an issue since it can easily tunnel between ground states by flipping large numbers of spins in a single sweep. In both cases, though, we measured the unsigned magnetization thus obtaining only histograms for the range  $[0, 1]$ . In (Fig.17) and (Fig.18) we computed the histograms for the negative range by assuming the  $\mathbb{Z}_2$  symmetry:

$$P(-m) = P(m) \quad (20)$$

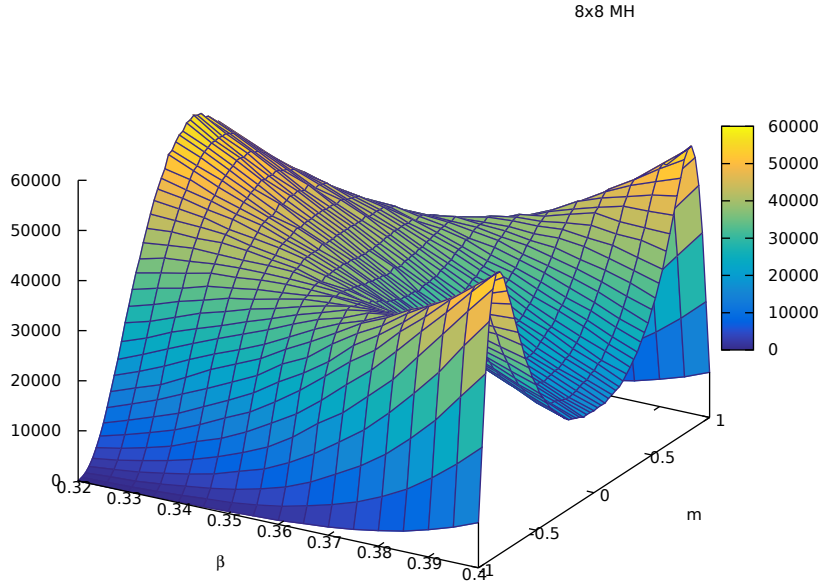


**Figure 19.** 3d plot of  $P(m, \beta)$  as computed from  $10^6$  measurements of  $m$  obtained on a  $8 \times 8$  lattice with the MH algorithm.

## 1.7 Spatial Correlations

The two-point correlation function is defined as:

$$G(\vec{r}_i - \vec{r}_j) = \langle \sigma_i \sigma_j \rangle \sim \exp(-|\vec{r}_i - \vec{r}_j|/\xi) \quad \text{for large } |\vec{r}_i - \vec{r}_j| \quad (21)$$

where  $\xi$  is the correlation length of the system:

$$\xi = -\lim_{|\vec{r}| \rightarrow \infty} (|\vec{r}| / \ln G(\vec{r})) \quad (22)$$

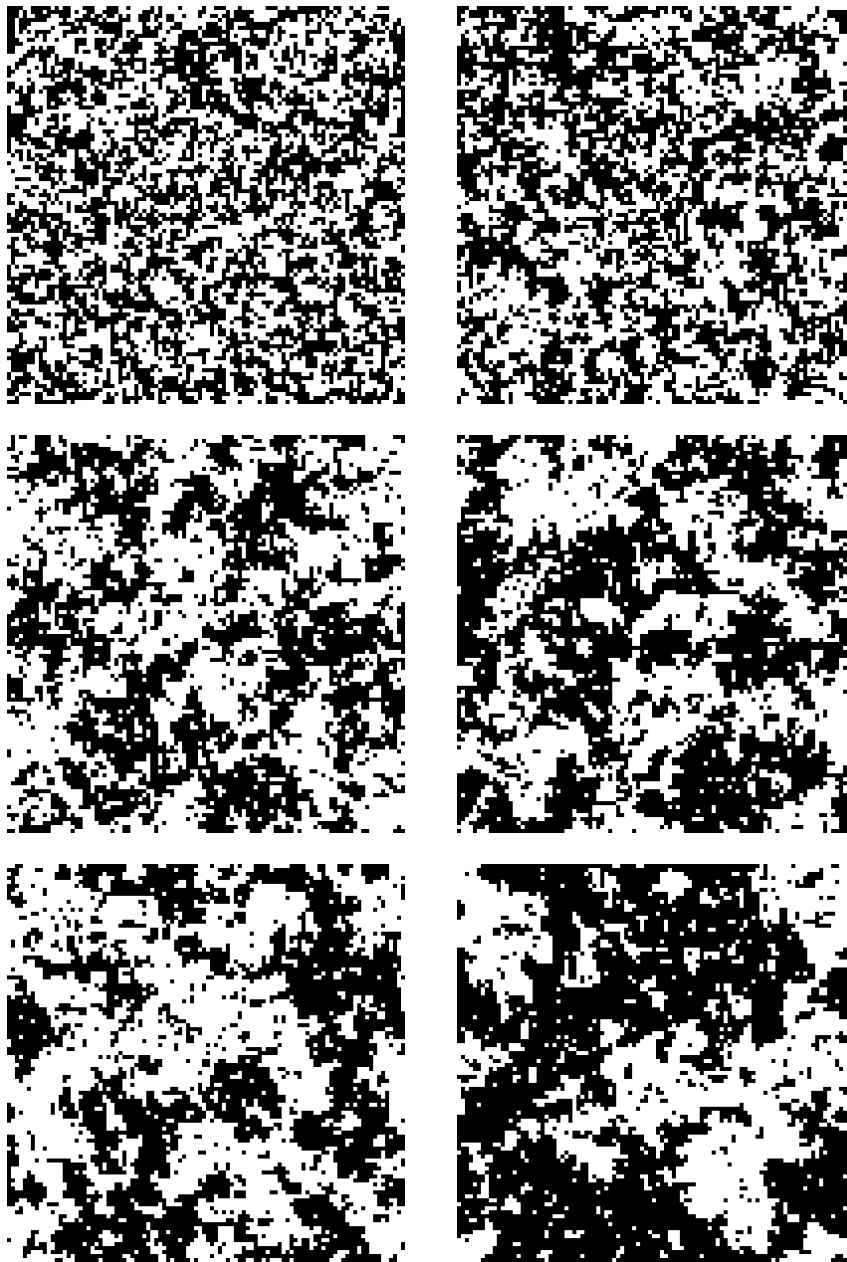


**Figure 20.** Illustration of the growth of spatial correlations when criticality is approached on a lattice  $100 \times 100 : \beta = 0.22, 0.31, 0.37, 0.39, 0.42, 0.43$ .

Since our system is finite and lives on a lattice, the rotational symmetry  $\text{SO}(2)$  of  $\mathbb{R}^2$  is broken down to the discrete subgroup  $\mathbb{Z}_4$  of  $\frac{\pi}{2}$  rotations. We take advantage of this and the translational symmetry of the system to compute an improved version of the correlation function  $G(\vec{r})$  by defining the observables:

$$S_x \equiv \frac{1}{L} \sum_{y=1}^L \sigma(x, y) \quad (23)$$

$$S_y \equiv \frac{1}{L} \sum_{x=1}^L \sigma(x, y) \quad (24)$$

where  $x$  and  $y$  are the two orthogonal directions in the lattice.

We can compute the correlation function as:

$$G(r) = \frac{1}{2} \left( \frac{1}{L} \sum_{x=1}^L S_x S_{x+r} + \frac{1}{L} \sum_{y=1}^L S_y S_{y+r} \right) \quad (25)$$

Because of the periodic boundary conditions on the lattice we also have that:

$$\sigma(x+aL, y+bL) = \sigma(x, y) \quad \forall (a, b) \in \mathbb{Z}^2 \quad (26)$$

and therefore, the exponential form of  $G$  is modified to that of a hyperbolic cosine:

$$G(r) \sim \frac{1}{2} \left( e^{\frac{r}{\xi}} + e^{-\frac{r}{\xi}} \right) \sim \cosh \left( \frac{r - \frac{L}{2}}{\xi} \right) \quad (27)$$

In (Fig.21) we can see the exponential decay of the correlation function at large distances.

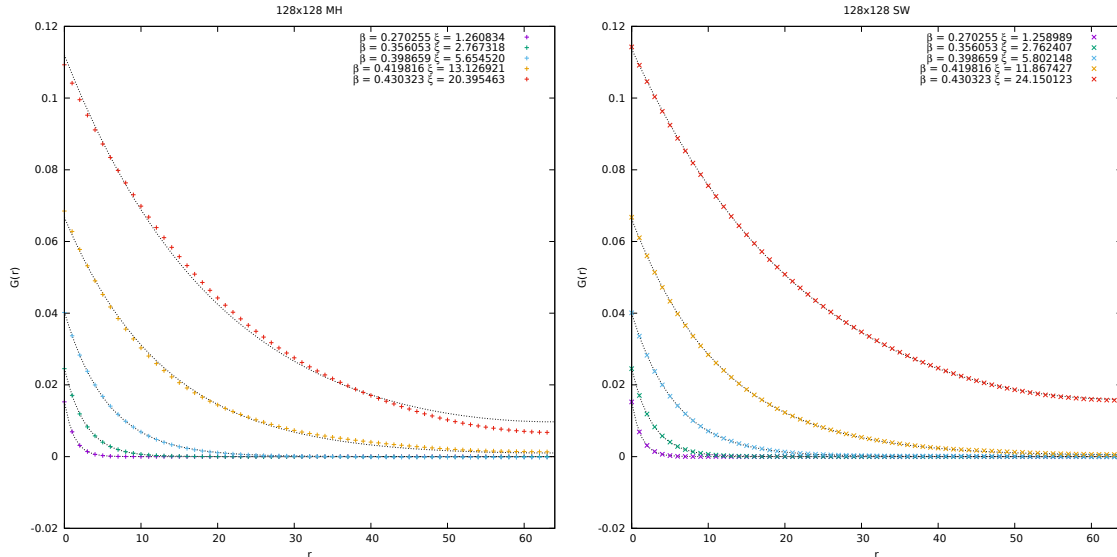


**Figure 21.** Correlation functions for various values of  $\beta$ . The lattice size used is  $128 \times 128$  in order to reduce finite-size effects. As a precaution, we consider an interval in  $\beta$ -space such that the correlation length is much smaller than the size of the lattice (approximately one order of magnitude smaller).

The correlation length diverges at the critical point as:

$$\xi \sim A |x|^{-\nu} \quad (28)$$

where  $\nu$  is an example of critical exponent of the model. We plot the data obtained from the previous fit using logarithmic scales on both axis. This way we can easily obtain the critical exponent  $\nu$  from a linear fit:

$$\log(\xi) = \log(A) - \nu \log(|x|) \quad (29)$$

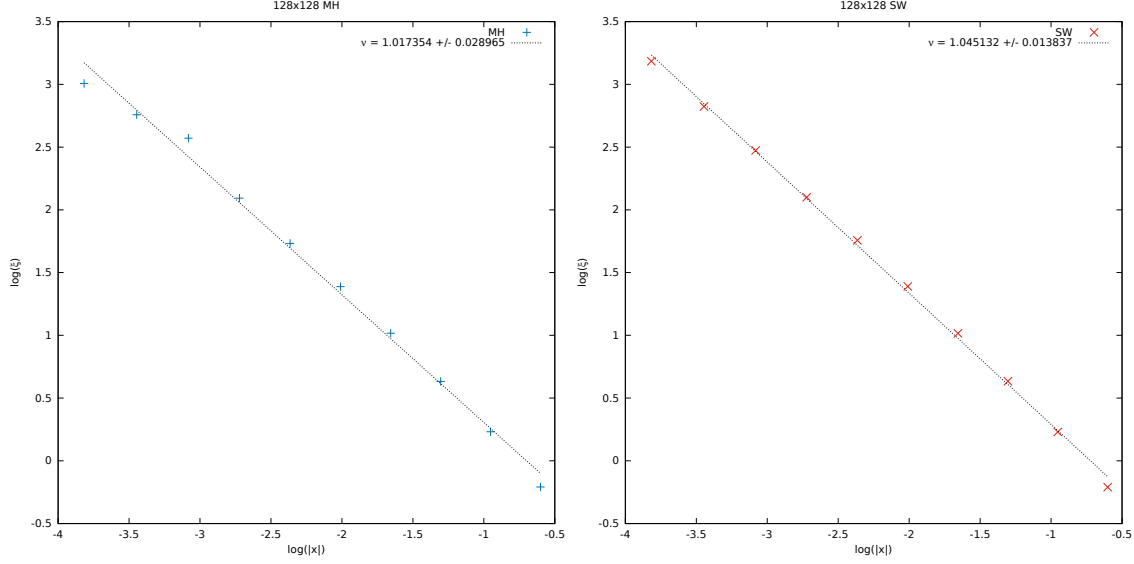


**Figure 22.** Plot of the correlation length dependence on the parameter  $x = \frac{\beta - \beta_c}{\beta_c}$  for a lattice of size  $128 \times 128$ . MH on the left and SW on the right. The errors are computed by jackknife binning of the fit data from (Fig.21) through (27).

The results are:

$$\nu_{\text{MH}} = 1.017 \pm 0.029 \quad (30)$$

$$\nu_{\text{SW}} = 1.045 \pm 0.014 \quad (31)$$

Both results are compatible with the known exact value  $\nu = 1$ .

## 1.8 Finite Size Scaling

The main results of the finite size scaling (FSS) study are usually estimates of the critical temperature and the critical exponents characterizing the universality class of the transition. In the infinite-volume limit most of the expectation values one can compute from  $e$  and  $m$  exhibit singularities at the transition point. In finite systems, though, the singularities are smeared out and the standard observables scale according to:

$$m = L^{-\beta/\nu} f_m(y) + \dots \quad (32)$$

$$C = C_{\text{reg}} + L^{\alpha/\nu} f_C(y) + \dots \quad (33)$$

$$\chi = L^{\gamma/\nu} f_\chi(y) + \dots \quad (34)$$

where  $\alpha, \beta, \gamma$  and  $\nu$  are the critical exponents,  $f_i(x)$  are FSS functions and  $y$  is the scaling variable. Near the phase transition the correlation length  $\xi \sim x^{-\nu}$  is the only length scale with which to describe the physics of the system, therefore the only adimensional quantity we can construct from it is:

$$y = L/\xi \sim L x^\nu = (L^{1/\nu} x)^\nu = L x \quad (35)$$

We now can remove any dependence on the scale of the system by rescaling the observables by the appropriate power of  $L$  given by the relative critical exponent. This way we expect each observable, expressed as functions of the scaling variable  $y$ , to collapse on the same curve  $f_i(y)$  regardless of the value of  $L$  (at least in the vicinity of  $\beta_c$ ).

$\nu$	1
$\alpha$	0
$\beta$	1/8
$\gamma$	7/4

**Table 3.** Exact critical exponents for the Ising model in 2d.

With a procedure completely analogous to that of (Sect.1.5), one could also obtain estimates for the critical exponents  $\alpha, \beta, \gamma$  and  $\nu$  by extrapolating the infinite size limit.

*Remark:* we observe that since the exact value of exponent  $\alpha$  of the model is zero, the quantity  $C$  should, in principle, not scale with the lattice size. In reality  $C$  has a logarithmic divergence at the critical point, hence we adopt the scaling law:

$$C \sim \log(L^{1/\nu}) \quad (36)$$

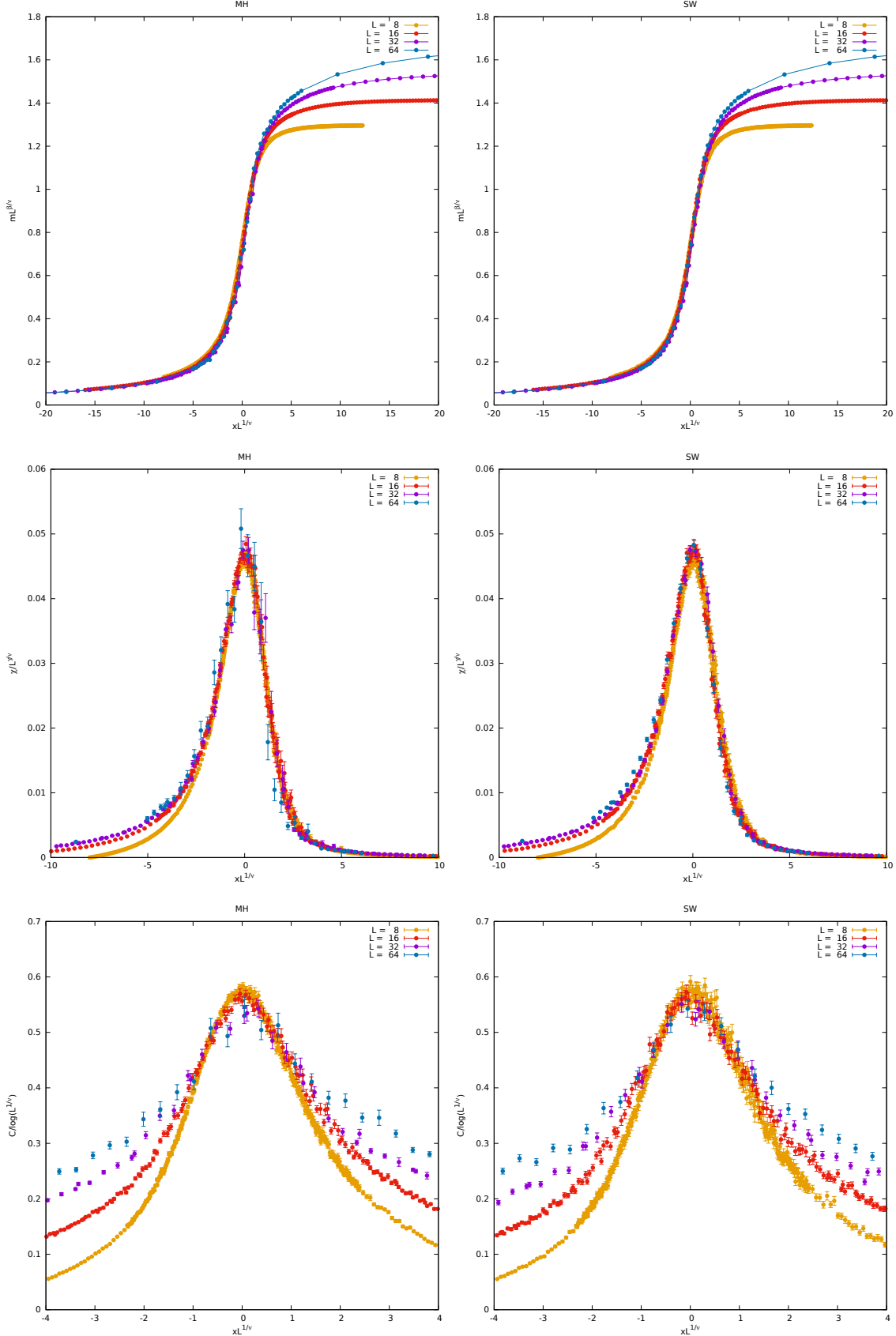


**Figure 23.** Finite Size Scaling study for the lattice sizes  $8^2, 16^2, 32^2, 64^2$ . Left MH, right SW. The top plot represents the scaling of the magnetization, the center one the magnetic susceptibility and the bottom one the heat capacity.

# Laboratory of Computational Physics

BY LUCA CASSIA

Dipartimento di Fisica, Università di Milano-Bicocca  
I-20126 Milano, Italy

Email: 1.cassia@campus.unimib.it

## Table of contents

<b>1 Potts Model 2d</b> . . . . .	1
1.1 Thermalization . . . . .	1
1.2 Autocorrelation Times . . . . .	2
1.3 Observables . . . . .	3
1.4 $\beta$ Critical . . . . .	4
1.5 Probability Distribution Functions . . . . .	7
1.6 Spatial Correlations . . . . .	9
1.7 Finite Size Scaling . . . . .	11

## 1 Potts Model 2d

The 2-dimensional Potts Model constitutes a generalization of the Ising Model to a generic number  $q \in \mathbb{N}$  of states for the spin variable. A useful way to picture the space of states of a Potts spin variable is to map it to the space  $U(1) \subset \mathbb{C}$  of unimodular complex numbers. We represent each state  $p$  with the  $p^{\text{th}}$  complex  $q$ -root of the unity in  $\mathbb{C}$ :

$$p \mapsto e^{\frac{2\pi i}{q} p} \in U(1) \quad (1)$$

Lets consider a 3-state Potts system of  $L \times L$  spins situated on the points of a regular square lattice with periodic boundary conditions (PBC) in both directions, as for the Ising Model. Each spin interacts with its nearest neighbours inside the lattice, with an Hamiltonian:

$$\mathcal{H} = - \sum_{\langle i,j \rangle} \delta_{\sigma_i, \sigma_j} \quad (2)$$

where the sum is taken only over the set of unordered pairs  $\langle i, j \rangle$  such that  $\sigma_i$  and  $\sigma_j$  are nearest neighbours. The implementation of the MH algorithm is completely analogous to that for the ising model, while for the SW algorithm we need to modify the probability with which to activate the link between neighbouring spins. In fact, the partition function can be written as:

$$Z[\beta] = \sum_{\{\sigma\}} e^{\beta \sum_{\langle ij \rangle} \delta_{\sigma_i, \sigma_j}} = \sum_{\{\sigma\}} \prod_{\langle ij \rangle} e^{\beta \delta_{\sigma_i, \sigma_j}} \quad (3)$$

using the Fortuin-Kasteleyn representation we can write:

$$e^{\beta \delta_{\sigma_i, \sigma_j}} = 1 + (e^\beta - 1) \delta_{\sigma_i, \sigma_j} = e^\beta [e^{-\beta} + (1 - e^{-\beta}) \delta_{\sigma_i, \sigma_j}] \quad (4)$$

therefore we can immediately read the probability of establishing a link between neighbouring spins as:

$$p = 1 - e^{-\beta} \quad (5)$$

### 1.1 Thermalization

As for the case of the Ising Model, we opted for a cold start approach. In (Fig.1) we present the thermalization process for MH and SW at various temperatures and for two different volumes:  $32^2$  and  $64^2$ . The observed quantity is the energy density:

$$e = \langle \mathcal{H} \rangle / V \quad (6)$$

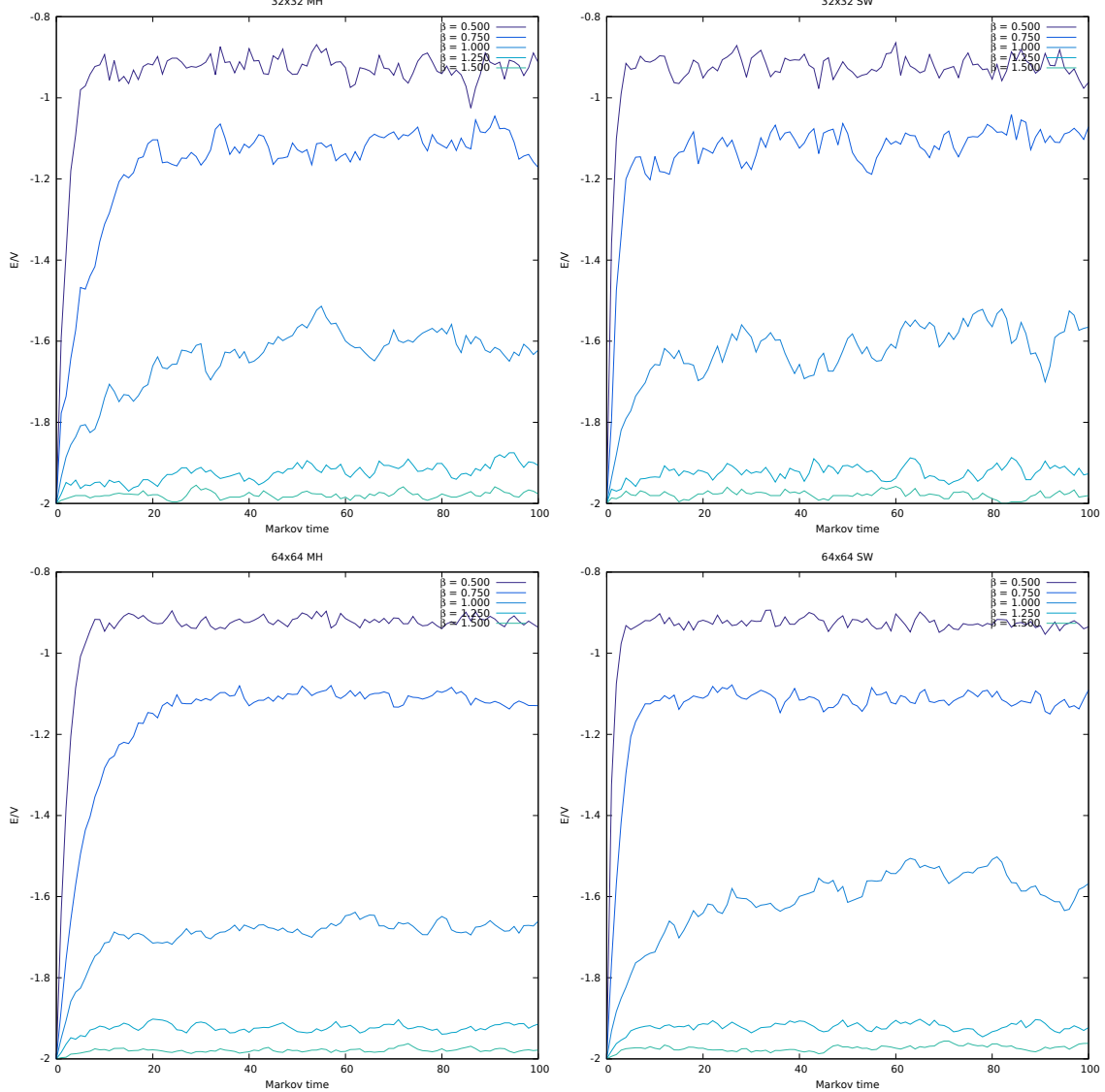


**Figure 1.** Thermalization process of the energy density on a lattice  $32 \times 32$  in the top two pictures and  $64 \times 64$  in the bottom two. MH on the left, SW on the right.

As expected, the MH algorithm has a slower mixing rate due to the critical slowing down effect near the critical inverse temperature:

$$\beta_c = \log(1 + \sqrt{3}) \approx 1.00505254\dots \quad (7)$$

For this reason we focus only on the study of the model through the implementation of the much more efficient SW algorithm. The thermalization time is taken to be 1000 Markov steps.

## 1.2 Autocorrelation Times

We now study the correlations present in the energy density signal produced by the Markov process. As we did for the Ising Model, we fit the data using the integrated autocorrelation time exact result for a bivariate gaussian signal:

$$\tau_{\text{int}}(k_{\max}) = \tau_{\text{int}} \left[ 1 - \frac{2 \tau_{\text{exp}}}{2 \tau_{\text{exp}} + 1} e^{-k_{\max}/\tau_{\text{exp}}} \right] \quad (8)$$

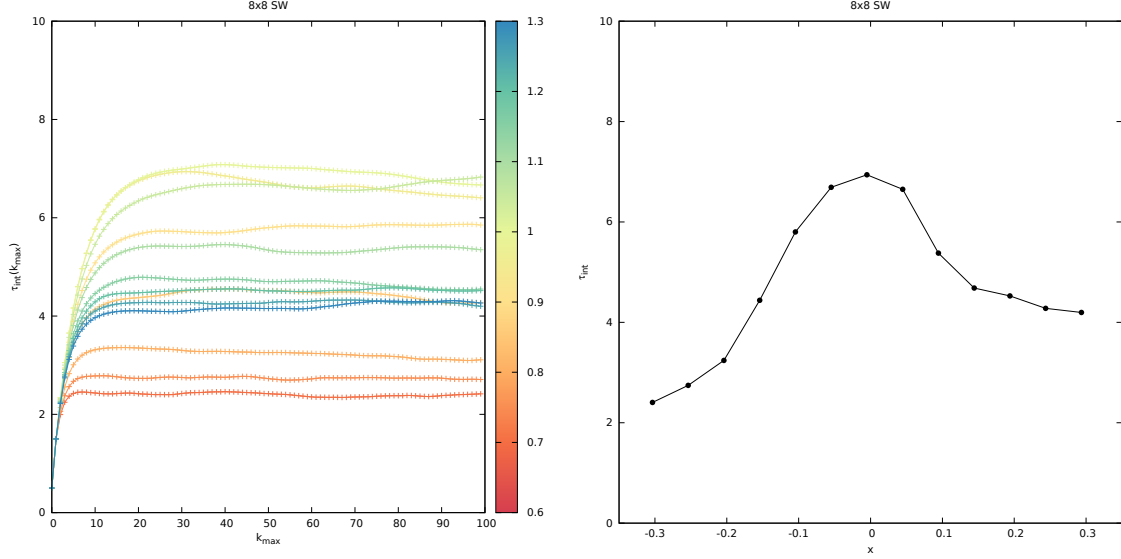


**Figure 2.** Plots of the autocorrelation of the signal for  $e$ . On the left is shown the integrated autocorrelation time  $\tau_{\text{int}}$  as a function  $k_{\text{max}}$ . The chromatic scale indicates the value of  $\beta$ . On the right is shown the plot of  $\tau_{\text{int}}$  as a function of  $x = \frac{\beta - \beta_c}{\beta_c}$ . The lattice size is  $L = 8$ .

As already pointed out, the autocorrelation time of the SW signal is very low even near the phase transition because of the dynamical critical exponent  $z \approx 0$ . Thus we can safely set the bin size to 50.

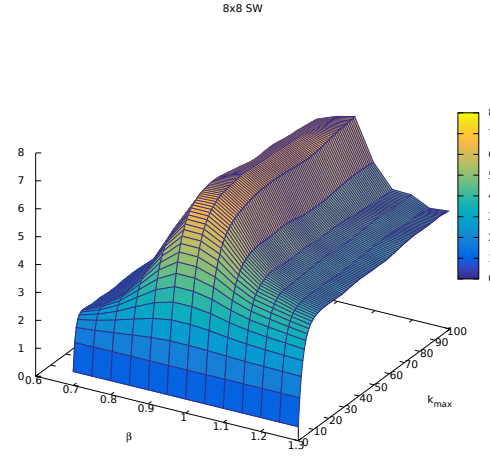


**Figure 3.** 3d plot of  $\tau_{\text{int}}(\beta, k_{\text{max}})$  for a Potts Model of volume  $8 \times 8$  near  $\beta_c$ .

### 1.3 Observables

The main observables of interest for this system are the energy density  $e$  and the magnetization  $m$ :

$$e = \langle \mathcal{H} \rangle / V, \quad (9)$$

$$m = \langle |\mathcal{M}| \rangle, \quad \mathcal{M} = \frac{1}{V} \sum_i \sigma_i \quad (10)$$

For each inverse temperature we compute the estimate of the generic observable  $\mathcal{O}$  from a set of  $5 \cdot 10^4$  measurements.

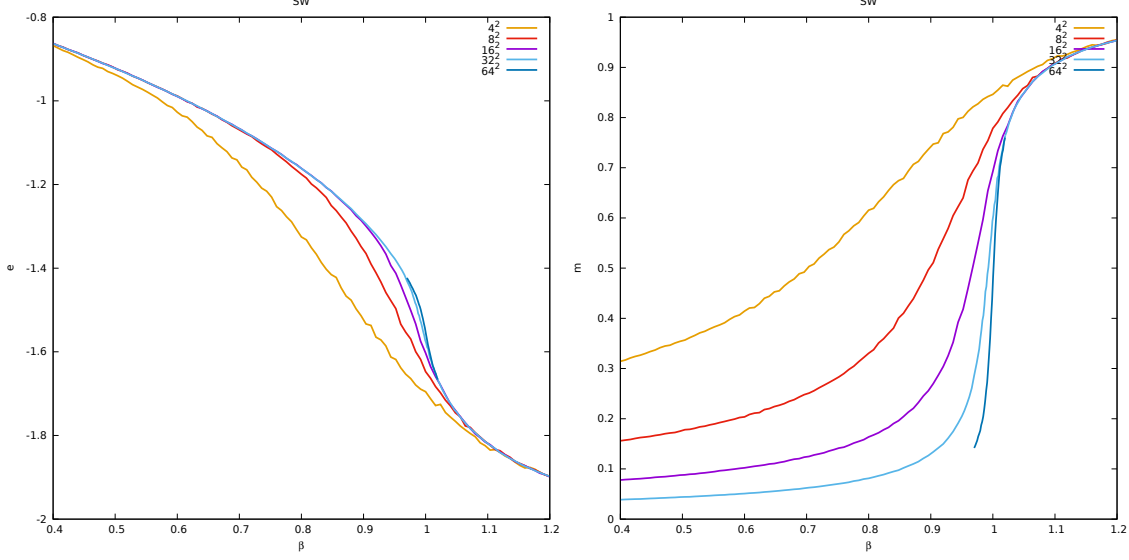


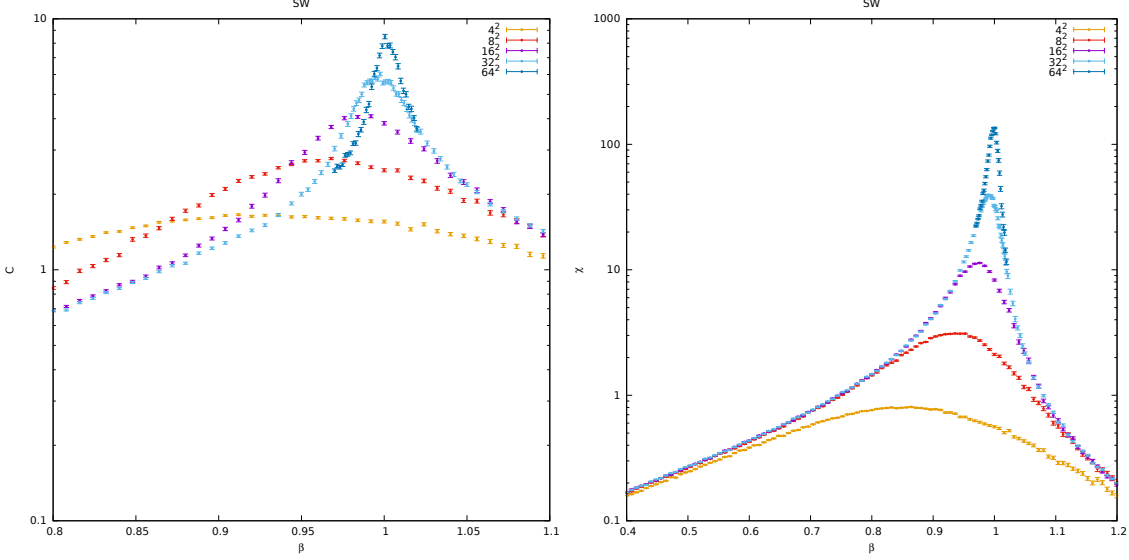
**Figure 4.** Left: energy density  $e$  as a function of  $\beta$ . Right: magnetization modulus  $m$ . The various colors represent different lattice sizes:  $L = 4, 8, 16, 32$ .

As the lattice volume  $V = L^2$  increases, both the energy and magnetization curves approach their infinite volume limit.

We also plot the heat capacity and the magnetic susceptibility:

$$C = \frac{\beta^2}{V} \langle (\mathcal{H} - \langle \mathcal{H} \rangle)^2 \rangle \quad (11)$$

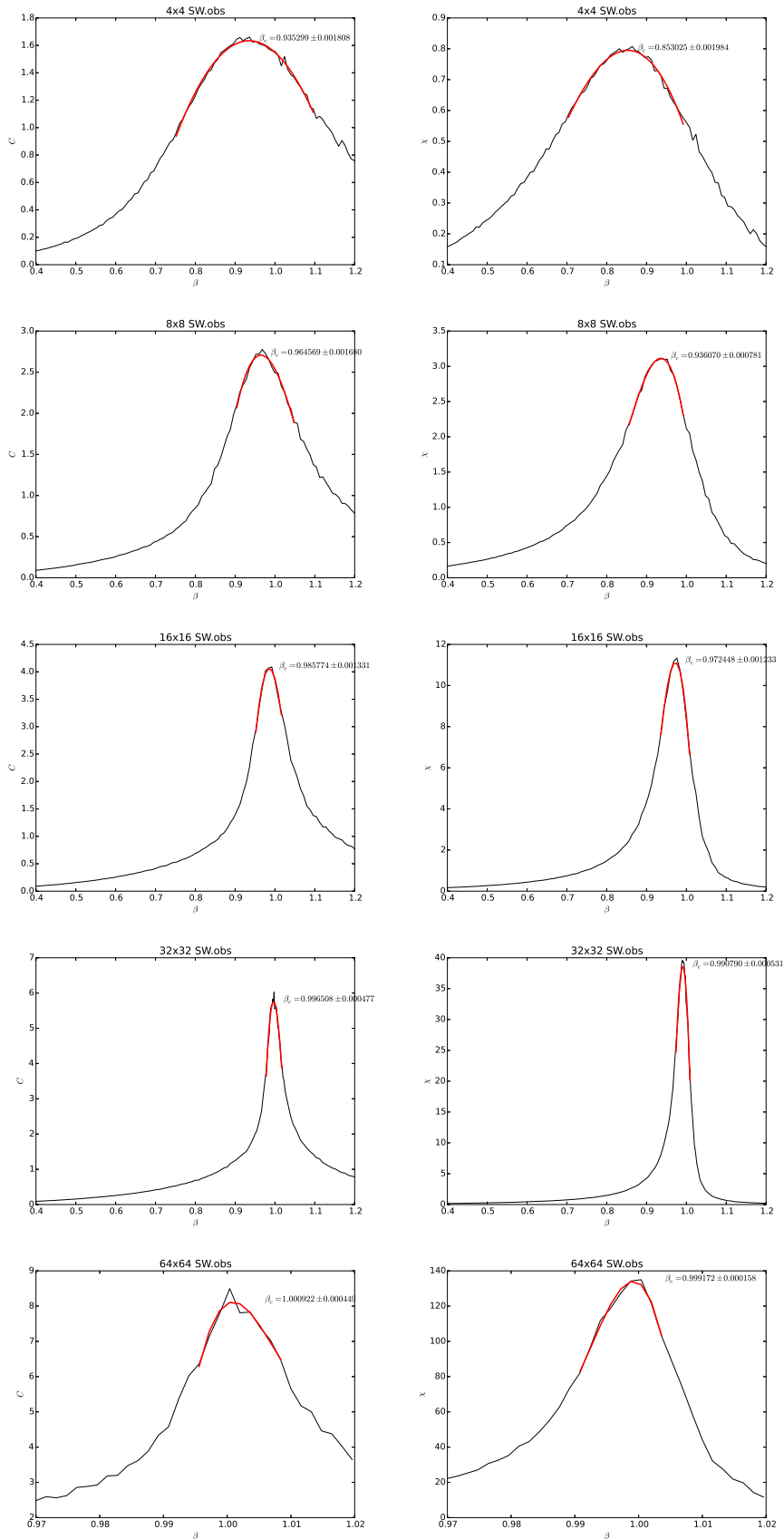
$$\chi = \beta V \langle (|\mathcal{M}| - \langle |\mathcal{M}| \rangle)^2 \rangle \quad (12)$$



**Figure 5.** Left: heat capacity as a function of  $\beta$ . Right: magnetic susceptibility. The various colors represent different lattice sizes:  $L = 4, 8, 16, 32, 64$ .

#### 1.4 $\beta$ Critical

From a power law fit of the points near the peak of each dataset we obtain estimates for the pseudocritical  $\beta$ -values at finite sizes  $L = 4, 8, 16, 32, 64$ .

**Figure 6.** Fit of the heat capacity and susceptibility peaks.

$L$	$\beta_{\max}(C)$	$\beta_{\max}(\chi)$
4	$0.93530 \pm 0.00181$	$0.85303 \pm 0.00198$
8	$0.96457 \pm 0.00168$	$0.93607 \pm 0.00078$
16	$0.98577 \pm 0.00133$	$0.97245 \pm 0.00123$
32	$0.99651 \pm 0.00048$	$0.99079 \pm 0.00053$
64	$1.00092 \pm 0.00045$	$0.99917 \pm 0.00016$

**Table 1.** Pseudocritical  $\beta$ -values obtained by polynomial fit of the peaks of  $C$  and  $\chi$ .

The polynomial function we used for the fit is:

$$f(\beta) = A + B(\beta - \beta_{\max})^2 + C(\beta - \beta_{\max})^3 \quad (13)$$

We can now obtain an estimate of  $\beta_c$  from a power law fit to the location of the maxima  $\beta_{\max}$ :

$$\beta_{\max} = \beta_c - c L^{-\nu} \quad (14)$$

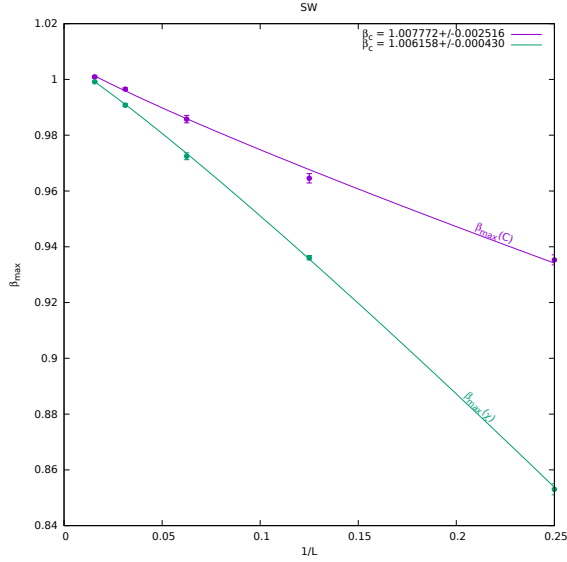


**Figure 7.** Pseudocritical inverse temperature fit. The purple lines are relative to the heat capacity  $C$  while the green ones to the magnetic susceptibility  $\chi$ .

The result of the fit are:

$$\beta_c(C) = 1.00777 \pm 0.00252 \quad (15)$$

$$\beta_c(\chi) = 1.00616 \pm 0.00043 \quad (16)$$

As we can see, both values obtained from the fit of  $C$  and  $\chi$  are very close to the exact solution of (7). We could improve these results further by discarding some measurements done at smaller volumes ( $L = 4$  and  $L = 8$  for instance) and repeat the measurement procedure for larger lattice sizes.

## 1.5 Probability Distribution Functions

We study the probability distribution of the magnetization for a lattice of size  $L = 8$ . The energy and magnetization levels of a discrete system are quantized. In particular, for a Potts Model on a square lattice of size  $L^2$  with PBC, there are exactly  $\frac{1}{2}(L^2 + 1)(L^2 + 2)$  magnetization levels distributed as in (Fig.8):

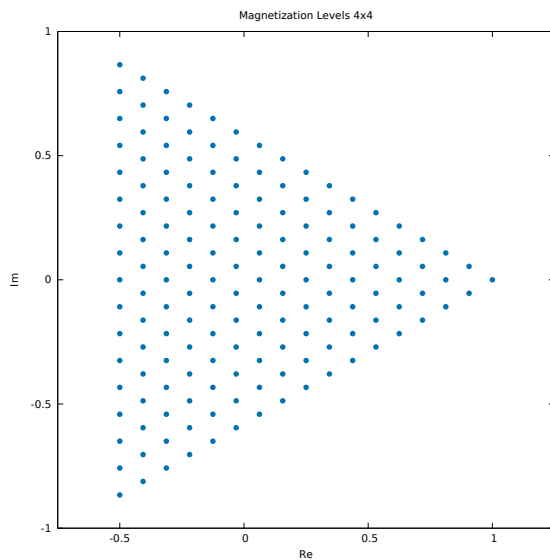


**Figure 8.** Magnetization levels of the Potts Model on a  $4 \times 4$  lattice. We remark that, since the average is a convex function of its arguments, every magnetization level must be contained in the convex hull of the three basic magnetizations  $1, \frac{-1+i\sqrt{3}}{2}, \frac{-1-i\sqrt{3}}{2}$  (*magnetization domain*).

With this consideration one can construct the probability distribution function of the magnetization just by counting the number of samples in each level (for  $L$  not too large):

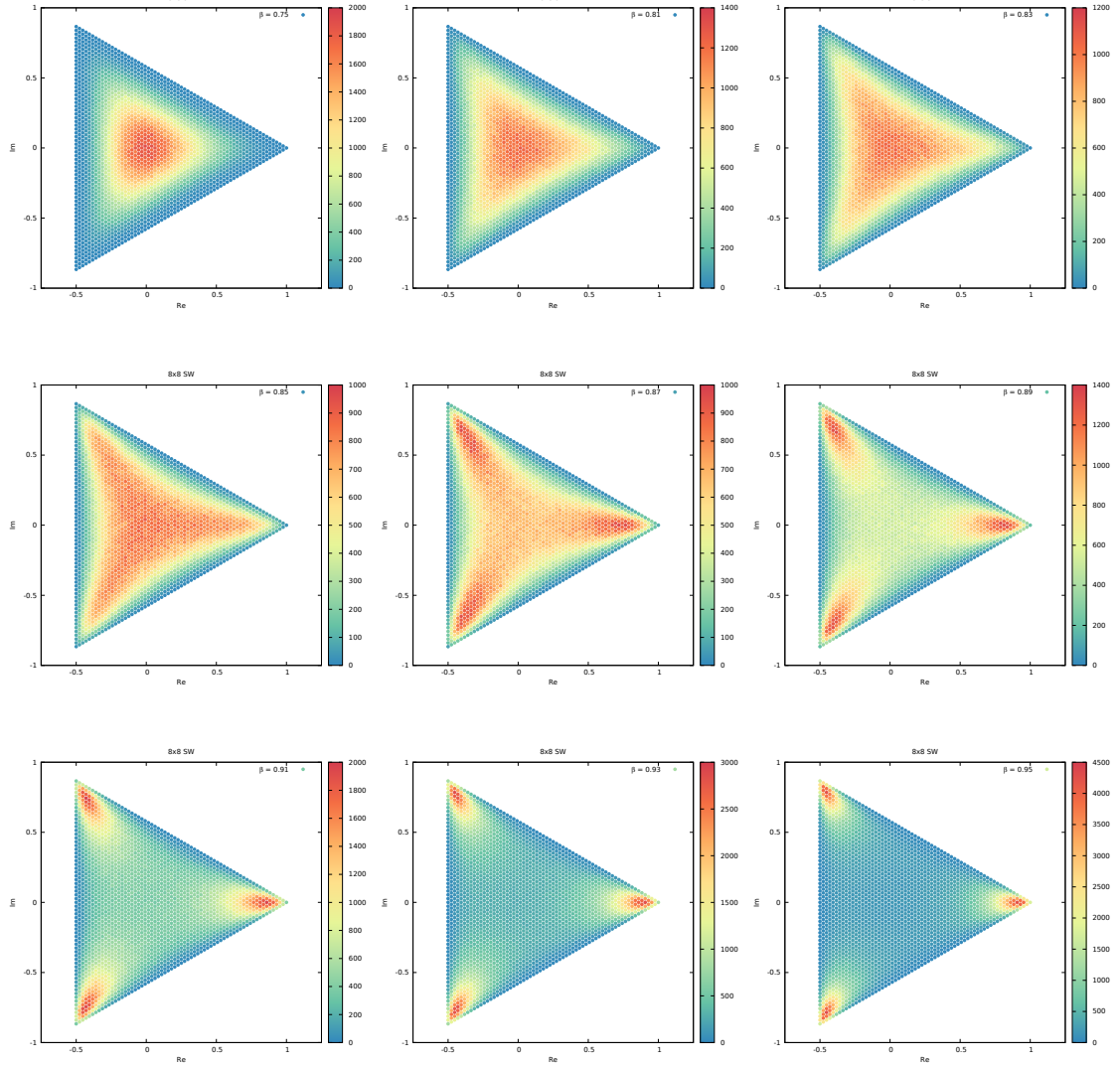


**Figure 9.** Probability distribution functions of  $\mathcal{M} \in \mathbb{C}$  obtained from  $10^6$  sweeps of SW on a lattice  $8 \times 8$ .

At low values of  $\beta$  (high temperature  $T$ ) the system is found most probably in the disordered state  $\mathcal{M} \approx 0$  and every spin state has equal probability. As the temperature lowers and approaches the critical point  $T_c$ , the probability distribution widens and takes the shape of a triangle oriented

as the magnetization domain. Finally, as we cross the critical point, the distribution becomes peaked around three different points situated along the directions of the cubic roots of the unity and representing high probabilities for configurations where a large number of spins are aligned. In the limit  $\beta \rightarrow \infty$  ( $T \rightarrow 0$ ) these points tend to the vertices of the triangle and the peaks of the probability distribution become very narrow.

## 1.6 Spatial Correlations

The two-point correlation function is defined as:

$$G(\vec{r}_i - \vec{r}_j) = \langle \text{Re}(\sigma_i \sigma_j^*) \rangle \sim \exp(-|\vec{r}_i - \vec{r}_j|/\xi) \quad \text{for large } |\vec{r}_i - \vec{r}_j| \quad (17)$$

where  $\xi$  is the correlation length of the system:

$$\xi = -\lim_{|\vec{r}| \rightarrow \infty} (|\vec{r}| / \ln G(\vec{r})) \quad (18)$$

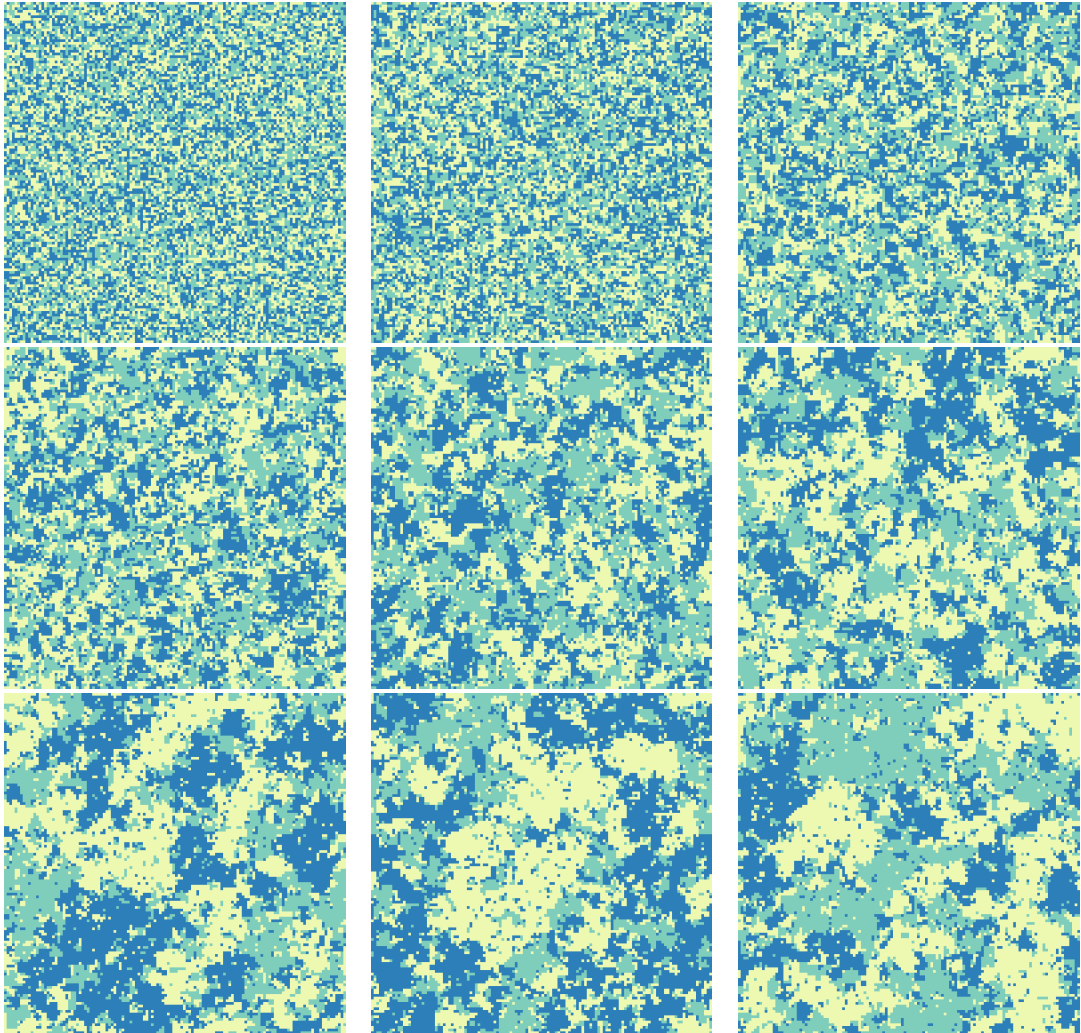


**Figure 10.** Illustration of the growth of spatial correlations when criticality is approached on a lattice  $128 \times 128 : \beta = 0.2, 0.5, 0.7, 0.8, 0.9, 0.95, 0.97, 0.98, 0.99$ .

Analogously to the case of the Ising Model we define observables:

$$S_x \equiv \frac{1}{L} \sum_{y=1}^L \sigma(x, y) \quad (19)$$

$$S_y \equiv \frac{1}{L} \sum_{x=1}^L \sigma(x, y) \quad (20)$$

and we compute the correlation function as:

$$G(r) = \frac{1}{2} \left( \frac{1}{L} \sum_{x=1}^L \frac{S_x S_{x+r}^*}{S_x S_x^*} + \frac{1}{L} \sum_{y=1}^L \frac{S_y S_{y+r}^*}{S_y S_y^*} \right) \quad (21)$$

Again the fit is done via the hyperbolic cosine function:

$$G(r) \sim \frac{1}{2} \left( e^{\frac{r}{\xi}} + e^{-\frac{r}{\xi}} \right) \sim \cosh \left( \frac{r - \frac{L}{2}}{\xi} \right) \quad (22)$$

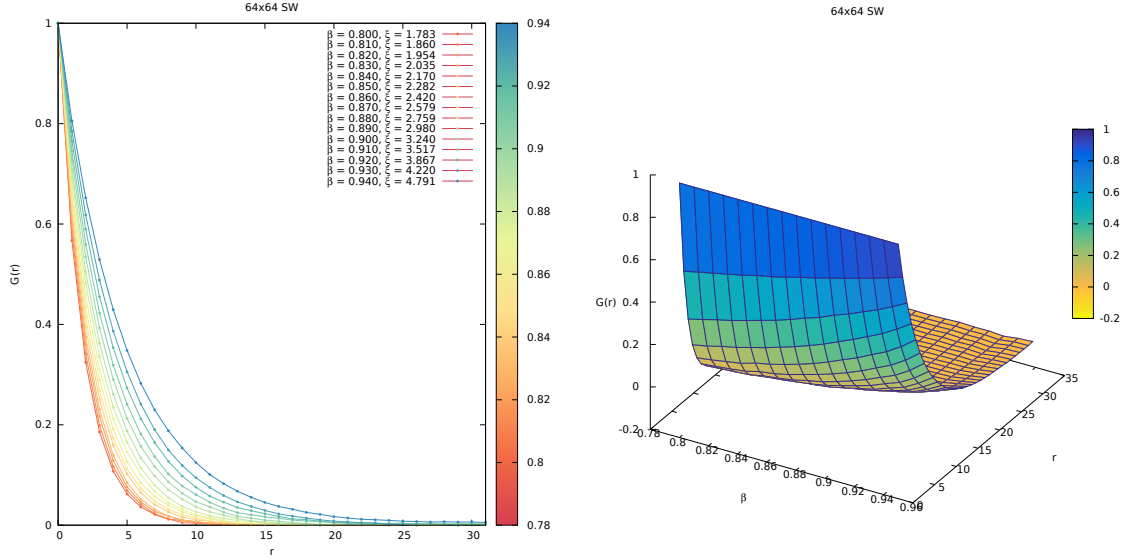


**Figure 11.** Correlation functions for various values of  $\beta$ . The lattice size used is  $64 \times 64$ . As a precaution, we consider an interval in  $\beta$ -space such that the correlation length is much smaller than the size of the lattice (approximately one order of magnitude smaller).

The correlation length diverges at the critical point as:

$$\xi \sim A |x|^{-\nu} \quad (23)$$

We plot the data obtained from the previous fit using logarithmic scales on both axis and compute the critical exponent  $\nu$  from the linear fit:

$$\log(\xi) = \log(A) - \nu \log(|x|) \quad (24)$$

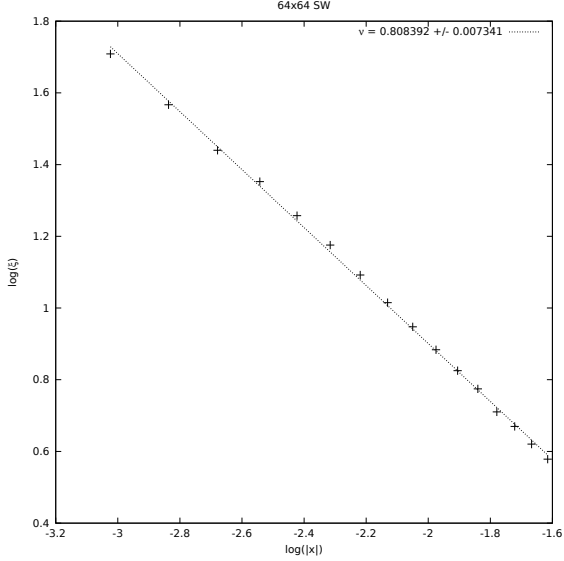


**Figure 12.** Plot of the correlation length dependence on the parameter  $x = \frac{\beta - \beta_c}{\beta_c}$  for a lattice of size  $64 \times 64$ . The errors are computed by jackknife binning of the fit data from (Fig. 11).

The result of the fit is:

$$\nu_{SW} = 0.80839 \pm 0.00734 \quad (25)$$

which is comparable with the exact value:

$$\nu = \frac{5}{6} \approx 0.83333\dots$$

## 1.7 Finite Size Scaling

The critical exponents of the model are:

$\nu$	$5/6$
$\alpha$	$1/3$
$\beta$	$1/9$
$\gamma$	$13/9$

**Table 2.** Exact critical exponents for the Potts model in 2d.

We therefore rescale the observables as:

$$m \rightarrow m L^{\beta/\nu} \quad (26)$$

$$\chi \rightarrow \chi / L^{\gamma/\nu} \quad (27)$$

$$C \rightarrow C / L^{\alpha/\nu} \quad (28)$$

and plot the data expressed as function of the scaling variable  $x L^{1/\nu}$ :

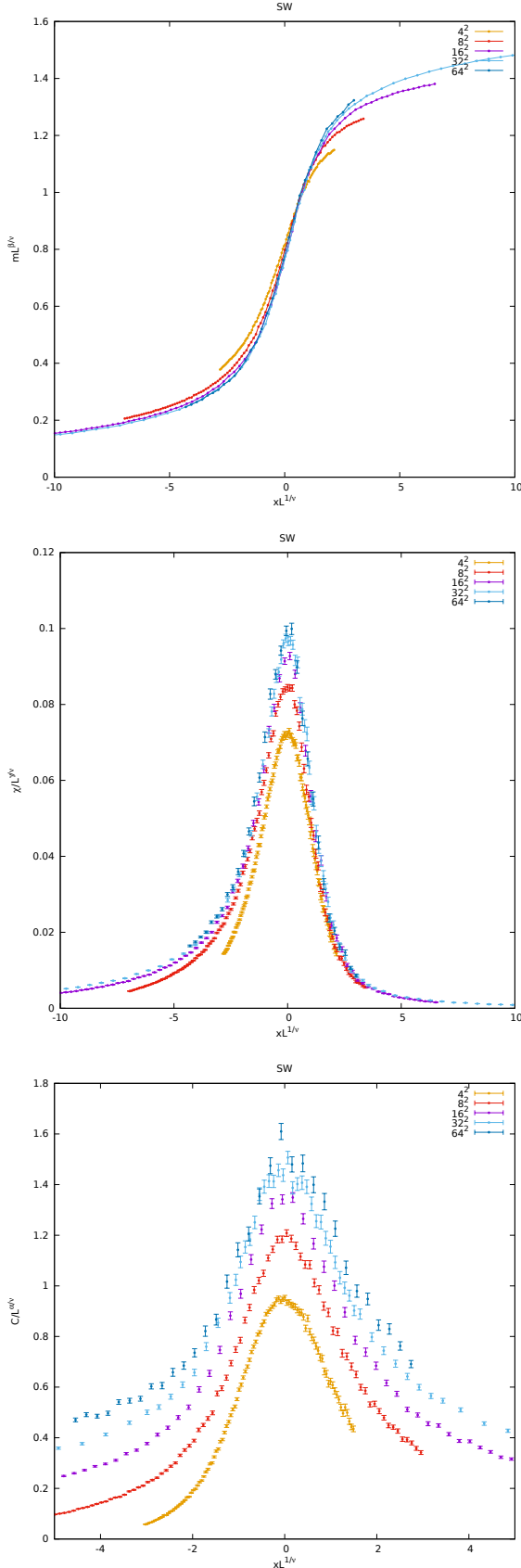


**Figure 13.** Finite Size Scaling study for the lattice sizes  $4^2, 8^2, 16^2, 32^2$ . The top plot represents the scaling of the magnetization, center one the magnetic susceptibility and the bottom one the heat capacity.

*Remark:* the curves obtained by rescaling of the magnetization, susceptibility and heat capacity, fit well to the FSS functions  $f_i(x L^{1/\nu})$  when the system has a large enough volume that the boundary effects are negligible. However, for smaller volumes ( $L = 4, 8$ ) those effects are more important and, as we can see from (Fig.13), the fit becomes worse. In particular we see that the value  $L=4$  is too small for the scaling hypothesis to apply.